Surface and interface properties of BaTiO3 ferroelectric thin films studied by in-situ photoemission spectroscopy

Emmanuel Arveux

N° d'ordre : 3921

THÈSE

PRÉSENTÉE A

L'UNIVERSITÉ BORDEAUX 1

ÉCOLE DOCTORALE DES SCIENCES CHIMIQUES

Par Emmanuel Arveux

POUR OBTENIR LE GRADE DE

DOCTEUR

SPÉCIALITÉ : Science des matériaux

Propriétés de surfaces et interfaces de couches minces ferroélectriques de $BaTiO_3$ étudiées par spectroscopie de photoémission in-situ.

Soutenue le 8 Décembre 2009

Devant la commission d'examen formée de :

M. Claude Delmas	Directeur de recherche – ICMCB (CNRS)	*Examinateur*
M. Wolfgang Donner	Professeur – TUD	*Examinateur*
M. Jean Etourneau	Professeur – ICMCB (CNRS)	*Membre invité*
M. Wolfram Jaegermann	Professeur – TUD	*Examinateur*
M. Andreas Klein	Außerplanmässiger Professeur – TUD	Co-*Directeur de thèse*
M. Mario Maglione	Directeur de recherche – ICMCB (CNRS)	Co-*Directeur de thèse*
M. Christophe Muller	Professeur – IM2NP Marseille	*Rapporteur*
Mme Sandrine Payan	Maître de conférence – ICMCB (CNRS)	*Co-directrice de thèse*
M. Dieter Schmeiβer	Professeur – TU Cottbus	*Rapporteur*

Surface and interface properties of $BaTiO_3$ ferroelectric thin films studied by in-situ photoemission spectroscopy

emmanuelarveux@gmail.com

Introduction

Before 1970, the most exciting challenge in ferroelectrics was modelling ferroelectric phase transitions and discovering new ones [1]. The focus changed after 1988 [2], when thin films were developed and first integrated into semiconductor chips at the nanoscale through ferroelectric random access memory devices, thin film capacitors and tunable microwave devices. For instance, in memory applications, where several kilovolts are required to switch the polarization of a large single crystal from up (+1) to down (-1) state, it requires only a few volts in thin film of ~100nm thickness, making them suitable for memories with low voltage supply.

Unfortunately, the functional properties of ferroelectric thin films are strongly degraded as the film thickness is decreased like enormous reductions in dielectric constant, significant broadening of the Curie anomaly (peak in dielectric constant with respect to the temperature), and increase of the leakage current. The origins of such "size effects" have thus been intensively studied in this context but remains, however, considerably debated [3].

One of the most important effects contributing to such size dependence has been well ascribed to the presence of interfaces [4]. They can be extrinsic to the material (e.g. film/electrode interfaces) or intrinsic to the materials (e.g. grain boundaries, surfaces). The knowledge of the chemical and electronic nature of such interfaces becomes therefore very challenging regarding their influences in functional properties of thin films. This thesis work begins at this stage.

Typical experimental approaches to study ferroelectric thin film properties are usually based on electrical characterizations, e.g. current ─voltage characteristics or impedance spectroscopy. However, such macroscopic methods are rather limited to identify the interface properties mentioned above due to the interdependence of parameters. In addition, the microscopic properties cannot be directly accessed from such experimental approach. One of our objectives is to make use of in-situ photoemission spectroscopy (XPS) to investigate the chemical and electronic properties of ferroelectrics thin films at their surfaces and interfaces with the substrate and the top electrode. XPS has been widely used for many years to study semiconductor interface formation and is applied in the present work on perovskite-structure titanate materials ($ATiO_3$). Such XPS investigations of ferroelectric films were only rarely performed and no systematic study of the influence of dopants is available to date.

Recently, photoemission spectroscopy has proven to be an important analytical technique to study the near surface/interface chemistry of $ATiO_3$ compositions in the bulk form [5] or in thin film form [6] but the literature presents a contradictory and unclear picture as deduced from core-level photoemission spectra. This is mainly due to the different surface preparations, which have been used prior to the measurement to obtain a clean surface. For instance, it has been shown that cleaning $ATiO_3$ surfaces by ion sputtering produces a non-stoichiometric surface region introducing new features in photoemission spectra making the data interpretation ambiguous. In this context, the surface preparation is a crucial step to be able to observe the intrinsic surface properties.

Our photoemission studies were thus carried out in-situ between thin film preparations and surface analysis step at the Darmstadt Integrated System for Material research (DAISY-MAT) thereby avoiding surface contaminations during the experiments without the use of etching step. The work follows a previous thesis on the properties of $(Ba,Sr)TiO_3$ (BST) thin films and interfaces by R. Schafranek [7]. While his work was performed on non-ferroelectric materials, the present work extents the systematic to the ferroelectric $BaTiO_3$ composition. In addition, another thesis performed at the ICMCB by V. Reymond [8] on BST films and BST/dielectric multilayers have shown that interfaces have key contribution to the dielectric losses. Our problematic is thus to understand the defect states and electronic structure at interfaces using photoemission spectroscopy with in-situ sputtering deposition.

The first chapter of this thesis is composed of three sub-sections. The first one introduces briefly the ferroelectric properties in bulk materials with a particular emphasis on the different mechanism of polarization. Then, the second part describes the consequences of doping effect on the electrical properties. This sub-section is a key to introduce the influence of point defects in the macroscopic properties of ferroelectric materials induced by doping, e.g. via the Positive Temperature Coefficient of Resistivity (PTCR) behaviour [9]. An important part of this thesis is indeed focused on the comparison between surface properties of undoped and Nb-doped $BaTiO_3$ (donor dopant). Afterwards, stoichiometry changes in the near surface region observed under annealing treatments are also described since we have investigated the effect of extensive thermal annealing on chemical composition of our $BaTiO_3$ thin films. Finally, the last part of this chapter describes the main differences encountered in thin films compared to ceramics or single crystal materials which are our basic motivation.

The second chapter reports the main characterization methods and thin films preparation used along this study. Thin films have been deposited using R.F magnetron sputtering and mostly characterized by photoelectron and impedance spectroscopy. This chapter is mainly describing the typical informations which can be extracted from the photoemission spectra in $ATiO_3$ oxides.

The third chapter contains the major results of the thesis which are discussed through five sections. The first section is related with surfaces of sputtered $BaTiO_3$ thin films and interface studies of metal contact formation with typical top and bottom electrodes. Using in situ XPS, we have evidenced the formation of interface barrier which depends on many parameters like the type of metal used for the electrode formation or the thermal treatment. We also show that the interface properties are highly sensitive to the amount of donor dopants which can be either in the $BaTiO_3$ films or in the substrate. We confirmed that platinum is not a good contact for donor doped $BaTiO_3$ while indium provides a good ohmic contact for PTCR system. After having investigated the contact formation, we show in section 2 the actual dielectric properties of such stacks. Then, the third section describes in details surface segregation phenomena observed in donor-doped thin films which are compared with typical behaviour of donor-doped ceramics. Such surface segregation resulting from the compensation of heterovalent substitution has been largely mentioned in the literature [10]. We show here that XPS is able to directly probe such segregation. The fourth section is also comparing thin film and bulk surface properties when subsequently annealed. It has been demonstrated that stoichiometry change occurs in the near-surface region under thermal treatment. Finally, the last section will discuss the much debated barium features typically observed in photoemission spectroscopy which is still largely discussed. This fifth section is voluntary lastly placed since its discussion is mainly speculative.

Corresponding literature

[1] J.F. Scott. (2007), *Science*. **395**, 954.

[2] J.F. Scott, and C.A. Paz de Araujo. (1989), *Science*. **246**, 1400.

[3] J.M. Gregg. (2009), *Phys. Status Solidi A.* **206**, 577.

[4] J. Junquera, and P. Ghosez. (2003), *Nature*. **422**, 506.

[5] B. Cord, and R. Courths. (1985), *Surf. Sci*. **152**, 1141.

[6] J.D. Baniecki, M. Ishii, T. Shioga, S. Miyahara, and K. Kurihara. (2006), *Appl. Phys. Lett.* **89**, 162908.

[7] R. Schafranek. (2009), *Thesis*, Kathodenzerstäubte (Ba,Sr)TiO_3- Dünnschichten für steuerbare Mikrowellenkomponenten Material-, Bauteil- und Grenzflächeneigenschaften, TU Darmstadt.

[8] V. Reymond. (2004), *Thesis.* Nouvelles couches minces et multicouches derives de $BaTiO_3$: optimisation des propriétés diélectriques, ICMCB of Bordeaux.

[9] W. Heywang. (1971), *J. Mat. Sc.* **6,** 1214.

[10] N.G. Eror and D.M. Smyth. in *The Chemistry of Extended Defects in Non-Metallic Solids,* edited by L. Eyring and M.O. Keeffe (North-Holland Pub.Co., Amsterdam, 1970), p62.

Contents

Chapter I

Ferroelectricity in bulk materials

1.1 Ferroelectricity in bulk materials

Dielectric materials have a strong influence on the evolution of electrical engineering, electronics, and information technology. They are typically crystalline or amorphous inorganic as well as organic compounds and polymers [1]. They are used as bulk materials and, most often, as thin-films. Ferroelectric materials are a sub-division class among dielectrics (fig. 1.1.1). Therefore, in this part the dielectric properties are going to be recalled first and the ferroelectric properties will be described later for bulk compounds.

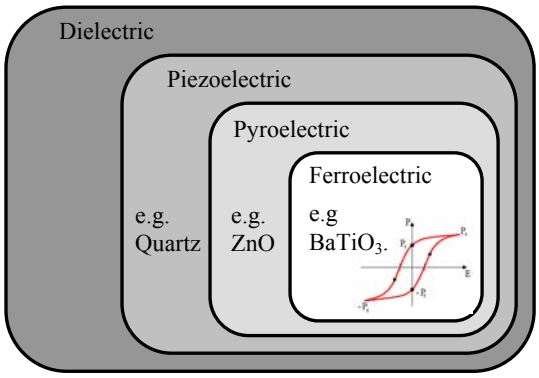

Figure 1.1.1: Sub-classes of dielectric materials with some key materials.

1.1.1 Dielectric Polarization

Dielectrics are insulating materials that are used because of their polarizability enabling increased charge storage in capacitors. They do not conduct electricity due to the very low density of free charge carriers. Spontaneous polarization results from the separation of the barycentres of positive and negative charges. If this separation is induced by an external electrical field, it is called dielectric polarization or polarizability.

In contrast, conductors such as metals do conduct electric current because of free mobility of the electrons within the lattice. If no charges are present in the material, conductivity requires that the charges can enter and leave the material and therefore contribute to the conduction phenomena through the conduction band level. Thus, we clearly see that a good dielectric (or good insulator) should have a relative high band gap to obtain low equilibrium charge carrier density and high injection barriers at the contacts.

This chapter will start with a brief description of the macroscopic and microscopic dielectric polarisation [2].

1.1.1.a Macroscopic and microscopic polarization

In accordance to the Poisson equation, the source of the dielectric displacement **D** is given by the density of charges ρ:

$$\text{div } \mathbf{D} = \rho \tag{1.1}$$

Equation (1.1) shows that electric displacement can be considerably increased from charges in the materials.

Based on this relation, the global charge neutrality of matter within an external field is described by:

$$\mathbf{D} = \varepsilon_0 \mathbf{E} + \mathbf{P} \tag{1.2}$$

ε_0 **E** represent the vacuum contribution induced by the externally applied electric field, **P** is the electrical polarization of the matter. It is important to note that **P** can be induced by pyroelectric polarization, piezoelectric polarization, ferroelectric polarization or dielectric polarization (by an external electric field).

For a pure dielectric material, the polarization is proportional to the electric field in linear approximation by:

$$\mathbf{P} = \varepsilon_0 \chi_e \mathbf{E} \quad \text{or} \quad \mathbf{D} = \varepsilon_0 \varepsilon_r \mathbf{E} \tag{1.3}$$

Here, the material properties are:
χ_e is the electrical susceptibility,
ε_r is the relative dielectric constant with $\varepsilon_r = 1 + \chi_e$,
For many dielectrics, χ_e and ε_r are field-independent. However, large electric fields can lead to strong non-linear dielectric properties. Therefore tunable dielectrics are achieved. From the

device point of view, this property (tunability) is particularly interesting as the capacity to store charges can be tuned by varying the voltage [3]. We can note that in ferroelectric materials, the variation in ε_r leads to a hysteresis behaviour as shown in Figure 1.1.2.

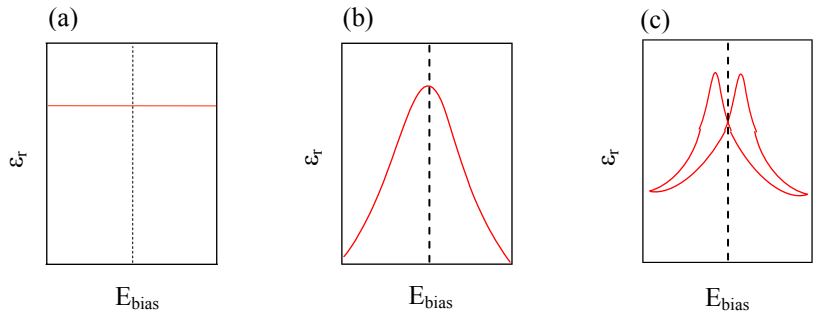

Figure 1.1.2: Bias field dependence of the dielectric constant of (a) typical dielectric, (b) tunable dielectric and (c) ferroelectric material.

We are now going to discuss the correlation between the macroscopic polarisation **P** and the microscopic properties of the material. The macroscopic polarisation **P** is the sum of all individual dipole moments $\mathbf{p_a}$ with their density $\mathbf{N_a}$. The contribution can be described by:

$$\mathbf{P} = \sum_{a} \mathbf{N_a}\, \mathbf{p_a} \tag{1.4}$$

If we consider a single (polarizable) particle, and if the particle is put into an electric field, the dipole moments are induced by the local electric field $\mathbf{E_{loc}}$ at the dipole site:

$$\mathbf{P} = \mathbf{N_a}\, \alpha\, \mathbf{E_{loc}} \tag{1.5}$$

α is the polarizability of an atomic dipole. In condensed matter, the electrostatic interactions between the microscopic dipoles make the local electric field different from the external macroscopic one $\mathbf{E_a}$, i-e, $\mathbf{E_{loc}} \neq \mathbf{E_a}$:

$$\mathbf{E_{loc}} = \mathbf{E_a} + \sum \mathbf{E_{dipole}} \tag{1.6}$$

Therefore, the local field is higher than the macroscopic field inside the dielectric due to contribution of all dipoles.

So far, another field has been voluntary neglected since dipoles were only considered parallel oriented along the applied electric field. This hypothesis is true for example when the

dielectric structure is face-centered cubic. Thus, the barycentre of positive and negative ions is uniform in all the directions (isotropic contribution) assuming that field induce by the atoms $\mathbf{E_{atoms}} = 0$. We are going to see for ferroelectric materials, e.g. $BaTiO_3$, $\mathbf{E_{atoms}}$ can not be neglected anymore even in the cubic phase due to strong directional dependence of the oxygen neighbourhood (strong anisotropy) [3].

One of the first reasons is related to the nature of the covalent Ti – O bonds and most specifically, to the nature of charge coordination in TiO_6 octahedra. In a perfect cubic structure, the oxygen ion electronic orbitals are perfectly spherical. The distances between these charges and the charges surrounding the Ti are all the same, see figure 1.1.3 (a).

But in real $BaTiO_3$ cubic structure, it has been shown from diffraction experiments [3] that titanium atoms are not located in the center of the oxygen octahedron but are displaced in the {111} direction and jump between eight equivalent sites (b). This effect is highly anisotropic and is created within the crystal through long-range interactions which lead to the formation of long dipole chains in the $\mathbf{E_{atoms}}$ direction (c).

The covalency model in perovskites has been well described by H. Thomann [4] to explain such intrinsic anisotropy of oxidic perovskite network.

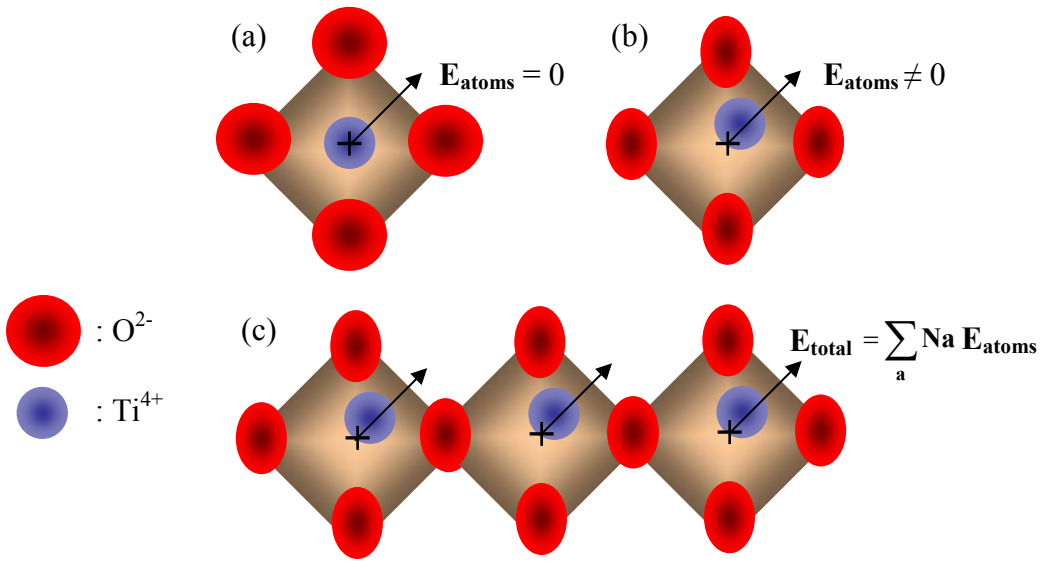

Figure 1.1.3: TiO_6 octahedra arrangements for (a) ideal covalent TiO bonds, (b) nonideal covalent TiO, (c) long-range contribution inducing an appreciable $\mathbf{E_{total}}$

1.1.1.b Mechanism of Polarization

Let us now deal with the behaviour of a dielectric material in alternating electric field. When a constant electric field is applied on the electrodes, the polarizable species within the dielectrics are oriented to the same field direction. If an alternating electric field (e.g. sinusoidal wave) is applied, the same species are going to follow the polarity change but with a certain relaxation time. There are as much relaxation times as number of polarizable species. Therefore, the dielectric response is not instantaneous but time dependant. To express this mathematically, the relative dielectric permittivity is written as a complex function:

$$\boldsymbol{\varepsilon}_r = \boldsymbol{\varepsilon}_r' + i\,\boldsymbol{\varepsilon}_r'' \tag{1.7}$$

The real part ε_r' characterizes the ability to store charges in the dielectric, and the imaginary part ε_r'' is the contribution of charge dissipation (dielectric loss). We clearly see that an ideal capacitor will have a high ε_r' value (High-K is commonly used) and low dielectric losses. Dielectric losses are usually described by the loss tangent:

$$\tan\delta = \frac{\boldsymbol{\varepsilon}_r''}{\boldsymbol{\varepsilon}_r'} \tag{1.8}$$

Away from resonances, it should be emphasized that the loss factor (tan δ) is caused by two contributions:

- the dipole reorientation,
- the residual leakage current of the non-perfect insulator.

Therefore, it is important to distinguish both contributions and they can be separated experimentally because of their distinct frequency and temperature dependence. For instance, the residual leakage current (or conductivity) contribution is well-known to occur at low frequency and high temperature. At low frequency, the loss factor can be described as follow:

$$\tan\delta = \frac{\sigma}{\omega.\boldsymbol{\varepsilon}_r''} \tag{1.9}$$

Thus, the relative dielectric permittivity expressed in (1.7) can be described more precisely as:

$$\boldsymbol{\varepsilon}_r = \boldsymbol{\varepsilon}_r' + i\,(\boldsymbol{\varepsilon}_r'' + \frac{\sigma}{\omega}) \tag{1.10}$$

Where σ denotes the conductivity at low frequency and ω pulsation ($\omega = 2\pi f$).

At higher frequencies, we can distinguish four contributions to the total polarisation of a dielectric material. They are discussed below. Each one contributes to the dielectric response but in different frequency regimes since they involve different polarizable species. The dispersion of the real and imaginary part of the dielectric function is schematically plotted in Figure 1.1.4. The relation between the real and imaginary part is evidenced in every frequency range. The conductivity reported previously is indicated by the arrow in the imaginary part.

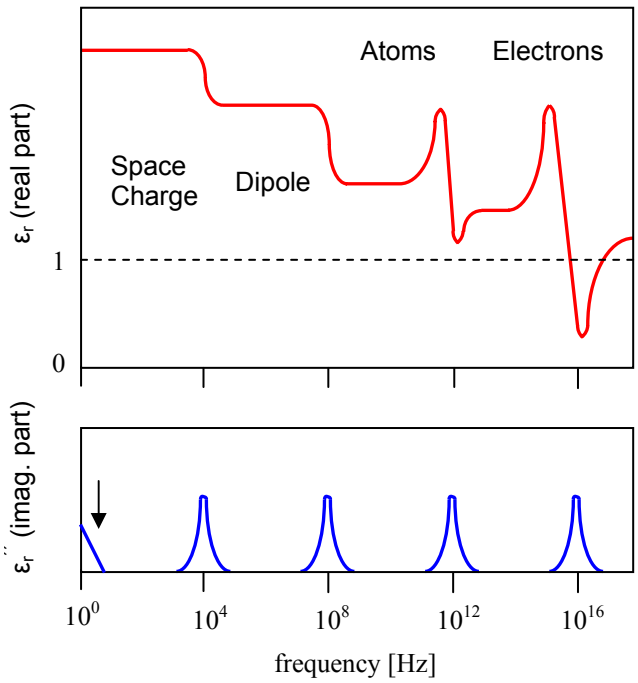

Figure 1.1.4: Frequency dependence of real (top) and imaginary (bottom) part of the dielectric function. The narrow indicates the conductivity contribution.

Space charge polarisation (10^0 – 10^4 Hz) could exist in dielectric material if the density of charge carrier is not homogeneously distributed. The most common case is the *pn* junction in semiconductor devices since the p-doped and the n-doped region induce charge depletion at their interface [5]. The space charge can also occur at the metal/dielectric interface, at grain boundaries in ceramics and domain walls in ferroelectrics. Thus, interfaces play a crucial role in the space charge effect but this extrinsic polarisation is much more pronounced if charged defects are localised at these interfaces. Therefore, space charge polarisation can be predominant in the dielectric properties if both free charges and interfaces are gathered. This polarization is also known as Maxwell-Wagner polarization.

Dipolar polarisation (10^4 – 10^8 Hz) characterizes the alignment of permanent dipoles as a function of the applied polarity. An electric field generates a preferred orientation for the dipoles, while the thermal fluctuation perturbs the dipole alignment. The average degree of orientation is a function of the applied field and the temperature. The mathematical expression is given by the so-called *Langevin function*:

$$\mathbf{P_d} \approx \coth(y) - \frac{1}{y} \qquad \text{with} \quad y = \frac{pE_a}{kT} \tag{1.11}$$

$\mathbf{P_d}$ describes the polarization of the dipoles, p indicates the permanent microscopic dipole moment, E_a defines the applied electric field, k denotes the Boltzmann constant and T the absolute temperature in Kelvin. By plotting $\mathbf{P_d}$ versus y, the polarisation shows saturation at very high field but is proportional to E for lower values.

Ionic Polarisation (Atoms): If the dielectric is described by ionic bonds, the displacement of positive and negative ions under electric field generate ionic polarisation (e.g. NaCl). As a result, when lattice vibrations or molecular vibrations induce relative atomic displacements, the centres of positive and negative charges might be in different locations. These center positions are affected by the symmetry of the displacements. When the centers do not correspond, polarizations arise in molecules or crystals. This polarization is called **ionic polarization**. Ionic polarization may induce **ferroelectric transition** as well as **dipolar polarization.** Because Ionic polarization is induced by lattice vibrations (phonons), the resulting dielectric dispersion is resonant at the phonon frequency, at variance from the two previous cases of relaxation.

Electronic Polarization: exists in all materials. It is based on the displacement of the negatively charged electron shell against the positively charged core. This displacement occurs due to the equilibrium between restoration and electric forces. **Electronic polarization** may be understood by assuming an atom as a point nucleus surrounded by spherical electron cloud of uniform charge density. In a solid, the resonance frequencies correspond to electronic inter- and intraband transitions.

The **depolarization field** (E_{depol}): If a ferroelectric material is polarized, a compensating depolarization potential across the material take place to ensure that the whole system is equipotential. This mechanism occurs differently if electrodes are sandwiching the

ferroelectric or not. Therefore, two situations can be envisaged. The case of unsandwiched ferroelectric and stacked ferroelectric, respectively illustrated Fig. 1.1.5 in (a) and (b). In the first case, polarization charges ± P reside on opposite faces to the electric dipoles. The magnitude of the electric field created by these charges is:

$$E_{depol} = \frac{P}{\varepsilon_0 \varepsilon_r} \tag{1.12}$$

where P is the ferroelectric polarization, $\boldsymbol{\varepsilon}_o$ is the vacuum permittivity and $\boldsymbol{\varepsilon}_r$ is the relative permittivity of the ferroelectric material discussed above. E_{depol} opposes large ferroelectric polarization because it grows in proportion to P. (a) is thus the situation for uncompensated polarization charges. Ferroelectrics are often studied in capacitor structures (b).

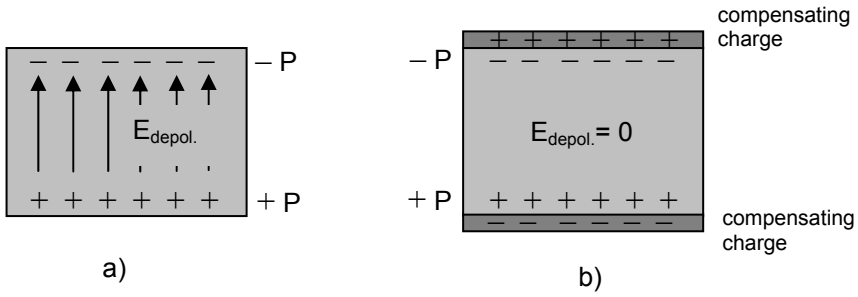

Figure 1.1.5: (a) A depolarization field ($E_{depol.}$) arises in an isolated ferroelectric, due to uncompensated polarization charges (P) on opposite faces of the material. (b) Metal electrodes provide a source of compensating charges, which cancel $E_{depol.}$

When metal plates are placed on opposite faces of the ferroelectric, the polarization charge attracts charges of opposite polarity from the metal. If it is possible for compensating charge (into the metal) to move into close proximity to the ferroelectric surface, E_{depol} can be eliminated. For these compensating charges, the ability to move toward the interface is directly related to the *electron screening length* (ESL) in the metal [7]. Therefore, electrode with low carrier density (low ESL), can result in insufficient charge near the ferroelectric/electrode interface, leaving a residual depolarization field [8]. Oxide electrodes, known for reducing ferroelectric fatigue [9], would not be optimal for thin devices due to their *finite electron screening length* [10]. Elemental electrodes like Pt or Au over $SrRuO_3$ or Nb-doped $SrTiO_3$ were found to exhibit better screening properties of the electrodes [11].

In the next paragraph, we are going to see an example from literature on ferroelectric thin films showing that it is delicate to distinguish between intrinsic and extrinsic origins of polarization.

Let us now deal briefly with relaxation phenomena through dielectric model (especially *Debye* model and *Maxwell-Wagner* model) used to indentify the polarization origin.

1.1.1.c Relaxation Phenomena

Debye relaxation [12] is a very simple model where only two polarizable species are assumed in the dielectric. Thus, the dielectric parameters will undergo a single relaxation time τ which denotes the transition time between one species and the other one. Both are contributing to the dielectric response but at different frequencies. Let us take the example of a ceramics including two possible dielectric contributions; one from grain boundaries and the other from the grains. Each contribution is usually represented using the impedance diagram (–Z'' vs. Z'), see figure 1.1.6 (b). They can also be represented by an equivalent circuit also depicted in Figure 1.1.6. Both contributions can be easily distinguished with the impedance diagram but the relaxation process between them can only be evidenced using the Cole-Cole diagram [13] by plotting $\boldsymbol{\varepsilon}_r''$ vs. $\boldsymbol{\varepsilon}_r'$. Finally, it is important to note that if only one species is considered in the dielectric, no mechanism of relaxation has to be expected (see figure 1.1.6 (a)).

The *Debye relaxation* is usually expressed in the complex permittivity $\boldsymbol{\varepsilon}$ of a medium as a function of the field frequency ω:

$$\boldsymbol{\varepsilon}(\omega) = \boldsymbol{\varepsilon}_\infty + \frac{\varepsilon_s - \varepsilon_\infty}{1 + i\,\omega\tau} \tag{1.13}$$

Where $\boldsymbol{\varepsilon}_\infty$ is the high frequency permittivity, $\boldsymbol{\varepsilon}_s$ is the low frequency permittivity (static) and τ describes the characteristic relaxation. In the case of a pure Debye relaxation the plot of $\boldsymbol{\varepsilon}_r'$ and $\boldsymbol{\varepsilon}_r''$ vs. the frequency is recalled figure 1.1.7.

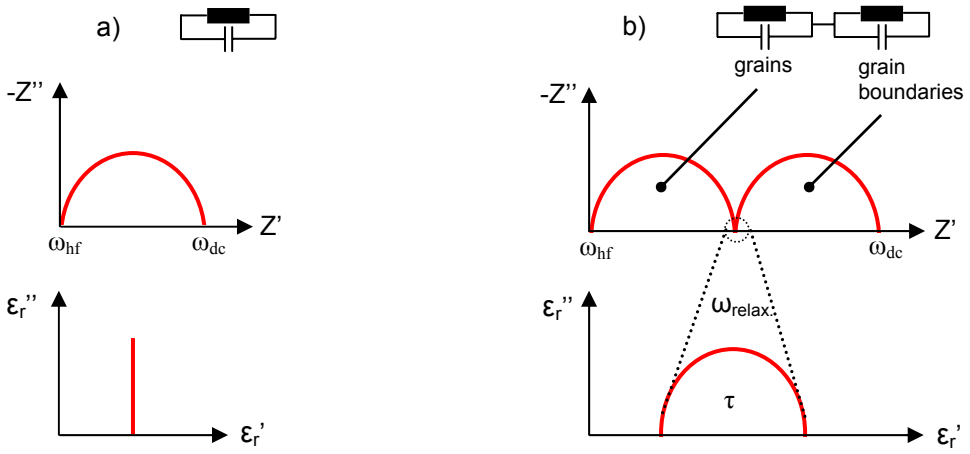

Figure 1.1.6: Impedance diagrams (top) and Cole-Cole diagrams (bottom) for one polarizable specie in the dielectric a) and typical *Debye* relaxation with two polarizable species b). Impedance diagram is not an appropriate plot to observe the relaxation process.

Maxwell Wagner (MW) effect is commonly involved if a material is electrically heterogeneous. This dispersion occurs because of the charging of the interfaces within the material. This phenomenon does not arise from dielectric relaxation in the bulk phases of the material (which might also be present), but is a consequence of the boundary conditions on the fields at the interfaces between phases. Interfacial effects typically dominate the dielectric properties of doped-$BaTiO_3$ [14], when free charges induce by doping are located at the interfaces (grain boundaries, domain walls, electrodes). The typical *Maxwell Wagner* behaviour is plotted in figure 1.8. In a MW system, the real part is the same as in *Debye* relaxation. Analysis of the real part of relative permittivity is therefore not useful for identification of interfacial polarization effects. On the other hand, analysis of the imaginary permittivity does distinguish *Debye* from MW behaviour.

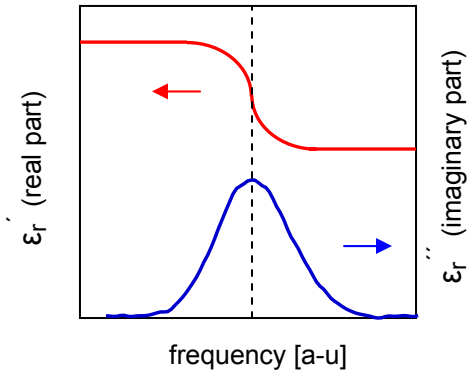

Figure1.1.7. Frequency dependence of real and imaginary part for the case of Debye-type relaxation process.

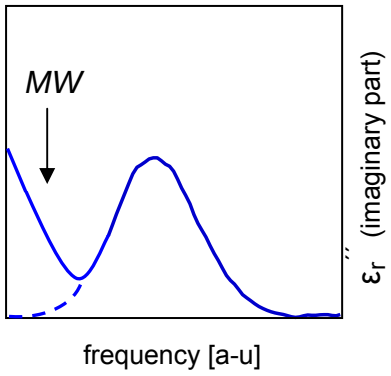

Figure1.1.8. Form of the imaginary permittivity response expected from both *Maxwell Wagner* and *Debye* models

In particular $\varepsilon_r'' \mapsto 0$ as $f \mapsto 0$ in a *Debye* system, whereas in a MW system $\varepsilon_r'' \mapsto \infty$ (see figure 1.1.7 and 1.1.8). We note that some authors underrate such low frequency behaviour. Typical discussion on interfacial polarization is presented below.

We now show one example of MW relaxation in an integrated ferroelectric. Thin-film capacitors in which the dielectric layer is composed of superlattice of $Ba_{0.8}Sr_{0.2}TiO_3$ and $Ba_{0.2}Sr_{0.8}TiO_3$, have been studied using impedance spectroscopy [15]. Giant permittivity of intrinsic origin (motion of domain walls) was claimed in this paper. At low frequencies, permittivities as high as 420 000 were measured (figure 1.1.9). Nevertheless, dielectric analysis performed at lower frequency, reported by O´Neil *et al.* [16], have revealed an increase of the imaginary part in agreement with *Maxwell Wagner* polarisation (see figure 1.1.10), most probably due the numerous interfaces in this superlattice structure. Change in carrier mobility in defect zone can therefore enhance considerably the permittivity properties and MW behaviour cannot be ruled out to explain giant permittivity values often observed in superlattices structures.

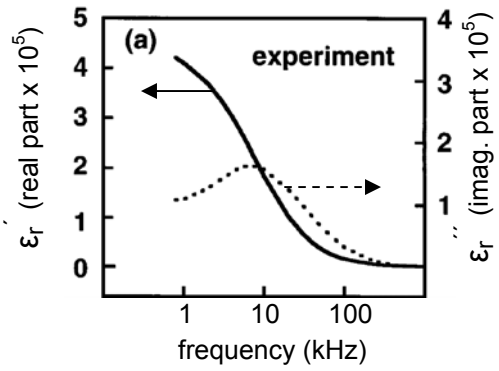

Figure1.1.9: Frequency dependence on a logarithmic scale of real and imaginary parts of the superlattice after [15].

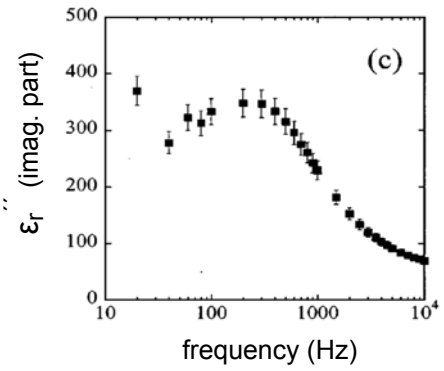

Figure1.1.10. Frequency dependence on a logarithmic scale of real and imaginary parts for the same superlattice but at lower frequency [16].

We have given here a short description of different polarization mechanisms in dielectrics. The entire spectrum from the dc response to the optical frequencies was covered. The dc and low-frequency response are dominated by displacing charged ions or space charges within the materials. For higher frequency, only the electrons are able to follow the rapid changes of the electrical fields. We saw that the dielectric polarization can have different origins which are sometimes difficult to distinguish. Impedance spectroscopy can be used to probe such mechanisms but a broad temperature/frequency range of investigation is often necessary to discriminate the contributions.

We are now going to consider dielectric crystals which show a spontaneous electric polarization and in which both crystallographic states and temperature can influence this intrinsic polarization.

1.1.2 Ferroelectric Polarization

This section is focused on dielectric crystals which show a spontaneous electric polarization. Phenomenology of Ferroelectrics, temperature dependence and electrical properties will be discussed. Among the different ferroelectrics, we will focus on the oxide materials. The topic of this paragraph has been largely covered in many textbooks such as [17,18].

Barium titanate, the first ceramic material in which ferroelectric behaviour was observed, is the ideal system for a discussion of the phenomenon from the point of view of crystal structure and microstructure. Figure 1.1.11 displays the crystal structure of cubic $BaTiO_3$.

Upon cooling from high temperatures, a solid state phase transition occurs during which the positive and negative ions displace with respect to the other, leading to tetragonal deformation. Due to the change of the barycentre of positive and negative charges (Ti^{4+} moves towards one of the six O^{2-} neighbours), a spontaneous polarization (oriented to the tetragonal axis) appears. The permittivity value is also drastically modified at the transition temperature (T_c ~120°C): it increases well above 10 000 as depicted on figure 1.1.12. If the inverse of susceptibility $(\varepsilon_r')^{-1}$ is plotted as a function of the temperature, a linear relation is obtained within the cubic phase with $(\varepsilon_r')^{-1}$ reaching zero below the transition temperature (T_c). Additional phase transitions occur as well for lower temperature (Rhombohedral and Orthorhombic).

There are several directions for ferroelectrics research and applications [19]: substrate-film interfaces and high strain states, finite size effects, nanotubes and nanowires, core-shell, electrocaloric devices, ferroelectric random access memories (FeRAMs), tunable capacitors, dynamic random access memory (DRAM) capacitors, electron emitters, weak-magnetic field sensors and super-capacitors. Tunable thermistor properties in semiconducting ferroelectrics are also used in PTCR applications (Positive Thermal Coefficient of Resistivity) [20], in which the drastic change of resistivity (~ 8 decades) in dependence on temperature is one of the most important non-linear properties in physics of solid state materials.

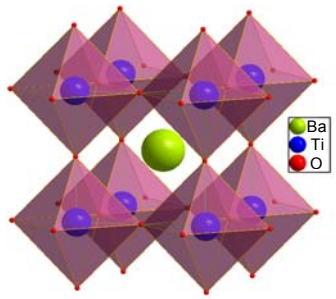

Figure 1.1.11. Unit cell of cubic $BaTiO_3$ (perovskite structure). The central Ti^{4+} ion is surrounded by six O^{2-} ions in octahedral configuration.

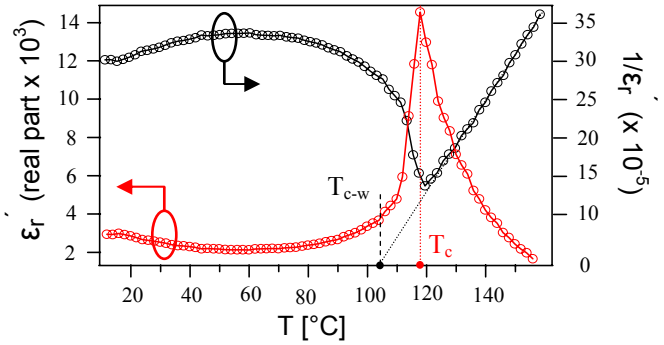

Figure 1.1.12. Real part of the permittivity vs. temperature for $BaTiO_3$. The inverse of the permittivity is also plotted. T_c denotes the transition temperature and T_{c-w} the Curie-Weiss temperature.

The present section includes the following sub-sections:

- We are going to see first some thermodynamics of ferroelectrics showing their anisotropic properties as a function of the temperature (structure, lattice constants, spontaneous polarization and relative permittivity), and ferroelectric domains.
- Thereafter, we will briefly discuss the Landau-Ginsburg phenomenological model used to explain the phase transition at a macroscopic level.
- Then, we will have a look on basic compositions and size effects commonly studied in bulk materials.

1.1.2.a Thermodynamics

Spontaneous polarization is necessarily related to the crystal symmetry. Ferroelectric crystals can be classified in several families according to their: (i) structures, (ii) Curie temperature values and (iii) spontaneous polarisation values. These crystallographic considerations are out of the scope of this work but a detailed report is available thanks to the work of Walter J. Merz [21]. Here are some typical ferroelectric structures extracted from the Kittel book [2] as the Rochelle salt [22], $FeTiO_3$ [23] commonly recognised as an **ilmenite structure**, **pyrochlore crystal structure** like $La_2Zr_2O_7$ and the archetypical structure named **perovskite structure** as $CaTiO_3$ or $BaTiO_3$ [24].

The spontaneous polarization of a ferroelectric crystal can be reoriented by an external electric field modifying the crystallographic configuration and thus, the barycentre of positive and negative charges. We have to note that the analogies with ferromagnetic materials (polarisation/magnetisation, dielectric permittivity/magnetic susceptibility, etc…) have defined the term: **Ferroelectricity** [22]. But this analogy remains limited since the polarisation requires lattice distortion and magnetisation does not. The coupling between the crystallographic configurations and the external electric field, lead to the well known **hysteresis loop** which occurs when ferroelectric states are switched. The hysteresis loop of a single crystal and that of a ceramic are shown in figure 1.1.13.

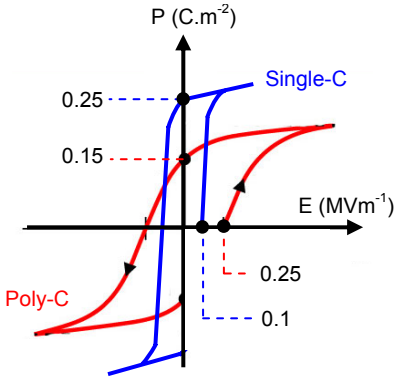

Figure 1.1.13. Blue: Hysteresis loops for a single crystal of $BaTiO_3$. **Red**: Polycrystalline $BaTiO_3$. [17]

For the single crystal loop, the almost vertical portions of the loop are due to the reversal of spontaneous polarization induced by domain reversal and growth. The almost horizontal portions represent saturated states in which the crystal is in a single domain state. Typically, the **coercive field** at room temperature is 0.1 $MV.m^{-1}$ and the **saturation polarization** is 0.27 $C.m^{-2}$ for $BaTiO_3$ [17]. In poly-crystal ferroelectric materials, e.g. ceramics, we have to keep in mind a statistical orientation of the grains. The coercive field is thus higher (more energy is necessary to switch these poly-domains) and the saturation as well as remanent polarization are lower than for a single crystal (all the grains are not entirely oriented in the polarization direction).

To consider the various properties of ferroelectric materials, barium titanate will only be discussed to define the anisotropic properties as shown in figure 1.1.14.

The phase transition in barium titanate is of first order (see figure 1.1.12), and as a consequence, there is a discontinuity in the polarization, lattice constant, dielectric constant as evidenced on figure 1.1.14. This first order behaviour is also evidenced by a small thermal hysteresis of the transition, which depends on many parameters such as mechanical stress, crystal imperfections, or impurities. Upon cooling from high temperature, the following sequences occur: **cubic** to **tetragonal** structure (spontaneous polarization in the [100] direction), **orthorhombic** structure (polarisation along the [110] direction) and finally, a **rhombohedral** structure (polarization is in the [111] direction).

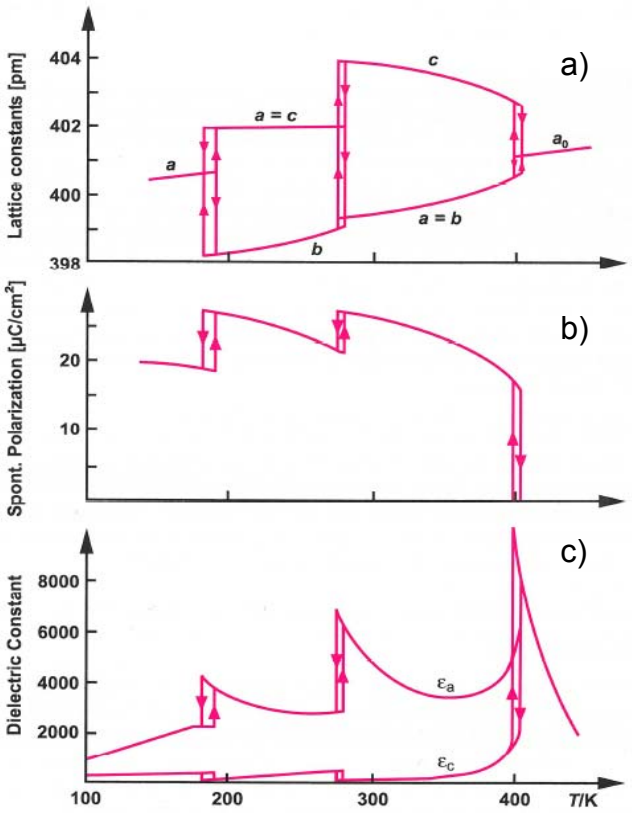

Figure 1.1.14: Properties of barium titanate as a function of the temperature:
a) unit-cell distortions lattice dimensions after [26]
b) spontaneous polarization
c) relative permittivities measured in the *a* and the *c* direction after [27].

When a ferroelectric single crystal is cooled below the phase transition temperature, ferroelectric domains appear. These domains define regions of homogeneous polarization separated by walls of well defined geometry. Figure 1.1.15 is a typical micrograph showing the domains in a single grain [28]. Ferroelectric domains are not necessarily defined by a grain and several grains can have the same crystallographic orientation, thus contributing to form a unique domain. Domain walls typically appear along specific crystallographic planes which satisfy the mechanical compatibility conditions. In order to avoid internal stress, these domains or twins can only be arranged one against each other in certain ways to form domain walls, which can be of ± 180° or ± 90°, giving rise to well defined structures. Now, let us see an example of domain formation in thin films. Recently, investigation of strain effect, which arises mainly from the mismatch of lattice parameters and from different thermal expansion coefficients between thin films and substrate, has become increasingly important due to its great influence on the domain formation for ferroelectric thin films [29,30,31]. Figure 1.1.16 displays a typical investigation on domain configuration for thin films of $BaTiO_3$ on tensile substrates [29] showing poly-domains configurations, currently observed in such structure.

Nowadays, one of the main scientific challenges is to identify the effects produced by applying an external electric field, i.e, does it induce intrinsic or extrinsic effects [32]. Intrinsic effects consider the deformation of the unit cell, whereas extrinsic effects consider the displacement of domain walls. The distinction between both contributions is sometimes not straightforward [33].

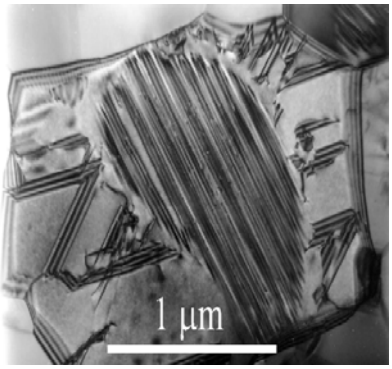

Figure 1.1.15: Single representative grain within a polycrystalline ceramic. The core region shows ferroelectric domains from tetragonal phases of $BaTiO_3$ after [28].

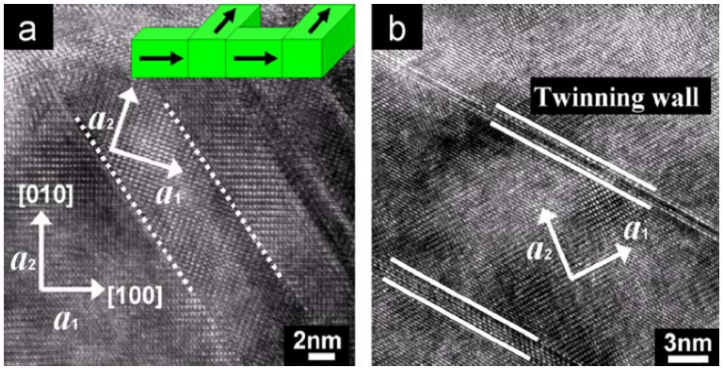

Figure 1.1.16: Plan-view HRTEM images for 200nm (a) and 400nm (b) BTO thin films deposited on Si. Inset of (a) shows the suggested schematic *a1/a2/a1/a2* poly-domains configurations. In addition, with increasing BTO thickness, both the width of domains and domain walls are increased due to size effect. After [29].

Very recently, an artificial magneto-capacitance coupling has been established which is taking the advantage of the interaction between domain wall dynamics and charged defects to induce such coupling [34]. Indeed, we have to point out that domain walls in oxide materials (bulk or thin film) can localise free charges which might induce conductive behaviour in originally insulating materials [35], leading to novel routes towards potential nanoelectronic applications.

We just described some thermal properties in ferroelectric materials (anisotropy, temperature dependence, ferroelectric domain and domain wall). They are driving the electrical properties (permittivity, tunability, polarisation, resistivity), and can be considerably affected if defects are introduced (see chapter 1.2) and/or if the material considered is in thin film form (see chapter 1.3). Let us now summarize the different phenomenoligical models commonly used to describe the ferroelectric phase transitions.

1.1.2.b Theoretical models

There are several theoretical approaches which "partially" describe the phase transition in ferroelectrics materials. A phenomenological model has been established by Landau and Ginzburg [36] introducing the polarisation **P** as an order parameter. Cochran [37] has developed the soft mode approach of displacive phase transition, involving optical vibration modes. Then, the shell model [38] was used to consider the anisotropic polarizability of the oxygen O^{2-}, which explained several features of ferroelectrics but did not provide an explanation for the differences between $BaTiO_3$, $PbTiO_3$ and $SrTiO_3$. Nowadays, ab-initio calculations are employed to provide an in-depth analysis of orbital hybridization states [39], electronic density mapping [40] and interfacial effects responsible for destabilizing the ferroelectric state in ultrathin-film devices [41].

In the present paragraph, we are going to describe the theory of the Ferroelectric Phase Transition through the Landau-Ginzburg model.

Ginzburg-Landau Theory

The model describes the thermodynamics of the ferroelectric phase transition. In physics, this mathematical expression has been also used to model superconductivity or magnetism. It describes some of the phenomena of phase transitions without explaining the underlying microscopic mechanism. But the theory is very useful to understand macroscopically the polarisation change near the phase transition temperature (T_c). Close to the phase transition, the Gibbs energy P (Polarisation and Temperature related) may be expanded in powers of the order parameter P:

$$P = P_0 + aP^2 + bP^4 + cP^6 - \mathbf{P.E} \qquad (1.14)$$

Where $a = k(T - T_c)$

If $b > 0$, the transition is of second order phase transition (e.g. $BaTiO_3$), and if $b < 0$ the ferroelectric transition is a first order phase transition (e.g. $LiTaO_3$). We underline that the phase transition covered by this model is restricted to the paraelectric/ferroelectric transition. Figure 1.1.17-a) schematically displays the free energy F for different temperatures as a function of the polarisation for both first and second order transitions. By inspecting graph a), we clearly see a difference between first and second order. When $T >> T_c$, only one

equilibrium position is possible for the free energies at P=0, identifying the paraelectric state. But for temperatures closer to the transition, the first order exhibit several intermediate states in contrast with the finite values reached by the 2nd order. There is a direct consequence on the polarisation behaviour in dependence on temperature where the first order transition is much more abrupt (see graph (b)). This results from the co-existence of several stable states (P=0 and P≠0). Plotting the inverse of the permittivity vs. the temperature (graph (c)) with the linear extrapolation reaching zero below T_c, gives the Curie-Weiss temperature ($T_{c\text{-}w}$). Between T_c and $T_{c\text{-}w}$, secondary minima at finite polarizations become visible. When $T = T_c$, we reach the situation where all three minima of the free energy are at the same level. "Up" and "Down" indicate both stable ferroelectric states used to store electrical information. In 2nd order transition, T_c and $T_{c\text{-}w}$ are superimposed.

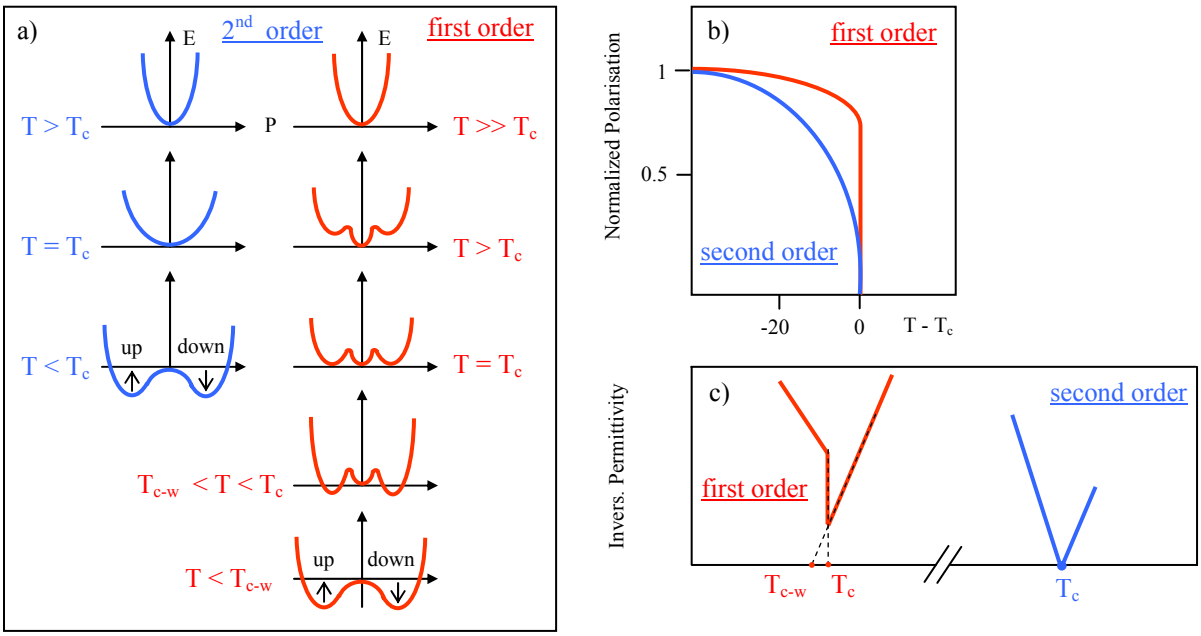

Figure 1.1.17: a) Free energy of a ferroelectric with a second-order phase transition (blue) and with a first order phase transition (red) at different temperatures. T_c denotes the phase transition temperature and $T_{c\text{-}w}$ is the Curie-Weiss temperature. b) Normalized Polarization for first and second order materials. c) Inverse of the permittivity for both order.

The Landau model does not take into account: (i) inhomogeneous field in the matter, (ii) is not applicable on finite solids and (iii) do not give microscopic information on the ferroelectricity.

Closing Remarks

Dielectric and Ferroelectric polarization, has just been described in the case of ideal materials (free of defects). Nevertheless, all these properties (e.g. transition temperatures) can be drastically modified by heterovalent or isovalent substitution [14], whether unwanted or intentionally included. For instance, appropriate amount of niobium in $BaTiO_3$ change drastically its resistivity from 10^{10} Ω.cm to 10^2 Ω.cm at room temperature [20]. The next paragraph will thus focus on charge defects induced by doping and their influence on electrical properties. Thereafter, the stoichiometry influence will also be discussed regarding the near-surface region where dramatic changes are observed.

1.2 Stoichiometry and charged defects in ferroelectrics

The addition of small quantities of impurities in an insulator or semiconductor has a dramatic effect on its conductivity. It is, of course, such extrinsic effects that are the basis of silicon semiconductor technology [6]. Ferroelectric materials are also sensitive to point defects [42]. Their electrical properties can be drastically modified by "extra charges" as can be seen on figure 1.2.1 for niobium doped $BaTiO_3$. In such ceramics, substitution of 0.02 weight percent of Ti^{4+} with Nb^{5+} results in a strong decrease of the room temperature resistivity by more than 4 orders of magnitude. High resistivity is partially recovered on crossing the ferroelectric transition temperature at about 400K. Such behavior, known as Positive Temperature Coefficient of Resistance (PTCR) [20], shows that electronic state of impurities is very important in ferroelectrics. However, as in many oxides, the amount of residual defects is orders of magnitude higher than in silicon crystals (100 ppm instead of 0.001 ppm). The term "high purity" is thus not applicable in oxide materials like ABO_3 ferroelectrics. In addition, they are often highly resistive at room temperature. Therefore, the study of semiconductivity in oxides has necessarily been carried out at high temperatures (> 500°C) making the setup design and the establishment of equilibrium more difficult. This paragraph will first deal with some typical doping effects and the consequences of free charges in electrical properties of ferroelectrics. We will finally describe the near-surface region of ABO_3 materials, also submitted to stoichiometry change, as observed under annealing treatment.

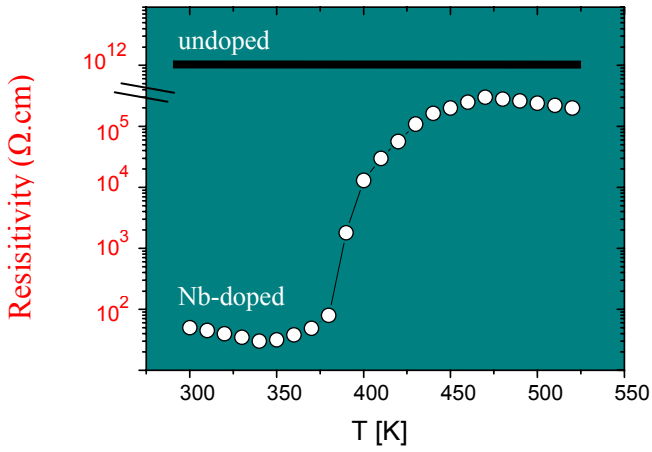

Figure 1.2.1: Resistivity change in $BaTiO_3$ ceramic induced by doping effect (Nb^{5+} 0,02 wt%). The jump of resistivity is starting at the Curie temperature [20].

1.2.1 Introduction

The discussion will most largely cover substitution of aliovalent cation impurities and their effects on the defect chemistry of $BaTiO_3$ in particular on the generation of free charges. Isovalent cations have no first order effect on such charges (i.e. the charge neutrality is not disturbed), and the anionic substitution is extremely rare.
First of all, we shall briefly see the conservation rules involved in the substitution mechanism, the typical jargon definition and the defect notation. We have to mention that extensive studies in defect chemistry of oxides have been done by D.M. Smyth [42].

These rules may be summarized as follows:

- If an ion is replaced by a different ion of the same valence, it is called *Isovalent* substitution (e.g. Sr^{2+}/Ba^{2+}). It is *Heterovalent* or *aliovalent* when the valence is different (e.g. La^{3+}/Ba^{2+}).
- Substituted cations are classified as *acceptor* centers if their charge is less than that of the cation they replace (e.g. Fe^{3+}/Ti^{4+}), and *donor* centers if they have a greater charge (e.g. Nb^{5+}/Ti^{4+}). In any case, the resulting charge must be electrically neutral (e.g, through O^{2-} gain/loss or generation of free electrons/holes).
- Dopant cations must have a very close oxidation state and ionic radii compared to the cation they replace (e.g. La^{3+} is too large to replace Ti^{4+} on the B-site).
- If the amount of impurities introduced in the perovskite structure is less than 1% atomic concentration, *doping* can be considered. For higher content, we commonly used the term *substitution*.

A wide variety of defect notations have been suggested in the literature but the self-consistent symbols proposed by Kröger and Vink [43] have been finally accepted as the most useful. The notations can be described as follows:

$$\mathbf{What}^{\text{charge}}_{\text{where}}$$

What: Which defect species (ion or a vacant site denoted by V).
Where: Indicates the lattice site occupied by the defect.

Charge: Indicates the charge difference between the defect and the substituted ion. A dot is used for an extra positive charge, and a slash denotes an extra negative charge.
For instance, V_{Ti}'''' denotes a Ti vacancy leading to four extra negative charges which have to be compensated, for instance via the loss of two oxygen: $2V_O^{\bullet\bullet}$.

In the following paragraph, we are going to describe two consequences of such doping in the electrical properties: (i) the "positive temperature coefficient of resistivity" (PTCR) effect, which is refereeing to the large increase of resistivity observed in doped $BaTiO_3$ in the vicinity of the Curie temperature (see fig. 1.2.1 above), and (ii) colossal dielectric properties observed in $CaCu_3Ti_4O_{12}$, where the equilibrium between Cu^{2+}, Cu^{+} and oxygen vacancies may play the same role of charged defects and induce a colossal increase of the permittivity but from extrinsic origin, i.e.; not from the bulk property. Both points will be useful in the course of this thesis since an important part of the work is devoted to the study of doping effect in $BaTiO_3$ thin films (see later III.3.2 and III.3.4). Finally, we will provide a description of the surface and the near surface region of stoichiometric perovskites at elevated temperature. The literature has indicated a rather complex behavior of the surface on prolonged annealing in the temperature range where conductivity increases. If the situation seems to be well documented for bulk materials, the results are much more speculative for thin films. This point will also be described in chapter III.3.2

1.2.2 Positive temperature coefficient resistivity (PTCR) in donor doped $BaTiO_3$

In 1955, *Haayman, Dam* and *Klasens* [44] found that $BaTiO_3$ can be transformed into a semiconductor by using Verwey's controlled valency method. The method consists of replacing partly Ba^{2+} ions by large trivalent ions like La^{3+}, or Ti^{4+} ions by small pentavalent ions like Nb^{5+} or Sb^{5+}. In all cases, the "extra positive charges" of the foreign ions change drastically the resistivity properties of $BaTiO_3$, especially at the Curie temperature. Studies of both single crystals and ceramics of samarium-doped $BaTiO_3$ [45] with identical compositions have shown that the PTCR effect is only present in polycrystalline material and thus related to grain boundaries. Some authors claim the non-necessary donor dopant additives to obtain a PTCR effect since grains and grain boundaries can be differently oxidized under certain circumstances [46]. The most accepted model to explain macroscopically the PTCR effect has

been established by Heywang [20] assuming a specific potential profile at surfaces and interfaces. The main results are summarized in fig. 1.2.2 and fig. 1.2.3.

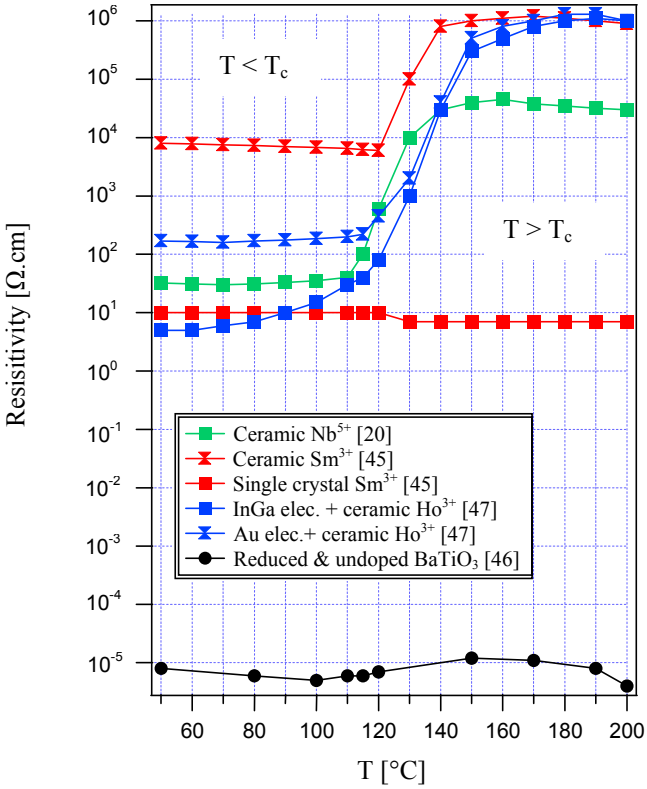

Figure 1.2.2: Resistivity versus temperature characteristics of $BaTiO_3$ containing various dopants. Ceramic and single crystal profiles are also compared. Different electrodes can change the resistivity profile, especially at low temperature. The conductivity property is also shown for undoped $BaTiO_3$ highly reduced.

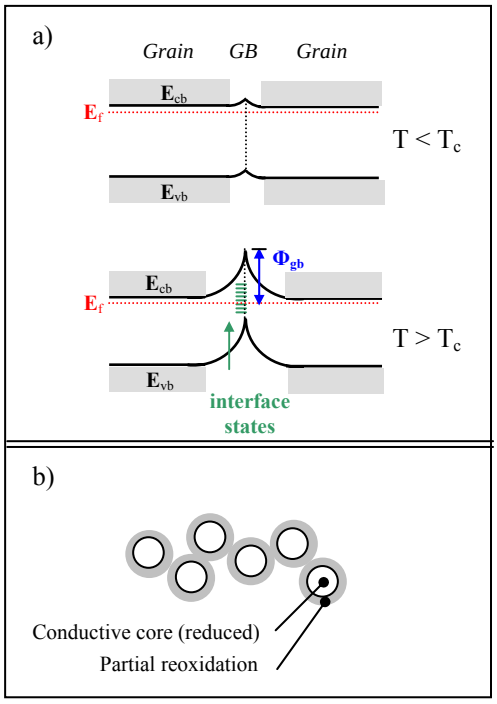

Figure 1.2.3: a) Energy level diagram near a grain boundary after Heywang [20] for doped $BaTiO_3$. The interface states induce a high Schottky barrier (Φ_{gb}) when $T > T_c$.
b) Schematic model of core-shell structures on partial reoxidation due to slow cooling in air after [46]. Here, donor dopants are assumed not essential to induce both semiconductivity and PTCR due to modifications to the oxygen content of the ceramics.

It is evident that the PTCR anomaly, absent from the doped single crystal, is restored in the ceramic of identical composition [45]. Also, from room temperature up to the Curie temperature, the resistivity of the ceramic is about three orders of magnitude larger than that of the single crystal. Thus, only the presence of grain boundaries can account for these differences.

The Heywang model (see fig. 1.2.3 (a)) assumes the presence of potential barriers (i) at metal contacts and (ii) at grain boundaries, both induced by surface/interface states which can be

thermally activated. But as the jump of resistivity takes place precisely at the Curie temperature, coupling between ferroelectric polarization and interface states is obvious. The polarization charges ($T < T_c$) in the ferroelectric phase could compensate the interface states at the grain boundaries (acceptor states). Therefore, these ferroelectric charges could cancel the potential barrier regions along the grain boundaries, resulting in a low resistivity. The resistivity jump at the transition temperature is then resulting from the release of such compensation.
This model has provided a good starting point for analysis and modeling of PTCR behavior in macroscopical view but the most interesting problem connected with this model is the nature of the interface states.

As for any semi-conductor interfaces, the first step is to understand the conductivity properties at both sides of the interface, which in the case of $BaTiO_3$ ceramics is the grain core conductivity. We are going to see now the proposed defect chemistry to explain the origin of semiconductivity. This topic has attracted a lot of interest and is still a matter of debate [48,49].

Since donor (La^{3+}) doping has been intensively reported in the literature, we are going to focus the description on La-doped $BaTiO_3$. Different mechanisms can be identified to understand the charge imbalance involved in doped $BaTiO_3$. The following defect reactions encountered in La-doped $BaTiO_3$ are using the notations of Kröger–Vink (KV), presented above. These notations only involve reactions to respect the charge neutrality in the ideal network (crystal) without taking into account the realistic system (grains + grain boundaries). The PTCR effect occurs in such system (polycrystalline materials). These notations do not inform on the new location of the displaced elements to maintain the charge neutrality. For instance, if a titanium vacancy is created to unbalance the extra charges, the new location of the expelled titanium will not be indicated in the (KV) notations, but only the vacancy site. The expelled Ti might form an extra-phase at the grain boundaries or interstitial defect (unlikely in perovskite structure). In fact, experimental investigations are required to complete these theoretical notations. But they at least provide a good starting point to study the defect chemistry of donor doped $BaTiO_3$ (ionic or electronic disorder).

$$4Ba_{Ba}^{x} + Ti_{Ti}^{x} \leftrightarrow 4La_{Ba}^{\bullet} + V_{Ti}^{''''} \qquad (2.1)$$

(2.1) indicates that Ti vacancies act as the charge-compensating defect (ionic compensation).

$$3Ba_{Ba}^{x} \leftrightarrow 2La_{Ba}^{\bullet} + V_{Ba}^{''} \quad (2.2)$$

(2.2) indicates that Ba vacancies act as the charge-compensating defect (ionic compensation).

$$Ba_{Ba}^{x} \leftrightarrow La_{Ba}^{\bullet} + e' \quad (2.3)$$

(2.3) indicates that injection of "extra" electrons could counter balance the valence mismatch between Ba^{2+} and La^{3+} (electronic compensation). Therefore, the conductivity is drastically increased, the number of charge carriers being equal to the La concentration, i.e, $[La_{Ba}^{\bullet}] = n$. Another reaction can increase the conductivity also by charges releasing. However, this next mechanism does not involve doping to occur (which might also be present):

$$O_o \leftrightarrow \tfrac{1}{2} O_2 + V_O^{\bullet\bullet} + 2e' \quad (2.4)$$

(2.4) indicates a reduction reaction that produces oxygen vacancies and free electrons (electronic compensation). First-principles calculations performed by Erhart *et. al.* [50] have shown that doubly charged oxygen vacancies ($V_O^{\bullet\bullet}$) are accountable for *n*-type conduction under oxygen-poor conditions. We want to point out that (i) the black curve in Fig. 1.2.2 [46] is resulting from such reaction and more important (ii) reducing conditions are also favorable to compensate the donors by electrons. But since the maximum oxygen non-stoichiometry of pure $BaTiO_3$ is only 0.07 at % at 1000°C ($BaTiO_{2.998}$) [51], it is difficult to account for compensation (2.4) at higher donor dopants concentration. Therefore, reaction (2.4) cannot totally cancel reaction (2.1) and (2.2) is expected to occur at higher concentration range, as explained in the next paragraph.

The dependence of room temperature resistivity of donor-doped $BaTiO_3$ as a function of dopant concentration (figure 1.2.4) has been intensively debated [48,49,52]. This behavior is poorly understood, but is usually explained as a change of compensation mode from electronic to ionic depending on the doping concentration as schematized in Fig. 1.2.5. For

small amount of dopants, the releasing of electrons drops the resistance according to Eq. (3). An increase of the charge carrier density can also be obtained under oxygen-poor treatment (reaction (2.4)), but the curves plotted in Fig. 1.2.4 have been obtained under oxidizing conditions. Therefore, only (2.3) can account to explain the resistivity decreasing. At higher concentration, we observe an increase of the resistivity. This is usually explained by an ionic compensation mechanism according the (KV) notations: Eq. (2.1) and/or (2.2). Ionic vacancies ($V_{Ti}^{''''}$ and/or $V_{Ba}^{''}$) might be assumed to be created to counter-balance the extra charges. Thus, one should expect to observe extra-phases at the grain boundaries resulting from the doping incorporation in the network. In the light of these assumptions, we are now going to describe the state of art, often very contradictory. This will be useful in the chapter III referring to the results obtained in our donor doped thin films.

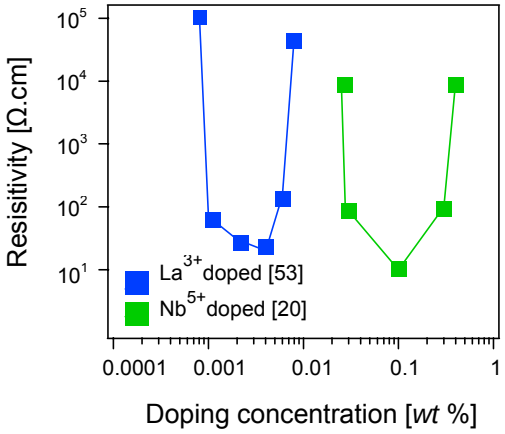

Figure 1.2.4: Resistivity of $BaTiO_3$ ceramics as a function of La / Nb concentration. A resistance minimum is observed with increasing the amount of dopant. Also observed with other dopants as Y, Sm, Gd, Ho, Nd.

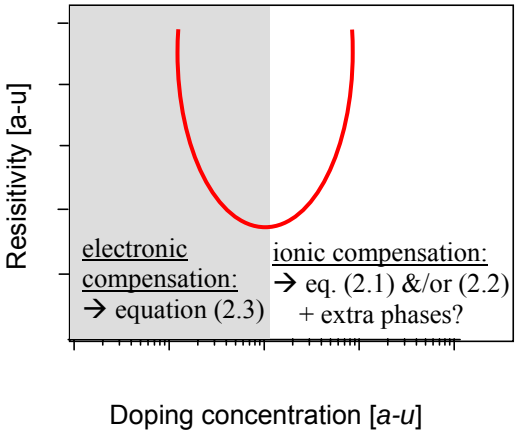

Figure 1.2.5: Schematic diagram showing the change of resistivity vs. doping content and possible mechanism of compensation involve in each region of semiconductivity.

The following paragraph is referring to the region where only ionic compensation is assumed (increase of resistivity). At the very beginning [52,54–57], $V_{Ti}^{''''}$ has generally been considered to be an unlikely defect because of its high effective charge that corresponds to a major disruption of the chemical bonding of the crystal. Thus, early theory [52,54–57] have assumed the formation of $V_{Ba}^{''}$ in the grains and, consequently, the formation of BaO phases at the grain boundaries. Therefore, a separated phase (BaO) is formed to accommodate the

doping incorporation following the reaction (2.2). Another theory, also assuming the presence of V''_{Ba} has been proposed [54] in which the resulting BaO (no specific form has been given) does not represent a separate phase but a structural accommodation in an ordered fashion within the grains. This could happen in the way that $Sr_3Ti_2O_7$ and $Sr_4Ti_3O_{10}$ are formed by ordered layers of SrO between perovskite type $SrTiO_3$ layers of various thickness denoted Ruddlesden Popper (RP) phases [58]. Thus, following these models, the compensation of donor-doped $BaTiO_3$ is by the barium vacancy for high doping concentration. The accommodation of BaO (model I) and RP phases (model II) in the structure are sketched in Fig. 1.2.6.

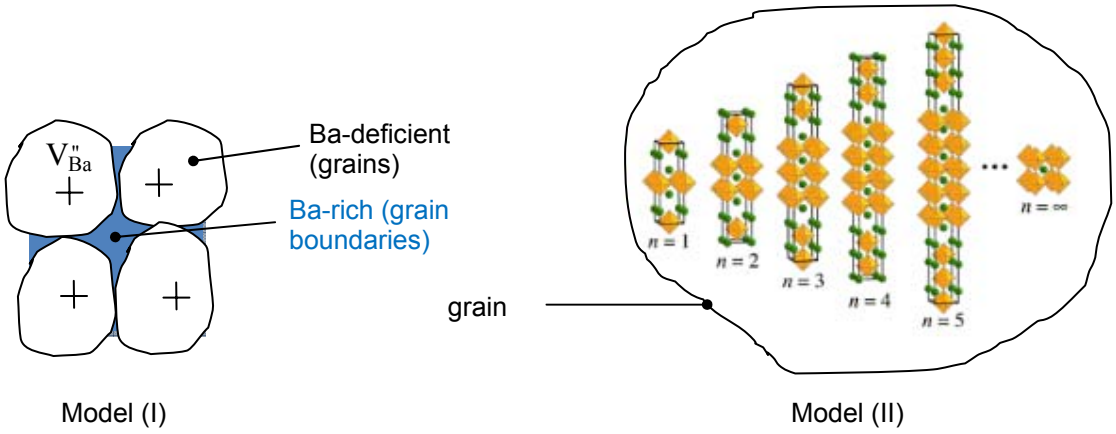

Figure 1.2.6: There are two proposed models to accommodate the barium vacancies: **Left :** (BaO) formation at the grain boundaries (separated phase). **Right:** Ruddlesden Popper phases which are the result of BaO intercalation between the perovskite blocks for different order of intercalation (different n).

However, such RP phases are only speculated since no experimental proof have been given in doped $BaTiO_3$. Furthermore, the solubility and mode of incorporation for BaO in $BaTiO_3$ were studied by X-ray powder diffraction by Hu et. al. [59] using scanning and transmission electron microscopy, electron probe microanalysis, and equilibrium electrical conductivity measurements. The presence of barium orthotitanate, Ba_2TiO_4, as a second phase for samples containing >0.1 mol% excess BaO was confirmed by direct microscopic examination. There was no evidence to support the incorporation of excess BaO into $BaTiO_3$ by a Ruddlesden-Popper (RP) type of superlattice ordering mechanism (Model (II) in Fig. 1.2.6).

If RP phases seem to be very unlikely, the formation of V''_{Ba} accompanied by Ba-rich precipitation were therefore assumed to occur since V''''_{Ti} would be energetically unfavorable.

Contradictory results have been published later [60] with the help of transmission electron microscopy (TEM), which have indicated that the compensating defects in donor-doped $BaTiO_3$ are titanium vacancies ($V_{Ti}^{''''}$). Surprisingly, very small amounts of Ti-rich secondary phases ($Ba_6Ti_{17}O_{40}$) have been observed at the grain boundaries resulting from a Ti expulsion from the grains. This result has been supported later by different authors [see e.g. 61,48].
We are now going to discuss the compensation mode at lower donor concentrations since the electronic compensation mode (reaction (2.3)) is also discussed [46,48,62]. The controversy can be summarized as following:

- Point 1: Donors are charge-compensated by Ti vacancies under all circumstances (reaction (2.1)), i.e. electrons never serve as the major charge-compensating species (reaction (2.3) never occurs). The semiconductivity at low dopant concentrations is only induced by loss of oxygen due to the high temperature firing commonly used in solid state reaction (typically, ~1300°C). In fact, this semiconductive character is only induced by reaction (2.4). In addition, partial reoxidation can occur at grain boundaries during cooling [46,62]. See also figure 1-4 (b).

- Point 2: Electrons are in fact a major charge-compensating defect over a wide range of conditions, and the conductivity is due to an electron concentration that is directly resulting from the donor concentration [49]. Thus, at low donor concentrations, reaction (2.3) is dominant.

Let see how the first point (rejecting reaction (2.3)) has been experimentally suggested.
West *et al.*[62] have prepared La-doped $BaTiO_3$ ceramics at low donor concentrations using a sol-gel route with final firing at 1100°C. According to these authors, this rather low temperature allowed them to avoid the oxygen loss occurring during the high temperature firing commonly employed in solid state chemistry. Fig. 1.2.7 reports the resistivity behavior vs. temperature for both sample preparations (sol-gel and solid-state reaction). Obviously, the resistivity of the samples sintered at low temperature is several orders of magnitude higher than those of the samples prepared at higher temperature. Therefore, compensation only by titanium vacancies is claimed. But, we have to note that the density of this ceramic (prepared by sol-gel) is much lower (~ 75%) than the one prepared by solid-state route (> 95%). Therefore, the porosity might influence the apparent resistivity observed. In addition, the electrical measurements have been performed until 1200°C, which is a higher temperature

than the firing one. In addition, the incorporation of the donors might be different for the different preparation techniques.

Let see now how the second point (assuming reaction (2.3)) has been experimentally determined [49]. The reliability of the measurement is based on the assumption that each added oxygen ion (O^{2-}) will neutralize two La^{3+} dopant ions, e.g. $LaO_{1.5}$ vs. BaO it replaces. Thus, a direct (and proportional) relation between the amount of oxygen and the amount of dopant has been speculated.

In that works, the authors have measured the weight change between the oxidation and the reduced states for a given doping concentration (one sample). They did it for different doping concentrations (different samples) using thermogravimetric measurements under the same conditions for each duplicate samples [54]. The reversible weight change was precisely that expected for weight gain or loss of oxygen that is the charge equivalent to the donor content, as shown in Fig. 1.2.6. The electrons have then become the main charge compensating defect due to the reduction. Thus, the free carrier concentration is directly coupled with the doping content.

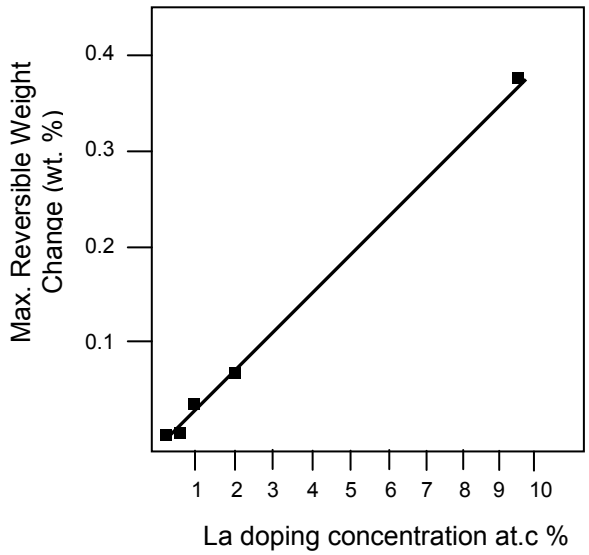

Figure 1.2.6:. The reversible weight change between oxidized and reduced $BaTiO_3$ doped with various concentrations of La^{3+}. The line is the calculated weight change for gain or loss of the "extra" oxygen in the donor oxide. The results suggest that the conductivity arises from an electron concentration that is directly coupled to the donor. Adapted from [54].

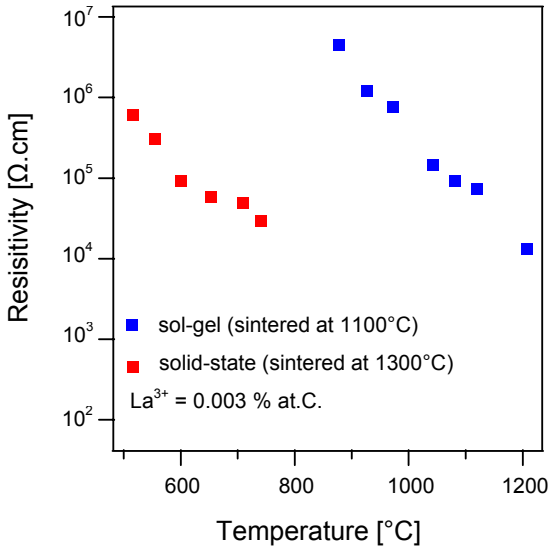

Figure 1.2.7: Resistivity data for sol-gel and solid-state preparation on La-doped $BaTiO_3$ ceramics. The doping content (0.003% at.C.) corresponds to the electronic compensation region. High resistivity is observed for sol-gel sample, suggesting (i) that La must be entirely compensated by titanium vacancies even for low donor concentration, (ii) samples prepared by solid-state reaction are oxygen nonstoichiometry. Adapted from [62]

The discussion about the charge compensation mode in donor doped $BaTiO_3$ is thus very perilous. Concentration of dopants, oxygen partial pressure and temperature used during the firing, must be systematically mentioned for realistic comparison. The Kröger–Vink (KV) notations can be used to express the type of disorder but is not a self consistent notation to understand the entire systems (bulk + grain boundaries). The experimental results discussed above have provided complementary informations to understand the different mechanism:

- At low donor concentrations, the samples are semiconducting. It seems that reaction (2.3) occurs. The couple Ba^{2+}/La^{3+} provides the free electron density proportionally to the doping content until a certain threshold.

- At higher donor concentrations, the resistivity increases due to a decrease of charge carrier concentration. This lowering of charge carrier density is obtained by ionic compensation (most likely $V_{Ti}^{''''}$ (reaction (2.1)) and consequently, Ti-rich phases at the grain boundaries under the following form: $Ba_{1-x}La_xTi_{1-x/4}O_3 + TiO_{secondary\ phase}$. But under oxygen-poor sintering conditions, the threshold between electronic/ionic compensation can occur at higher doping content than for oxidizing conditions [60,63]. This is mainly due to the contribution of reaction (2.3) + reaction (2.4) which provides enough electrons to compensate the donor. But since the maximum oxygen non-stoichiometry is limited to 0.07 at %, for reduced materials, $V_{Ti}^{''''}$ + Ti-rich phases still occur in the higher concentration range [60,61,64].

In summary, the electrical properties of donor-doped $BaTiO_3$ are not entirely understood. By using macroscopical model, we clearly see that interfaces (electrodes, grain boundaries) play a major role in the non-linearity observed. Interface states induce Schottky barriers (and thus high resistivity) under heating. This abrupt jump of resistivity takes place at the Curie temperature demonstrating the coupling between phase transition and PTCR effect. Studies of the chemical and electronic nature of interface states are thus a key to understand the mechanism of compensation. However, such detailed investigations are still missing and this is strong motivation for the present work. Our results will be described in the Chapter III.3.4

since surface and interface spectroscopy have been largely used in this thesis to study $BaTiO_3$ in thin film form (Nb-doped and undoped).

Let us show now another consequence of charged interfaces in perovskites. During the last decade, many materials with so-called "giant" permittivity have been investigated. We will show in this part that free charges may be stored at inner interfaces leading to extrinsic colossal permittivity.

1.2.3 Giant-dielectric phenomenon in $CaCu_3Ti_4O_{12}$ (CCTO)

In 2000, Subramanian *et al* [65] reported a high permittivity of ~12,000 in CCTO ceramics which, when measured at 1 kHz, remained constant between 100K and room temperature. The authors also reported a drastic decrease in the room temperature permittivity with increasing measuring frequency or decreasing temperature. These results are reported below, Fig. 1.2.8 under iso-frequency profiles.

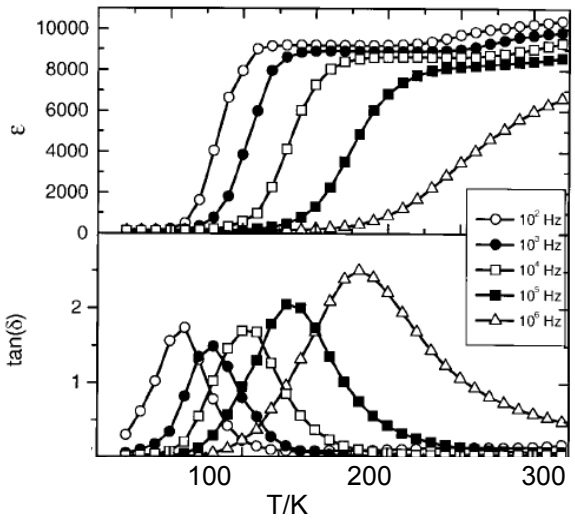

Figure 1.2.8. Iso-frequency dependence of the real part of the dielectric response of CCTO. The loss factor is also reported. Colossal permittivity is clearly measured with large loss (>1). Reported by [64].

Since the original report by Subramanian *et al*., there has been substantial debate about the origin of this very large permittivity (180 papers in 7 years). In the early stages, few intrinsic mechanisms were proposed [see e.g. 66] in which a dipolar mechanism was assumed (Ti^{4+} displacement in the oxygen octahedral). This intrinsic model was finally ruled out shortly after, especially thanks to the investigations of Sinclair *et al,* [67]. In this work, impedance spectroscopy was used to reveal a succession of two semicircles. Such behaviour is often found in ceramic materials, whose dielectric response at low frequencies is dominated by grain boundaries (e.g. Fe-doped $BaTiO_3$). These results are explained with an "internal barrier layer capacitor" (IBLC) model: semiconducting grains + insulating grain boundaries (similar to the model presented on 1.2.3 (b)) leading to Schottky barrier formation at these interfaces. Impedance plots (–Z'' vs. +Z') are appropriate (see fig. 1.2.9) to distinguish both contributions (grain / grain boundaries). The dispersion of the giant permittivity has been also reported (Fig. 1.2.10) at the same temperature evidencing a clear Debye-like behaviour. Furthermore, the imaginary part (ε''_r) increase strongly at low frequency denoting a Maxwell-Wagner effect. However, it should be noted that electrical measurements does not allow identification of the physical origin of the observed semicircles. The first semicircle could be due to grain boundaries, twinning boundaries (domain walls), and interfaces with electrodes. Although the extrinsic mechanism seems to be well accepted, the question related to the physical origin of this interfacial polarisation is not fully established. Up to now, it is not possible to definitely conclude which of the above developed scenarios is correct. Like the PTCR effect, models are limited by the unsatisfactory knowledge of charged defects at interfaces.

Finally, we just saw through the CCTO system that interfaces (grain boundaries, domain walls or electrodes) play again a major role in the dielectric properties. If the applications of CCTO in modern electronics seem to be limited (large loss and weak permittivity at frequency beyond megahertz), this material represents at least an educational system to see the consequences of such depleted interfaces on the dielectric properties of oxides. Improving the control of interfaces in advanced ceramics could considerably help for applications in integrated devices.

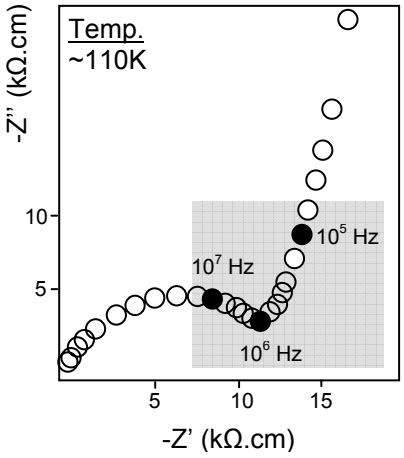

Figure 1.2.9: Impedance complex plot at 110K for CCTO materials. The inset square denotes the switching between bulk and conductivity contributions. After [67].

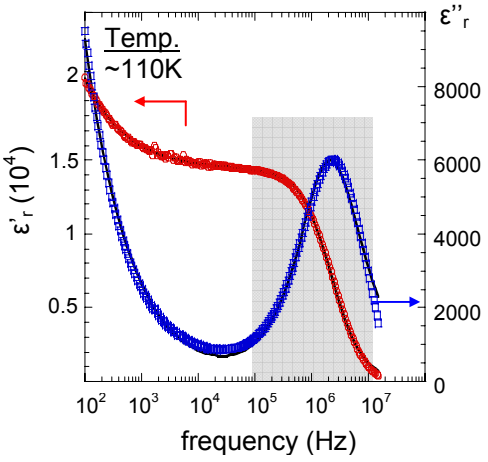

Figure 1.2.10: Isothermal dispersion of the dielectric permittivity at 100K for CCTO. The inset square denotes the dielectric relaxation. After [68]

The first two paragraphs (PTCR and CCTO related) were mainly focused on surface and interface defects inducing colossal change in electrical properties. In the next paragraph, we are going to "highlight" the importance of oxidation and reduction of $BaTiO_3$ in the near surface region.

1.2.4 Stoichiometry change in the near-surface region

The surfaces of ABO_3 perovskites have been intensively studied, especially for bulk materials at elevated temperature [69-71]. Indeed, the equilibrium conductivity study of such oxides is generally performed between 750 and 1200°C under a broad range of oxygen activity. Therefore, in order to reach the thermal equilibrium and solid/gas equilibria, long dwell times are requested (up to several hours). This protocol must be repeated for each partial pressure under variable temperature making the experiment particularly long (typically, several days of continuous heating are necessary).

Consequently, the materials gain or loose oxygen as it is expected but the cationic distribution (A and B site) can also be drastically modified between bulk and surface, modifying thus the original surface stoichiometry. This will be the topic of this paragraph.

In the last few years, it has been recognised that chemical reconstruction in the near surface region can occur under extensive thermal treatment. Cation segregation and solid state reactions cause a chemical heterogeneity in the surface layer with the formation of so-called A-cation rich Ruddlesden-Popper ($AO(ABO_3)_n$) and B-cation rich Magneli type (B_nO_{2n-1}) phases [72-73] depending on the thermal treatment. The situation can be summarized Fig. 1.2.11.

Figure 1.2.11: Schematic illustration of the chemical heterogeneity in the surface region of a ABO_3 crystal induced by oxidation or reduction thermal treatment at elevated temperature.

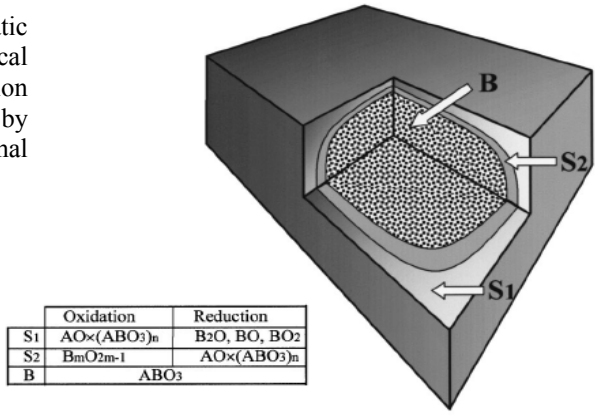

	Oxidation	Reduction
S1	$AO\times(ABO_3)_n$	B_2O, BO, BO_2
S2	B_mO_{2m-1}	$AO\times(ABO_3)_n$
B	ABO_3	

$SrTiO_3$ has been particularly studied since it does not exhibit a ferroelectric domain structure which influences the surface topography; it is paraelectric and crystallises in simple cubic structure for a wide range of temperature. We are thus giving several examples using the $SrTiO_3$ system as reference for discussion.

a) Surface reactions in oxidizing atmosphere

Heating $SrTiO_3$ in oxidizing atmosphere increases $\left[V_{Sr}^{''}\right]$ at the $SrTiO_3$ surface according to the defect reaction of the cation sub-lattice:

$$Sr_{Sr}^{x} + 2e' + \tfrac{1}{2} O_2 \leftrightarrow V_{Sr}^{''} + SrO_{secondary\text{-}phase} \qquad (2.5)$$

Sr ions will diffuse outwards from the bulk to the surface, where they can react with gaseous oxygen and form SrO-rich surface phases. Szot *et al.* [69] have observed a continuous accumulation of SrO_x on $SrTiO_3(100)$ surfaces in the case of oxidizing conditions. Sr surface

segregation and growth of SrO_x secondary phase on $SrTiO_3$ surfaces under oxidizing conditions have been also confirmed by many groups [74-76]. The amount of the formed surface SrO_x layers increases with the doping level of heterovalent dopant (La^{3+} or Nb^{5+} …) since the extrinsic donor dopants could create more Sr vacancies and enhance Sr diffusion in the solid [75] following equation (3).

Finally, Rahmati *et al.* [76] also shown that the density of surface SrO-rich islands depends on $SrTiO_3$ surface orientations. The island density decreases in the sequence of (100), (110) and (111). The main results are presented in Fig 1.2.12.

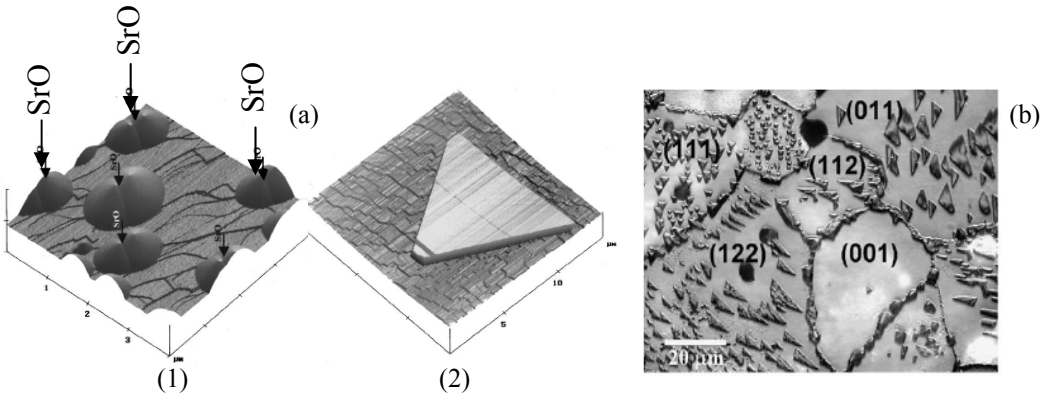

Figure 1.2.12: (a) AFM measurements of (100) surfaces prepared at 1000°C for (1) 24h and (2) 120h. The data give evidence of microcrystal which are attributed to SrO phase. It seems that regular microcrystal is formed due to the agglomeration of dropetlike features [68]. (c) optical micrographs from polycristalline STO with different orientation of the grains [75].

The formation of $[V_{Sr}^{''}]$ has been suggested to be accompanied by growth of Ruddlesden-Popper (RP) phases: ($AO(ABO_3)_n$) in the subsurface region which act as a source for the excess of Sr in the surface region [69]. Meyer *et. al.*, [77] have shown that under static electric field, reversible structural changes occurs in the near surface region of $SrTiO_3$ single crystals. Formation of Ruddlesden-Popper phases of composition $SrO(SrTiO_3)_n$ were evidenced using Wide-Angle X-ray Scattering (WAXS). The RP phases order (n) has been tuned under different voltages after relaxation time of about 250 min at every level of electric field at room temperature.

b) Surface reactions in reducing atmosphere

In reducing conditions, oxygen may desorb from the surface:

$$O_O^x \leftrightarrow V_O^{\bullet\bullet} + 2e'' + \tfrac{1}{2} O_2 \qquad (2.6)$$

The reduction leads to an increase of $[V_O^{\bullet\bullet}]$ at the surface. Thus, the concentration of compensating $[V_{Sr}^{''}]$ subsequently increases resulting in Sr migration from the surface to the bulk. Consequently, Ti enrichment can be assumed (and Sr-deficiency) on the surface. It has been demonstrated that reducing $SrTiO_3$ surfaces in vacuum above 900°C causes formation of Ti-rich surface phases, including Ti-rich phases of TiO and Ti_2O [69], TiO_2 [72], Ti_2O_3 islands [78].

1.2.5 Closing Remarks

Up to now, only bulk materials have been considered. Doping and grain boundary effects on electrical properties were presented through both PTCR and colossal permittivity materials. The role of interfaces has been emphasized in term of charged defects influencing the electrical properties. Stoichiometry change under thermal treatment was also described showing again the importance of surfaces in ABO_3 compounds. For a given composition, the situation in thin film materials is different. For instance, (i) the phase transition paraelectric/ferroelectric is very difficult to observe with a classical impedance spectroscopy approach (ii) the doping effect does not seem to change so drastically the electrical properties and (iii) the consequences of large thermal treatment on surface stoichiometry, have not been really studied in thin film materials. In the next paragraph, we are going to describe (i) the major extrinsic effects encountered in thin films (e.g. strain, size, interface…) and (ii) discuss the preliminary results about surface and interface studies of $ATiO_3$ thin films which have been the starting point for our investigations.

1.3 Ferroelectricity in thin film materials

A basic characteristic of all ferroelectric materials is the hysteretic behaviour relating polarization P and applied field E_a. If we apply a large E_a to the specimen, numerous domains can be lined up in the same direction. For instance, in memory applications, we can switch the polarization of the entire crystal from up (+1) to down (0) by reversing E_a. In a large single crystal this would require voltages of several kilovolts, which would be impractical for a commercial device. For a thin film of 100 nm thickness, it requires only a few volts. Thus the development of practical ferroelectric devices is closely linked with progress in thin films technology.

However, thin film processing is not always straightforward. With the available deposition techniques, ferroelectric memories are already suitable but the reliability remains a key issue. For instance, one of the most common approaches to measure the transition temperature of a ferroelectric material is to measure the dielectric constant and loss. However, in thin films, there are significant complications probably due to surface/interface effects (see Fig. 1.3.1). This paragraph will describe the main differences encountered in thin films compared to bulk ceramics or single crystals; Size effects (e.g. thickness dependence) and interface effects (e.g. metal-ferroelectric junction) will be described. The second part of this paragraph will deal with the electrical properties of $BaTiO_3$ thin films deposited on different bottom electrodes. Some recent investigations will also be described as they open a new field of study in ferroelectric thin films.

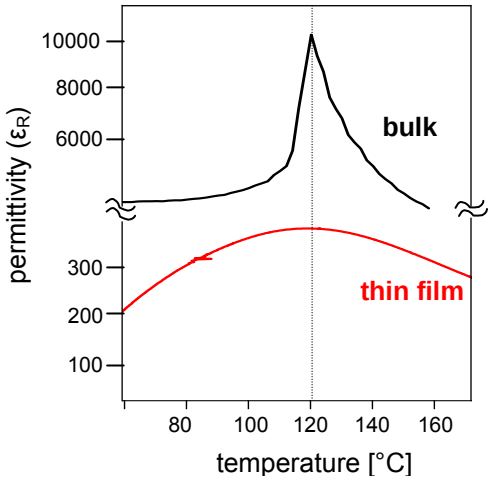

Figure 1.3.1: $BaTiO_3$: relative permittivity profile as a function of the temperature for bulk and thin film materials. Strong lowering of ε' and subsequent profile broadening are typically observed in thin films.

1.3.1 Grain size effects

It is first important to notice that thin films may differ in some substantial ways from bulk ceramics or single crystals of the same composition. The grain size is one of the effects involved in this difference. The purpose of this paragraph is thus to describe the consequences of grain size reduction to macroscopic properties.

In bulk $BaTiO_3$ ceramics, the grain size has a strong effect on the low frequency permittivity as shown in Figure 1.3.2. The permittivity is rising with decreasing grain sizes below approx. 10μm [79]. It is also clear from the graph (a) that grain size has no observable effect on the ferroelectric transition temperature. The higher permittivity for smaller grain size may be due to mechanical compression, inducing a preferred domain orientation. Thus, the subsequent stress can increase the polarizability in a preferred direction (single crystal-like). On the other hand, when the grain size increases, the stress is relaxed by the large size (polycrystalline-like), leading to a drop of the apparent permittivity. Grain boundary effects are also often invoked to explain the drop of permittivity [80,81]. However, the paraelectric state above the Curie temperature should also be affected by a low permittivity interfacial layer, which is not observed.

$BaTiO_3$ thin films show typically much lower permittivities than ceramics. But a significant increase of room temperature permittivity with a change from granular to columnar grain morphology is commonly observed, as show in (b) and (c). In contrast to $BaTiO_3$ bulk ceramics, which exhibit a clear paraelectric / ferroelectric phase transition, only a broad maximum in the permittivity vs. temperature curve is observed for polycrystalline thin films with a strong decrease of the maximum temperature (100K instead of 400K) . A diffuse phase transition (DPT) is commonly used to describe this phenomenon. In addition, the $BaTiO_3$ thin films do not show a ferroelectric hysteresis at room temperature suggesting that thin films of BTO behave as a superparaelectric material (since 1997 however, several publications are reporting ferroelectric hysteresis at room temperature for fully epitaxial BTO thin films. This will be described in the next paragraph).

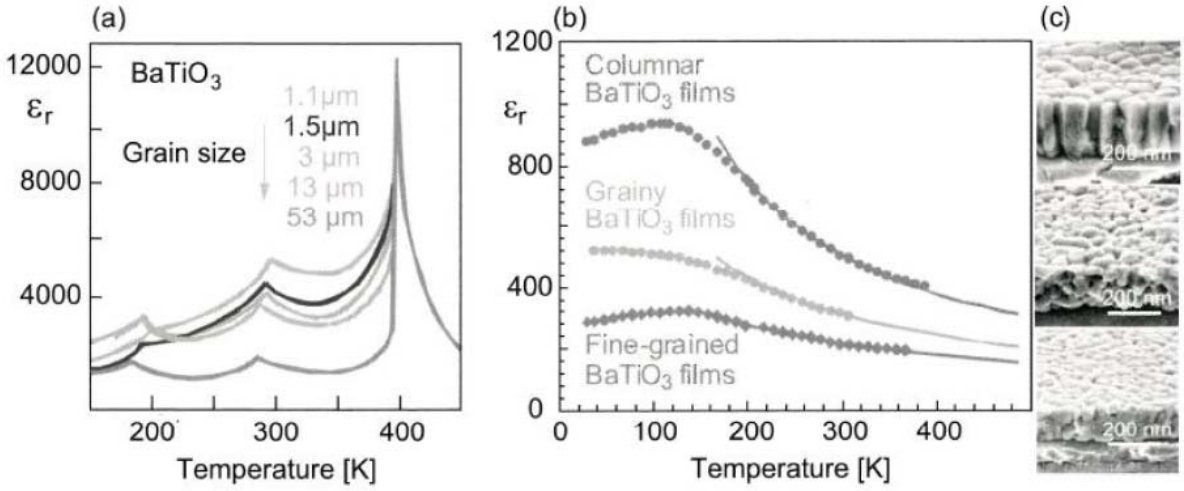

Figure 1.3.2: Temperature dependence of the permittivity for (a) bulk ceramics with different grain size after [79] and (b) thin films with different grain sizes. (c) show the microstructure of the corresponding films after [1].

1.3.2 Interface effects

Because capacitors are often the largest components in electronic circuits, extensive efforts are directed at reducing their size through the use of high-permittivity (i.e. high-storage ability) insulators such as perovskites, which should provide more capacitance per unit area. Unfortunately, most of the experiments on thin-film capacitors (e.g. $SrTiO_3$, $BaTiO_3$, $(Ba,Sr)TiO_3$) have yielded capacitance values that are orders of magnitude smaller than expected [82]. The microscopic origin of this reduced capacitance, which is often discussed in terms of a low-permittivity interfacial "dead layer", is not well understood. Experimentally, the thickness of the "dead layers" seems to be about 5-10 nm or more [83-87], whereas first principles calculations give a much smaller value of about 1nm [88-90]. In some works a tetragonal interface layer is found at all temperatures, even above T_c [60,61], where in others it is cubic even below T_c [83,84]. In fact, the structure of the surface layer can be rather complex and depends on processing conditions [91]. Whether such a dead layer exists at all, and if so, whether it is an intrinsic property of an ideal metal-insulator interface or a result of processing, which introduces defects and strain, are controversial questions [92]. This paragraph will describe the main experimental results available in the literature referring to the "dead layer" effect. Then, we will focus our discussion on bottom electrode / thin-film interfaces, which are much more influent than the top electrode.

The experimentally observed reduction in effective permittivity is usually expressed in terms of regions of low interfacial capacitance C_i, at the electrode-ferroelectric interfaces, acting in series with the nominal (bulk) ABO_3 capacitance C_b, to give a lower overall capacitance C_0:

$$\frac{1}{C_0} = \frac{1}{C_i} + \frac{1}{C_b} + \frac{1}{C_i} \qquad (1.3.1)$$

Figure 1.3.3 shows the inverse of the apparent capacitance at zero bias as a function of film thickness, at temperatures of 25, 100, 150, and 200°C. Results for a sample thickness of 12nm are included [93].

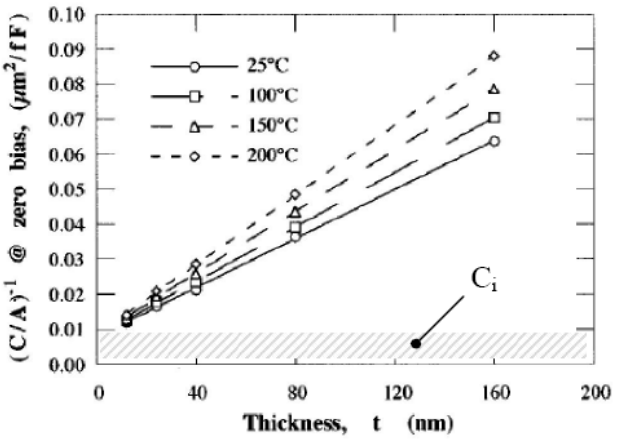

Figure 1.3.3: Thickness dependence of inverse capacitance divided by area at different temperatures (MOCVD-Pt/BST/Pt). An interfacial layer temperature and thickness-independent is observable [93].

The intercepts of the various curves are approximately independent of measurement temperature, while the slopes vary quite strongly. In this model, the permittivity of the dead layer is thus assumed to be temperature and field independent (consistent with the term "dead layer").

At present, two competing models for the interfacial layer exist. The first one is based on the finite electrostatic screening length in the metal supporting the idea of an intrinsic dead layer [94]. However recent experiments have shown that, by using free-standing single-crystal lamella instead of standard epitaxially grown films, bulk-like behaviour can be obtained even for lamellae as thin as 75 nm [95] as shown in Fig. 1.3.4. These results suggest that dead layers in thin films could arise from growth-induced defects, strains and grain boundaries rather than from the intrinsic properties of the interface. Several groups have shown that truly epitaxial growth can indeed significantly sharpen the form of the peak in dielectric constant against temperature, and raise the peak dielectric constant closer to single crystal values than

has previously been thought possible [96,97]. Results for different deposition conditions are given in Fig. 1.3.5.

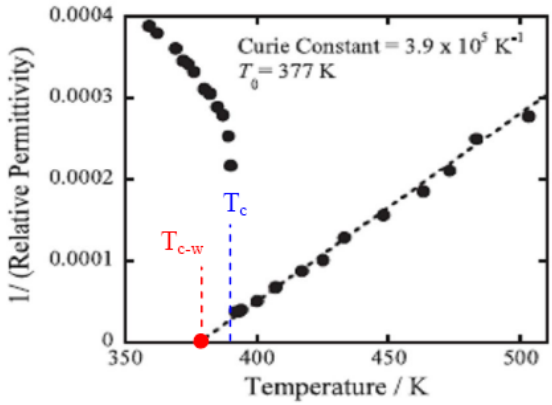

Figure 1.3.4: $BaTiO_3$: Above the observed Curie anomaly, the dielectric response of thin lamellae (75nm) exhibit Curie-Weiss response, with T_{c-w} below T_c. After [95]. Electrodes: Au.

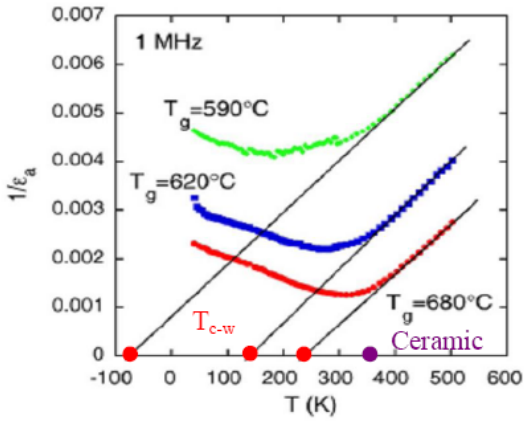

Figure 1.3.5: Inverse of the permittivity as a function of temperature, measured at zero bias and 1 MHz frequency for thin films grown at different temperatures (T_g) , after [97]. System: Pt/BTO/Pt.

It can be seen from figure 1.3.5 that all the films show Curie-Weiss behaviour above 400 K (growth temperature: T_g). But the apparent Curie-Weiss temperature is considerably affected by the growth temperature of the film. Usually, it seems to be difficult to obtain T_{c-w} **film** ≈ T_{c-w} **ceramic**, for a given composition. This change of T_{c-w} without a change of the slope (Curie-Weiss constant) was ascribed to the columnar nature of such films.

To complicate things further, the effect of the electrode material is even less clear [98]. For instance, Scott *et al.* [99] have pointed out the substantially better electronic screening provided by elemental metals, resulting in dead layer-free capacitors. However some works [96] suggested that the high ionic contribution to short range polarizability provided by electrodes such as $SrRuO_3$ or $LaNiO_3$ should yield improved screening; several experiments on thin $(Ba,Sr)TiO_3$ or $BaTiO_3$ films seem to support this argument [96,100-104].

Recently, fully *ab initio* calculations of the dielectric properties of $SrRuO_3/SrTiO_3/SrRuO_3$ and $Pt/SrTiO_3/Pt$ nanocapacitors have been performed by Spaldin *et al.* [92]. They found that the dead layer effect is reduced by almost a factor of four for electrodes made of elemental metals (e.g. Pt) as electrodes. These results suggest that electrodes with shorter electronic screening length, such as Pt or Au, should be the best candidates for reducing the dead layer. But again, these calculations report an opposite trend to many experimental groups, since the

superior perovskite-perovskite epitaxial quality brings the measured interfacial capacitance close to negligible values. In summary, the macroscopic origin of the reduced capacitance layer is not well understood. At least since ferroelectric materials are good insulators, the majority of carriers are injected from the electrode and therefore, the metal/film contact formation is a crucial point and might influence the macroscopic properties.
In Si-based technology, the metal contact on heavily doped-Si (most of the devices) forms an Ohmic contact as it is required for every semiconductor device in order to drive current in and out of the device. On the contrary, for the usual applications of ferroelectrics (capacitors) it is desirable to have the largest barrier possible to avoid residual leakage currents (see below).

Schottky barrier formation at metal-ferroelectric junctions

In the following, the ferroelectric film will be considered as a large band gap semi-conductor. The barrier heights of metal-semiconductor or metal-insulator systems are, in general, determined by both the metal work function and interface states [5]. In a simple model (in which interface states are not taken into account), the metal work function W_f drives the metal-ferroelectric junction properties. If the metal work function is greater than the electron affinity χ of the ferroelectric, a potential barrier Φ_b (for electrons) is formed at the interface. On the other hand, if the electron affinity of the ferroelectric is greater than the metal work function, an Ohmic contact should be formed (Φ_b = 0 eV). In this model, the barrier height is simply:

$$\Phi_b = W_f - \chi \qquad (1.3.2)$$

The situation is summarized Fig 1.3.6, where interface states are neglected and the ferroelectric (semiconductor) is assumed to be n-type doped. The latter assumption will be shown to be reasonable for $BaTiO_3$. Work functions of some typical electrode materials are given Table 1.

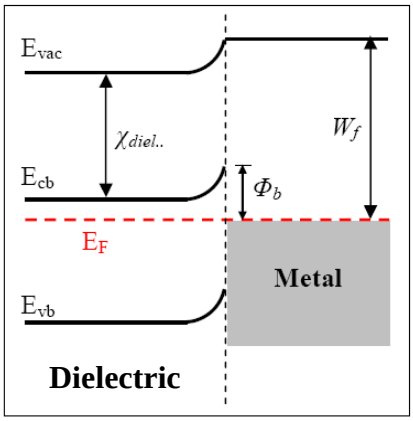

Figure 1.3.6: Energy-band diagram for typical rectifying (non-ohmic) contact between dielectric and metal. Interface states have been neglected in this schematic layout. E_{vac} indicate the vacuum level. Others notations are indicated previously in the text.

Electrode material	Work function (W_f)
Pt [5]	5.6 eV
Au [5]	5.1 eV
RuO_2 [105]	6.1 eV

Table 1: Work function of selected candidate materials used as electrode.

The bottom electrode for ferroelectric films has to fulfil several conditions. It must remain conductive even after the thin film deposition and must not react with the film. It should also have a sufficiently high work function to limit the leakage current as discussed previously. Noble metals such as Pt are the most suitable candidates from the point of view of chemical inertness and high work function. However, the available Pt substrates are most often [111] textured (polycrystalline). Therefore, with such platinized wafers, it becomes difficult to grow fully epitaxial films. As the electrical properties are strongly improved for high epitaxial quality films, this is a considerable limitation. However, some authors are able to grow very nice epitaxial films onto epitaxial Pt [97]. But this requires an individual Pt deposition prior to the ferroelectric film deposition. This might not be reasonable for industrial applications. As alternative bottom electrodes, conducting oxides such as RuO_2, IrO_2, $SrRuO_3$, Nb-doped $SrTiO_3$ might be suitable.

Until now, interface states have been neglected in the metal-ferroelectric junction. The band bending regime occurring in the dielectric (see figure 1.3.6) was so far only the consequence of charge transfer between the dielectric and the metal to equilibrate the Fermi energy. Usually, we define this model as the **Schottky limit** (Ideal Schottky barrier) practically involved in most of ionic semiconductors such as ZnS and Al_2O_3. However, it has been known for a long time, see e.g. [106,107], that for elemental (Si, Ge) and III-V compound semiconductors (e.g. GaAs), the Schottky-barrier formation is essentially independent of metal work function (see figure 1.3.7) but rather pinned by electronic states in the forbidden

gap. These electronic states can be either intrinsic to the metal-semiconductor junction (metal-induced-gap-states [108,109,110]) or extrinsic (defects introduced at the semiconductor surface due to the metal deposition [111]), both are discussed below.

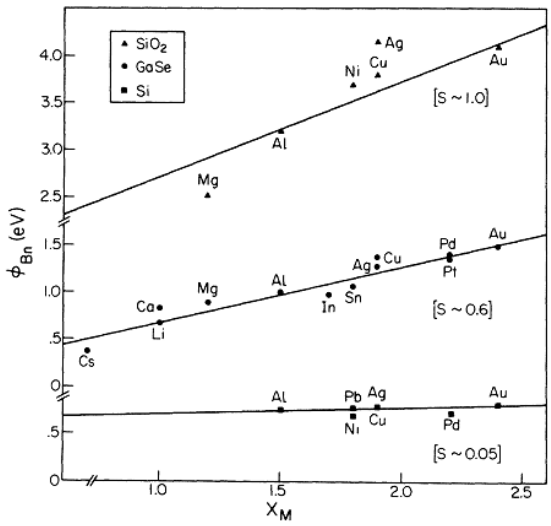

Figure 1.3.7: Schottky barrier energies of various metals on *n*-type semiconductors plotted versus electronegativity (χ_m) of the metal. For each material, slope S of the reference line is inversely proportional to the extent of Fermi-level stabilization at the semiconductor/metal interface [107].

The role of interface states is outlined in Fig. 1.3.8. The left graph shows a situation of an n-type semiconductor with surface states. The surface states are associated with charge neutrality level. The significance of the charge neutrality level is that if the Fermi energy level at the surface or interface coincides with the charge neutrality level, the net charge in the surface/interface states is zero. If the Fermi level is above E_{cnl}, the surface/interface charge is negative (acceptor like) and if E_F is below E_{cnl} it is positive (donor like). To establish overall charge neutrality, the n-type semiconductor develops an upward band bending, which is associated with a positive space charge, which balances the negative surface charge. The situation is slightly more complex at an interface, because a charge in the metal has to be added to the space charge and to the charge in the interface states to obtain overall charge neutrality.

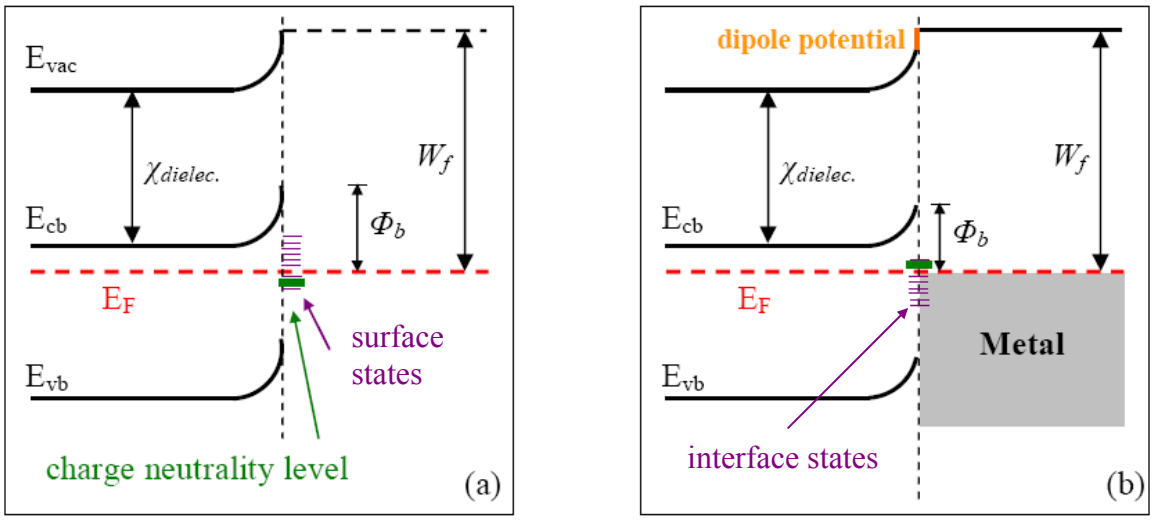

Figure 1.3.8: Energy-band diagram for typical semiconductor (or dielectric) with surface states. (a) without metal junction and (b) with metal junction. The interfaces states lead to a lowering of the Schottky barrier due to charge transfer between these states and the metal inducing interfacial dipole on the vacuum level.

The model describing intrinsic interface states in the band gap of the semiconductor has been first introduced by Heine in 1965 [108]. Louie *et al.* have later demonstrated *metal-induced gap states* using density functional theory [110]. As an example, Figure 1.3.9 shows the local density of states for the Metal/GaAs system, displayed for four regions. Each region contains one atomic layer. The interface is indicated by the red dashed lines (boundary between C and B). The pseudopodential method reveals metal-induced states in the GaAs band gap for the first atomic layer.

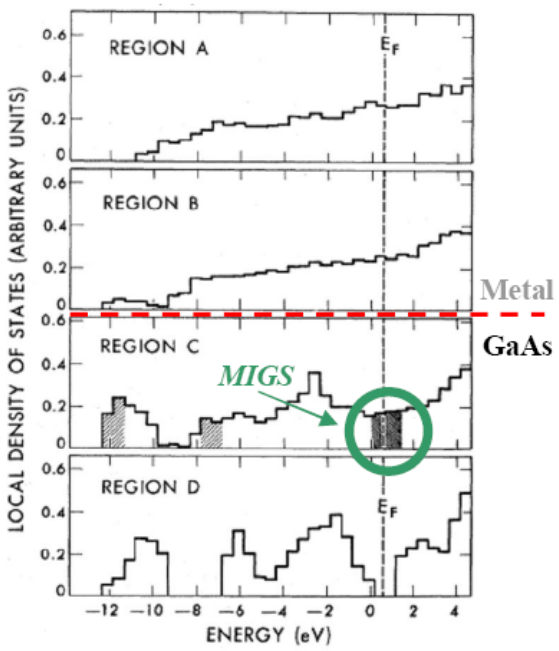

Figure 1.3.9: Local density of states for the Metal/GaAs interface. The red dashed line indicates the junction and MIGS are evidenced in the GaAs forbidden gap with the green circle. After [110].

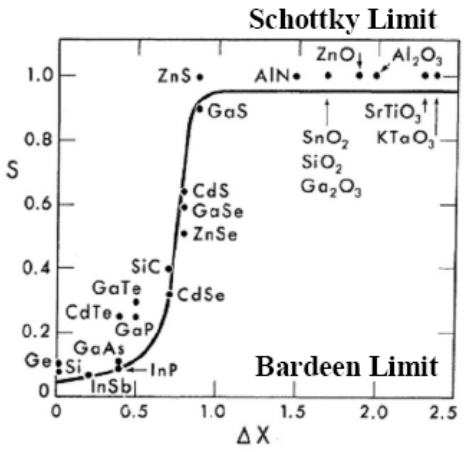

Figure 1.3.10: Index of interface behaviour **S** from Kurtin *et. al.* [107]

The charge neutrality level (E_{cnl}) is directly related to the MIGS and intimately connected to the electronic band structure of the semiconductor. It can be considered as a fundamental material parameter in the Schottky barrier determination. Calculations of charge neutrality levels using branch point energies have been provided by Tersoff [112] and Mönch [113] and by Cardona and Christensen using dielectric midgap energies [114]. The importance of charge neutrality levels for the barrier formation of ferroelectric materials has been pointed out by Dawber and Scott [99].

The limit of very high concentration of surface/interface states, which corresponds to full Fermi level pinning where the surface/interface Fermi level position and the thus also the barrier height are determined by the energetic position of the charge neutrality level, has been evidenced by Bardeen in 1947 [106] and is often termed as the **Bardeen limit.** In most cases, the density of interface states is moderate and the barrier heights will be established somewhere between the Schottky and the Bardeen limit. To express this mathematically, an index of interface behaviour **S** is used, with **S** = 1 corresponding to the **Schottky limit** and **S** = 0 to the **Bardeen limit**. The index of interface behaviour S corresponds to the slope

$d\Phi_b/dW_f$ in Fig. 1.3.7. This slope depends on the ionicity of the semiconductor as pointed out above and displayed in Figure 1.3.10. On this empirical curve, two trends can be observed: (i) **S** is expected to be close to the unity for ionic semiconductor (ii) and small (~0.1) for covalent semiconductors as Si and GaAs [107].

The model of Cowley and Sze [115] is a phenomenological approach to calculate the dependence of the Schottky barrier height (Φ_b) in dependence on metal work function and density of interface states. In this model, the barrier height is given by the following equation:

$$\Phi_b = [\, \mathbf{S}\,(W_f - \chi) + (1-\mathbf{S})(E_g - \Phi_0) - \Delta\Phi\,] + \left\{ \frac{C\mathbf{S}^2}{2} - \mathbf{S}^{3/2} \cdot \right.$$
$$\left. [\; C(\Phi_m - \chi) + (1-\mathbf{S}).(E_g - \Phi_0).\frac{C}{\mathbf{S}} - \frac{C}{\mathbf{S}}\;(\xi - k_b T) + \frac{\mathbf{S}C^2}{4}\;\;]^{1/2} \right\} \qquad (1.3.3)$$

where W_f is the metal work function, χ is the semiconductor electron affinity, $\Delta\Phi$ is the image force Schottky barrier lowering which depends on the magnitude of the electric field, and $\xi = E_{cb} - E_f$ is the Fermi level position in the bulk of the dielectric. We have to note that when **S**=1 (ionic semiconductor), the Schottky barrier calculation is expected to mainly dependent of metal work function. The two parameters **S** and C are given by:

$$\mathbf{S} = \frac{\varepsilon_i}{\varepsilon_i + q d_i N_i} \;\;,\;\; C = \frac{2q\varepsilon_s N_d d_i^2}{\varepsilon_i^2}.$$

where ε_i and ε_s are the interface and bulk dielectric permittivity, d_i is the thickness of the interface layer separating the interface states of the semiconductor from the surface charge of the metal, N_d is the bulk doping density, and N_i is the density of the semiconductor gap states.

Using this model, we can plot the dependence of Schottky barrier height on (i) the doping level N_d and (ii) the interface states N_i in $SrTiO_3$ with Pt electrodes (figure 1.3.11) [116]. Schottky barrier formation on $SrTiO_3$ has been intensively studied [116,117,118] as it is a model ionic compound with high permittivity, easily available in single crystal form, it can be doped, e.g. using Nb, to obtain conducting samples and it is not ferroelectric.

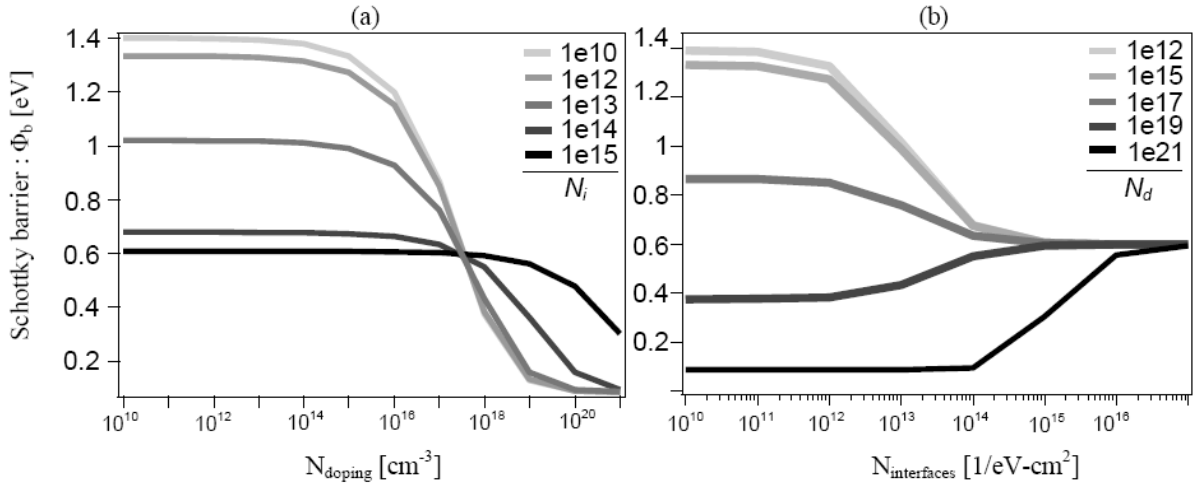

Figure 1.3.11: Schottky barrier heights in dependence (a) on the doping level N_d or (b) on surface densities of interface states N_i. Both N_d and N_i are successively used as a parameter. (a) and (b) are plotted for the $SrTiO_3$/Pt interface [116]. For the Pt work function and the $SrTiO_3$ electron affinity, we have used the values of Φ_m=5.6 eV and χ=4.2 eV, respectively.

Following Figure 1.3.11, a variation of the Schottky barrier can occur by changing the doping concentration or the density of interface states. From (a), it is clear that for low doping concentrations, the interface states are expected to play a major role in the barrier height whereas figure (b) shows that for low interface states densities, N_d will strongly modify the Schottky barrier height.

These graphs are very useful to identify the origin of Schottky barrier height variation, which can occur after a change in defect concentration (N_i) or change in doping concentration (N_d). Schafranek *et al.* [116] have shown on $SrTiO_3$:Nb single crystals with Pt contact a dependence of the Schottky barrier height for different thermal treatments (oxidation/reduction). Photoelectron spectroscopy has revealed a change in defect concentration (oxygen vacancies and Ti^{3+} states) responsible for the barrier height change from 0.5 eV under reduction treatment to >1.2 eV after oxidation.

1.3.3 Electrical properties of $BaTiO_3$ thin films vs. bottom electrodes

Heteroepitaxial $BaTiO_3$ thin films grown on conducting Nb-doped $SrTiO_3$, $SrRuO_3$ and Pt substrates have been intensively studied to measure their electrical properties. Polarization vs.

voltage hysteresis loops were measured with three different substrates combinations by Abe *et al.* [119] as shown Fig. 1.3.12 for $BaTiO_3$ thin films.

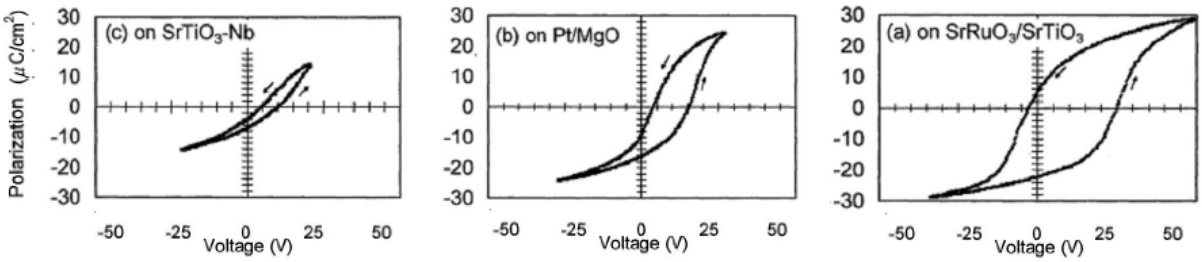

Figure 1.3.12: [119] : Ferroelectric hysteresis loops measured for heteroepitaxial $BaTiO_3$ films grown on (a) $SrRuO_3/SrTiO_3$, (b) Pt/MgO and (c) Nb-doped $SrTiO_3$. BTO thickness 410nm. Top electrode: Pt

Typical ferroelectric hysteresis loops are clearly observable on (a) $SrTiO_3/SrRuO_3$ and (b) MgO/Pt substrates. However, when $BaTiO_3$ is deposited onto (c) $SrTiO_3$:Nb substrates, only a residual loop is observed (Diode-like behaviour). This trend has been confirmed by many groups [120,121,122]. The drastic change in the ferroelectric properties might be explained by the properties of the $SrTiO_3$:Nb/$BaTiO_3$ interface. We will provide evidence that the interface will indeed allow for a large electron injection current (low Schottky barrier), making difficult the polarisation measurements (see the Chapter II.3.1.3).

1.3.4 New trends

Ferroelectric thin films and superlattices are currently the subject of intensive research [123,124,125] partly because of the changes in the ferroelectric properties as the thickness of the ferroelectric materials is reduced. In superlattices composed of layers of $PbTiO_3$ and layers of $SrTiO_3$, Dawber *et al.* have shown an anomalous increase of the tetragonality with the lowest $PbTiO_3$ volume fraction as shown in Figure 1.3.13. They attribute this behaviour to a new phenomenon: an interfacially induced form of improper ferroelectricity. It is related to rotation of oxygen octahedra, which is conversely responsible for a non-polar antiferrodistortive (AFD) ground state (see figure 1.3.14). But this model, do not take into account the possible contribution of interface field resulting from charged defects. It has been shown long time ago[126] that the application of a static electric field (E) results in a

temperature shift of the maximum of permittivity ($T(\varepsilon_{max}) < 10$ K for E = 0 kV/cm and $T(\varepsilon_{max})$ = 40 K for E = 5.18 kV/cm). This was explained in terms of electric field induced ferroelectricity which can occur in ultrathin films. Such an electric field effect was successfully demonstrated very recently [127] with the help of x-ray absorption near edge structure (XANES) analysis. The experiment has revealed a clear shift of the Ti-*K* absorption edge energy under electric field, attributed to a change of the Ti valence state. Therefore, application of a static electric field to a STO crystal results in a redistribution of oxygen vacancies in the near surface region resulting in Ti^{3+} states [127].

If we transfer these considerations to the superlattice structures (Figs. 1.3.13 and 1.3.14), we cannot exclude the following possibility: during vacuum deposition, some charged defects might occur at each interface of the multilayer (likely oxygen vacancies). For the very low coverage of PTO volume fraction (where AFD behaviour was reported), the charged defect at the interfaces could induce an electric field high enough to modify the polarization of the $SrTiO_3$ layer. We have to note that the typical concentrations of oxygen vacancies in ferroelectric thin films is about 10^{17} cm^{-3} – 10^{21} cm^{-3} [128].

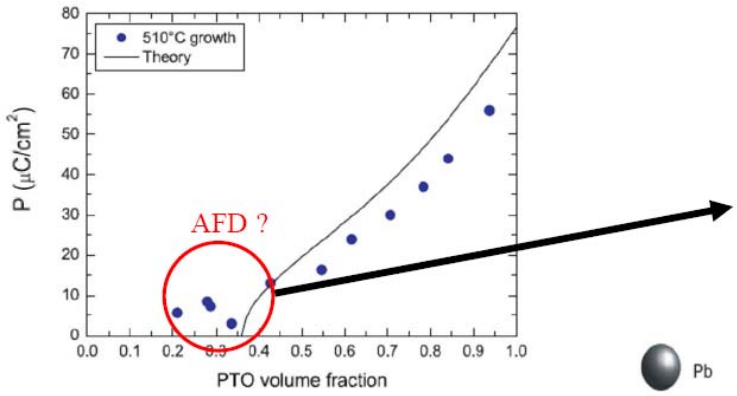

Figure 1.3.13: Polarization as a function of the PTO volume fraction in STO/PTO superlattices. Note that the polarisation seems to increase for low PTO volume fraction. After [123].

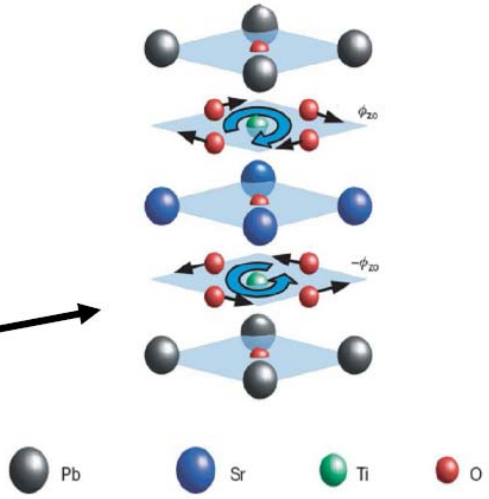

Figure 1.3.14: Schematic view of the $PbTiO_3/SrTiO_3$ superlattices and atomic motion associated to antiferrodistortive (AFD) mode. After [123].

Very recently, electrical investigations have been reported on almost freestanding single crystal $BaTiO_3$ that had been cut to thin film dimensions using focused ion beam (FIB) [129,130] (see Figure 1.3.15 (a) and (b)). Therefore, these BTO lamella (~ 100nm thick) are free from epitaxially induced strain from the substrate and are ideal for investigation of intrinsic properties. Remarkably, electrical and phase transition behaviour were found to be bulklike (c). Thus, this experimental approach gives an opportunity to systematically evaluate the effects of individual elements, which are suspected to contribute to the dramatic differences in functional response between bulk and thin films. Nevertheless, we also have to note that gallium etching induces Ga implantation in the lamellae. Thermal annealing has thus been performed in oxygen to repair the damage and expel the implanted Ga (see Figure 1.3.15 (d)). Additional experiments need to be performed to quantify the damage caused by focused ion beam processing (noted that the recorded capacitance value is abnormally low (femto-Farad) on (c)).

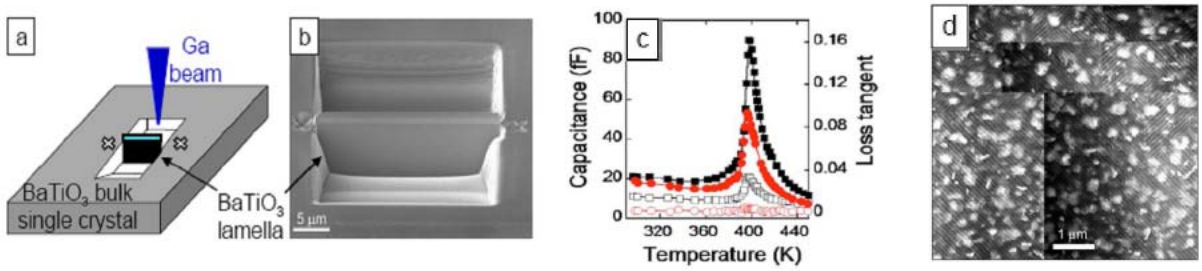

Figure 1.3.15: Different stages of a FIB process to fabricate a $BaTiO_3$ lamella for cross-sectional view: (a) schematic drawing. (b) FIB image of a lamella titled at 45 for a better viewing. (c) measured capacitance (filled data points) and loss tangent (unfilled data points) for $BaTiO_3$, annealed in oxygen (black squares) and nitrogen (red circles). (d) show TEM images of the annealed lamella, showing the expected Ga as clusters. (a) and (b) are reported from [130] whereas (c) and (d) are extract from [129].

1.3.5 Conclusion

We have seen that interface defects may contribute to the band alignment at the ferroelectric/electrode interfaces as in any metal/semiconductor contact. This can be of strong consequence for the investigation of the ferroelectric properties. Moreover, as for any oxides, the near surface region includes a large amount of charged defects which can even change the

structure and polarisation of ultratin films. These two interface contributions are thus to be deeply investigated. This is the main goal of the present work on the basis of in-situ XPS investigations of sputtered ferroelectric films.

1.4 Literature

[1] Polar Oxides, *Properties, Characterization, and Imaging*, (2005), Wiley, Weinheim.

[2] Introduction to Solid States Physics, (1956), C. Kittel. Wiley, New York.

[3] Nonoelectronics and Information Technology, Second, Corrected Edition, (2005), Wiley, Weinheim.

[4] R. Comes, M. Lambert and A. Guinier. (1968), *Solid State Communic.* **6**, pp. 715-719.

[5] H. Thomann, *Ferroelec.* (1987) **73**, pp. 183-199.

[6] S.M. Sze, *Physics of Semiconductor Devices*, (1981), Wiley, New York.

[7] C.T. Black, C. Farrell, and T.J. Licata. (1997), *Appl. Phys. Lett.* **71,** 2041.

[8] R.R. Mehta, B.D. Silverman, and J.T. Jacobs. (1973), *J. Appl. Phys.* **44**, 3379.

[9] J.F. Scott. (2000), *Ferroelectric Memories*, Springer, Berlin.

[10] M. Dawber, P. Chandra, P.B. Littlewood, and J.F. Scott. (2003), **15**, L393.

[11] M. Stengel, D. Vanderbilt, and N.A. Spaldin. (2009), *Nature Mat.* **8,** 392.

[12] His first major scientific contribution was the application of the concept of dipole moment to the charge distribution in asymmetric molecules in 1912, developing equations relating dipole moments to temperature and dielectric constant.

[13] K.S. Cole, and R.H. Cole. (1941), *J. Chem. Phys.* **9**, 341.

[14] P.W. Haayman, R.W. Dam, and H.A. Klasens. (1955), *German Patent*, **929,** 350.

[15] A. Erbil, Y. Kim, and R.A. Gerhardt. (1996), *Phys. Rev. Lett.* **77**, 1628.

[16] D.O´Neil, R.M. Bowman and J.M. Gregg. (2000), *Appl. Phys. Lett.* **77**, 1520.

[17] A.J. Moulson, and J.M. Herbert. (2003), *Electroceramics second edition*, edited by John Wiley & Sons.

[18] M.E. Lines and A.M. Glass. (1977), *Principles and Applications of Ferroelectrics and Related Materials*, Clarendon Press, Oxford.

[19] J.F. Scott. (2007), *Science*. **315**, 954.

[20] W. Heywang. (1971), *J. Mat. Sc.* **6,** 1214.

[21] W.J. Merz. (1954), *Phys. Rev. B.* **95**, 690.

[22] Vasalek. (1921), *Phys. Rev*. **17**, 475.

[23] H.C. Schweinler. (1952), *Phys. Rev*. **87**, 5.

[24] Discover simultaneously in several countries during the second war.

[25] T. Horie, K. Kawabe, M. Tachiki, and S. Sawada. (1955), J. Phys. Soc. Jap. **10**, 541. see also [17] p.78, fig. 2.46.

[26] Kay and Vousden. (1943), *Phil. Mag.* **40,** 1019.

[27] W.J. Merz. (1949), *Phys. Rev.* **76**, 1221.

[28] W.E. Lee. (2002), *University of Cambridge*, DoITPoMS Micrograph Library.

[29] L. Qiao, and X. Bi. (2008), *J. Cryst. Grow.* **310,** 5327.

[30] Y.L. Li, L.Q. Chen. (2006), *Appl. Phys. Lett.* **88,** 072905.

[31] K.J. Choi *et. al.* (2004), *Science*, **306,** 1005.

[32] R. Pérez *et. al*. (2007), *J. Appl. Phys*. **102,** 044117.

[33] Q.M. Zhang, H. Wang, N. Kim, and L.E. Cross. (1993), *J. Appl. Phys*. **75,** 454.

[34] M. Maglione. (2008), *J. Phys. Condens. Matter.* **20,** 322202.

[35] J. Seidel, *et. al.* (2009), *Nature Materials*. **8,** 229.

[36] V.L. Ginzburg and L.D. Landau. (1950), *Zh. Eksp. Teor. Fiz.* **20,** 1064.

[37] W. Cochran. (1969), *Advanc. Phys.* **18,** 157.

[38] H. Bilz, G. Benedek, and A. Bussmann-Holder. (1987), *Phys. Rev. B.* **35,** 4840.

[39] A. Filippetti, and N.A. Spaldin. (2003), *Phys. Rev. B.* **68,** 045111.

[40] A. Villesuzanne, *et. al.* (1998), *Eur. Phys. J. B.* **6,** 307.

[41] M. Stengel, D. Vanderbilt, and N.A. Spaldin. (2009), *Nature Materials,* **8,** 392.

[42] D.M. Smyth. (2000), *The defect Chemistry of Metal Oxides*, Oxford University Press, Inc.

[43] F.A. Kroger, and H.J. Vink. (1954), *Physica,* **20,** 950.

[44] P.W. Haayman, R. W. Dam and H. A. Klasens. (1955), *German Patent*, **929,** 350.

[45] G. Goodman. (1963), *J. Amer. Ceram. Soc.* **46,** 48.

[46] A.R. West, *et. al.* (2005), *J. Appl. Phys.* **98,** 094102.

[47] M.A.A. Issa. (1992), *J. Mat. Sc.* **27,** 3685.

[48] F.D. Morrison, A.M. Coats, D.C. Sinclair, and A.R. West. (2001), *J. Electroceram.* **6,** 219.

[49] D.M. Smyth. (2002), *J. Electroceram.* **9,** 179.

[50] P. Erhart, and K. Albe. (2008), *J. Appl. Phys.* **104**, 044315.

[51] J. Novak, and H. Arend. (1964), *J. Am. Ceram. Soc.* **47**, 530.

[52] G.H. Jonker. (1964), *Solid-State Elec.* **7,** 895.

[53] N. H. Chan, and D.M. Smyth. (1984), *J. Am. Ceram. Soc.* **67,** 285.

[54] N.G. Eror and D.M. Smyth. in *The Chemistry of Extended Defects in Non-Metallic Solids,* edited by L. Eyring and M.O. Keeffe (North-Holland Pub.Co., Amsterdam, 1970), p62.

[55] E.C. Subbaro, and G. Shirane. (1959), *J. Am. Ceram. Soc.* **42,** 279.

[56] G.A. Smolenskii, V.A. Isupov, and A.I. Agranovska. (1959), *Fiz. Tverd. Tela.* **1,** 1573.

[57] J.B. MacChesney, P.K. Gallagher, and F.V.D. Marcello. (1963), *J. Am. Ceram. Soc.* **46,** 197.

[58] S.N. Ruddlesden, and P. Popper. (1958), *Act. Cristallog.* **11**, 54.

[59] Y.H. Hu, M.P. Harmer, and D.M. Smyth. (1985), *J. Am. Ceram. Soc.* **68,** 372.

[60] H.M. Chan, M.P. Harmer, and D.M. Smyth. (1986), *J. Am. Ceram. Soc.* **69,** 507.

[61] S.B. Desu, and D. A. Payne. (1990), *J. Am. Ceram. Soc.* **73**, 3407.

[62] H. Beltran, E. Cordoncillo, P. Escribano, D.C. Sinclair and A.R. West. (2004), *J. Am. Ceram. Soc.* **87,** 2132.

[63] M. Drofenik. (1987), *J. Am. Ceram. Soc.* **70**, 311.

[64] G.V. Lewis, C.R.A. Catlow, and R.E.W. Casselton. (1985), *J. Am. Ceram. Soc.* **68**, 555.

[65] M.A. Subramanian, D. Li, N. Duan, B.A. Reisner, and A.W. Sleight. *J. Solid. State Chem.* (2000), **151,** 323.

[66] C.C. Holmes, T. Vogt, S.M. Sharpiro, S. Wakimoto, and A.P. Ramirez. (2000), *Science*, **293,** 637.

[67] D.C. Sinclair, T.B. Adams, F.D. Morrison, and A.R. West. (2001), *Appl. Phys. Lett*, **80,** 2153.

[68] M. Maglione. (2009), *Polarons, free charge localisation and effective dielectric permittivity in oxides*, to appear in Springer Series in Materials Science edited by G. Liu and V.Vikhnin.

[69] K. Szot, W. Speier. (1999), *Phys. Rev. B.* **60,** 5909.

[70] K. Szot, W. Speier, M. Pawelczyk, J.Kwapulinski, J. Hulliger, H. Hesse, U. Breuer and W. Quadakkers. (2000), *J. Phys. Condens. Matter*. **12,** 4687.

[71]: K. Szot, F.U. Hillebrecht, D.D. Sarma, M. Campagna, and H. Arend. (1985), *Appl. Phys. Lett.* **48,** 490.

[72] K. Szot, Ch. Freiburg, and M. Pawelczyk. (1991), *Appl. Phys. A.* **53,** 563.

[73] Y. Liang, and D.A. Bonnell. (1993), *Surf. Sci. Lett.* **285,** L510.

[74] R. Meyer, R. Waser, J. Helmbold, G. Borchardt. (2002), *J. Electroceram.* **9,** 87.

[75] A. Gunhold, K. Gömann, L. Beuermann, M. Frerichs, G. Borchardt, V. Kempter, W. Maus-Friedrichs. (2002), *Surf. Sci.* 507.

[76] B. Rahmati, J. Fleig, E. Bischoff, W. Sigle, J. Maier, M. Rühle. (2005), 2211.

[77] D.C. Meyer, *et. al.* (2006), *Appl. Phys. A.* **84,** 31.

[78] S.B. Lee, F. Phillipp, W.Sigle, M. Rühle. (2005), *Ultramicroscopy*, **105,** 30.

[79] K. Kinoshita, and A. Yamaji. (1976), *J. Appl. Phys.* **47,** 371.

[80] A.J. Bell, A.J. Moulson, and L.E. Cross. (1984), *Ferroelectrics.* **54**, 147.

[81] G.H. Jonker, and W. Heywang. (1962), *Science of Ceramics*, **1**, 255, Academic Press, New York.

[82] C.A. Mead.(1961), *Phys. Rev. Lett.* **6,** 545.

[83] T. Takeuchi, K. Ado, T. Asai, H. Kageyama, Y. Saito, C. Masquelier, O. Nakamura. (1994), *J. Am. Ceram. Soc.* **77,** 1665.

[84] M. Tanaka and Y. Makino. (1998), *Ferroelec. Lett.* **24,** 13.

[85] M. Anliker, H.R. Brugger, and W. Kanzig. (1954), *Helv. Phys. Acta.* **27,** 99.

[86] W. Kanzig. (1955), *Phys. Rev.* **98,** 549.

[87] Feng Tsai, and J.M. Cowley. (1994), *Appl. Phys. Lett.* **65,** 1906.

[88] J. Padilla, and D. Vanderbilt. (1997), *Phys. Rev. B.* **56,** 1625.

[89] C. Bungaro, and K.M. Rabe. (2005), *Phys. Rev. B.* **71,** 035420.

[90] R.I. Eglitis, and D. Vanderbilt. (2007), *Phys. Rev. B.* **76,** 155439.

[91] A.M. Kolpak, D. Li, R. Shao, A.M. Rappe, and D.A. Bonnell. (2008), *Phys. Rev. Lett.* **101,** 036102.

[92] M. Stengel, and N.A. Spaldin. (2006), *Nature Lett.* **443,** 679.

[93] C. Basceri, S.K. Streiffer, A.I. Kingon, and R. Waser. (1997), *J. Appl. Phys.* **82,** 2497.

[94] C. Zhou, and, D.M. Newns. (1997), *J. Appl. Phys.* **82,** 3081.

[95] M.M. Saad, P. Baxter, R.M. Bowman, J.M. Gregg, F.D. Morrison, and J.F. Scott. (2004), *J. Phys. Condens. Matter.* **16,** 451.

[96] R. Dittmann, R. Plonka, E. Vasco, N.A. Pertsev, J.Q. He, C.L. Jia, S. Hoffmann-Eifert, and R. Waser. (2003), *J. Appl. Phys.* **83,** 5011.

[97] J. Berge, A. Vorobiev, and S. Gevorgian. (2007), *Thin Solid Films*. **515,** 6302.

[98] R. Plonka, R. Dittmann, N.A. Pertsev, E. Vasco, and R. Waser. (2005), *J. Appl. Phys.* **86,** 202908.

[99] M. Dawber, and J.F. Scott. (2002), *Jpn. J. Appl. Phys.* **41,** 6848.

[100] C.L. Li, Z.H. Chen, Y.L. Zhou, and D.F. Cui. (2001), *J. Phys. Condens. Matter.* **13,** 5261.

[101] T. Yasumoto, N. Yanase, K. Abe, and T. Kawakubo. (2000), *Jpn. J. Appl. Phys.* **39,** 5369.

[102] K. Abe, N. Yanase, and T. Kawakubo. (2000), *Jpn. J. Appl. Phys.* **39,** 4059.

[103] A.J. Hartmann, M. Neilson, R.N. Lamb, K. Watanane, and J.F. Scott. (2000), *Appl. Phys. A.* **70,** 239.

[104] B.R. Chalamala, *et. al*. (1999), *Appl. Phys. Lett.* **74,** 1394.

[105] R. Schafranek, J. Schaffner, A. Klein. *J. Europ. Ceram. Soc.* (2009) doi:10.1016/j.jeurceramsoc.2009.05.009.

[106] J. Bardeen. (1947), *Phys. Rev*. **71**, 717.

[107] S. Kurtin, T.C. McGill, and C.A. Mead. (1969), *Phys. Rev. Lett*. **22**, 1433.

[108] V. Heine. (1965), *Phys. Rev*. **138**, A1689.

[109] J. Tersoff. (1984), *Phys. Rev. Lett*. **52**, 465.

[110] S.G. Louie, J.R. Chelikowsky, and M.L. Cohen. (1977), *Phys. Rev. B.* **15**, 2154.

[111] W.E. Spicer, P.W. Chye, P.R. Skeath, C.Y. Su, and I. Lindau. (1979), *J. Vac. Sci. Technol*. **16**, 1422.

[112] J. Tersoff. (1984), *Phys. Rev. Lett.* **52**, 465.

[113] W. Mönch. (2003), *Electronic Properties of Semiconductor Interfaces*, Springer-Verlag, Heidelberg.

[114] M. Cardona, and N.E. Christensen. (1987), *Phys. Rev. B.* **35**, 6182.

[115] A.M. Cowley, and S.M. Sze. (1965), *J. Appl. Phys.* **36,** 3212.

[116] R. Schafranek, S. Payan, M. Maglione, and A. Klein. (2008), *Phys. Rev. B.* **77,** 195310.

[117] M. Copel; P.R. Duncombe, D.A. Neumayer, T.M. Shaw, and R.M. Tromp. (1997), *Appl. Phys. Lett.* **70**, 3227.

[118] Y. W. Chung, and W.B. Weissbard. (1979), *Phys. Rev. B.* **20**, 3456.

[119] K. Abe, S. Komatsu, N. Yanase, K. Sano, and T. Kawakubo. (1997), *Jpn. J. Appl. Phys.* **36,** 5846.

[120] M. Okano, D. Sawamura, and Y. Watanabe. (1998), *Jpn. J. Appl. Phys.* **37,** 5101.

[121] O. Trithaveesak, J. Schubert, and Ch. Buchal. (2005), *J. Appl. Phys.* **98,** 114101.

[122] Y.S. Kim, J.Y. Jo, D.J.Kim, Y.J.Chang, J.H.Lee, T.W.Noh, T.K.Song, J.-G.Yoon, J.-S.Chung, S.I.Baik, Y.-W.Kim, and C.U.Jung. (2006), *Appl. Phys. Lett.* **88,** 072909.

[123] E. Bousquet, M. Dawber, N. Stucki, C. Lichtensteiger, P. Hermet, S. Gariglio, J.M. Triscone and P. Ghossez. (2008), *Nature lett.* **452,** 732.

[124] : M. Dawber, N. Stucki, C. Lichtensteiger, S. Gariglio, P. Ghosez, and J.M. Triscone. (2007), *Adv. Materials,* **19,** 4153.

[125] D.D. Fong, G.B. Stephenson, S.K. Streiffer, J.A. Eastman, O. Auciello, P.H. Fuoss, C. Thompson. (2004), *Science,* **304,** 1650.

[126] E. Hegenbarth. (1964), *Phys. Status Solidi,* **6,** 333.

[127] T. Leisegang *et. al.* (2009), *Phys. Rev. Lett.* **102,** 087601.

[128] M. Dawber, K.M. Rabe, and J.F. Scott, (2005), *Rev. Mod. Phys.* **77,** 1083.

[129] L.W. Chang, M. McMillen, and J.M. Gregg., (2009), *Appl. Phys. Lett.* **94,** 212905.

[130] I.A. Luk'yanchuk, A. Schilling, J.M. Gregg, G. Catalan, and J.F. Scott. (2009), arXig:0903.0764, to be published in *Phys. Rev. B.*

Chapter II

Experimental characterization methods and films preparation

2. Experimental characterization methods and films preparation

In this chapter, the emphasis is on the Photoelectron Spectroscopy (PES), which was used throughout the work as the main characterization method. A brief description on the electrical measurement setup will also be given as well as of the sputtering deposition technique which has been used for films preparation.

2.1 Introduction

The key functional properties that make ferroelectric materials so attractive in the first place, i-e. the large permittivity, are almost degraded in thin film form, as introduced in the first chapter (§1.3). The chemical composition and electronic structure of surfaces and interfaces play a major role in these degradations. Even for bulk materials, the macroscopical properties are drastically affected by interfaces like grain boundaries, domain walls or electrodes (see §1.2). After a large number of deep investigations, the near surface/interface chemistry of perovskite titanates structure ($ATiO_3$) remains poorly understood. X-ray photoelectron spectroscopy (XPS) has been proven to be an important analytical technique to study the near surface/interface chemistry of $ATiO_3$ compositions in the bulk form [1-11] and in thin film form [12-17]. This surface analysis has been typically used to investigate the contact formation with metal deposition [7,8,12,13,17,19] or more simply, to study the surface properties [1-6,9-11,14-16,18,20,21]. As a clean surface is required to study the intrinsic properties, various experimental processes have been used to obtain clean surface conditions during the experiment. Argon ion sputtering (IB), or Argon ion sputtering combined with annealing (IBA) were undertaken [1,2,3,5,16,17], vacuum fracture[6,9], in-situ scraping [10], acid treatment [18] as well as in-situ deposition [8,13,19] were performed prior to the measurement to obtain a clean surface. Some reports do not even mention any special pre-treatment [12,14,15,20,21]. The literature thus presents a contradictory and unclear picture of the electronic structure of $ATiO_3$ surfaces as deduced from core-level photoemission spectra [9]. In fact, the surface properties of $ATiO_3$ compounds can be rather complex and depend on processing conditions used to clean the surfaces [22]. For instance, if ion sputtering can effectively remove surface contaminations, it will also lead to disruption of chemical bonds

and therefore will create a high density of point defects and even extended defects on the investigated surface [2]. Therefore, great care is necessary to decide which species are affected or not by the surface cleaning step.

In addition, conducting samples are required for photoemission measurements. Since $ATiO_3$ ferroelectric stoichiometric compounds are usually insulators, charging effects can occur during the X-ray illumination. Typically, a low-energy flood gun is used to reduce surface charging [9,11]. But in some cases, the charging is too high to be fully compensated (e.g. for bulk materials) restricting the field of investigation. Charging can also be inhomogeneous along the investigated surface, leading to broadened and/or asymmetric peak shapes. Thermal annealing under reducing condition [1,2,6] or doping [4,8] might be suitable to obtain conducting ceramics to overcome the charging problem.

In this context, in-situ sample deposition is thus a straightforward way to prepare clean surfaces without the use of cleaning step. Thin film materials are also particularly convenient since the thickness is generally not large enough to induce surface charging (however, the substrate must be conducting). The emphasis of this paragraph is to describe the experimental approach used during this PhD work and particularly to explain what are the typical information collected. Thereafter, we will briefly describe the R.F magnetron sputtering method for thin film deposition. Finally, the setup used for dielectric measurements will be shown.

2.2 Photoelectron spectroscopy

Kai Siegbahn and his group have developed several significant improvements of photoelectron spectroscopy, which also often called Electron Spectroscopy for Chemical Analysis (ESCA). He received in 1981 the Nobel Prize to acknowledge his extensive efforts. Nowadays, Photoemission spectroscopy is a common technique for chemical surface analysis and extensively described in the literature [see e.g.22,23,24].

2.2.1 Information collected

Photoemission is based on the photoelectric effect (also termed Hertz effect), in which electrons are emitted from matter after absorption of photons such as X-rays. To achieve that, the energy of the photon required to extract the electron from the matter has to excess the

work function of the material. In addition, the kinetic energy of the collected electron must remains unaffected during the photoemission process. Thus, photoemission experiments are typically performed in ultra-high-vacuum (UHV) system, i.e. below 10^{-7} Pa. Indeed, in vacuum, the mean free path of the emitted electron is large enough for them to travel through an energy analyzer to a detector without scattering. In fact, the analyzer collects two kinds of electrons from the sample: (i) the primary electrons contributing to the chemical and electronic information and (ii) ineslatically scattered electrons contributing to the background intensity (secondary electrons). Both contributions can be appreciated in Fig. 2.2.1. For the primary electrons, the measured kinetic energy is directly coupled to their inelastic mean free path as sketched in Fig. 2.2.2 [25].

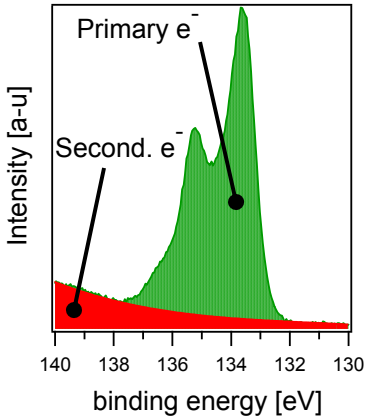

Figure 2.2.1: Typical Sr 3*d* XPS spectra recorded on $SrTiO_3$ material. The background line (red) is the result of secondary electrons collection.

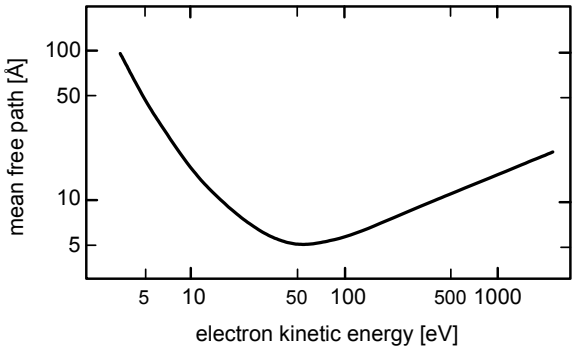

Figure 2.2.2: Inelastic mean free path of electrons in solids. This relation is also called "bathtube curve" [25].

The electron binding energy (BE) of each of the emitted electrons can be determined as following:

$$E_{binding} = h\nu - E_{kinetic} - \Phi_{sp} \qquad (2.2.1)$$

where $E_{binding}$ is the binding energy of the electron with respect to the Fermi energy of the spectrometer system, $h\nu$ is the energy of the X-ray photons being used, $E_{kinetic}$ is the kinetic energy of the electron measured by the instrument and Φ_{sp} is an instrumental parameter (work function of the spectrometer). As an electrical contact is established between the

sample and the spectrometer during the measurement, their respective Fermi energies (E_F) are aligned if the sample is conductive. Therefore, all the recorded binding energies are referenced to sample's Fermi level (the same between the sample and the spectrometer). This is particularly useful to know the position of the Fermi level (E_F) since any chemical change will be quantifiable thanks to this reference ($E_{binding}$ (FL) = 0 eV).

Typically, three kinds of measurements are performed during the surface analysis: (i) the survey spectrum which is used to identify all the chemical elements present at the surface, (ii) the recording of core levels at their characteristic binding energies which are tabulated, e.g., in the XPS handbook [24] and (iii) the valence band spectrum which provides important information on the Fermi level position, particularly useful to quantify the semiconducting character (p-type, n-type). Typical survey, core levels and valence band (VB) spectra are reported in Fig. 2.2.3 for a $BaTiO_3$ thin film.

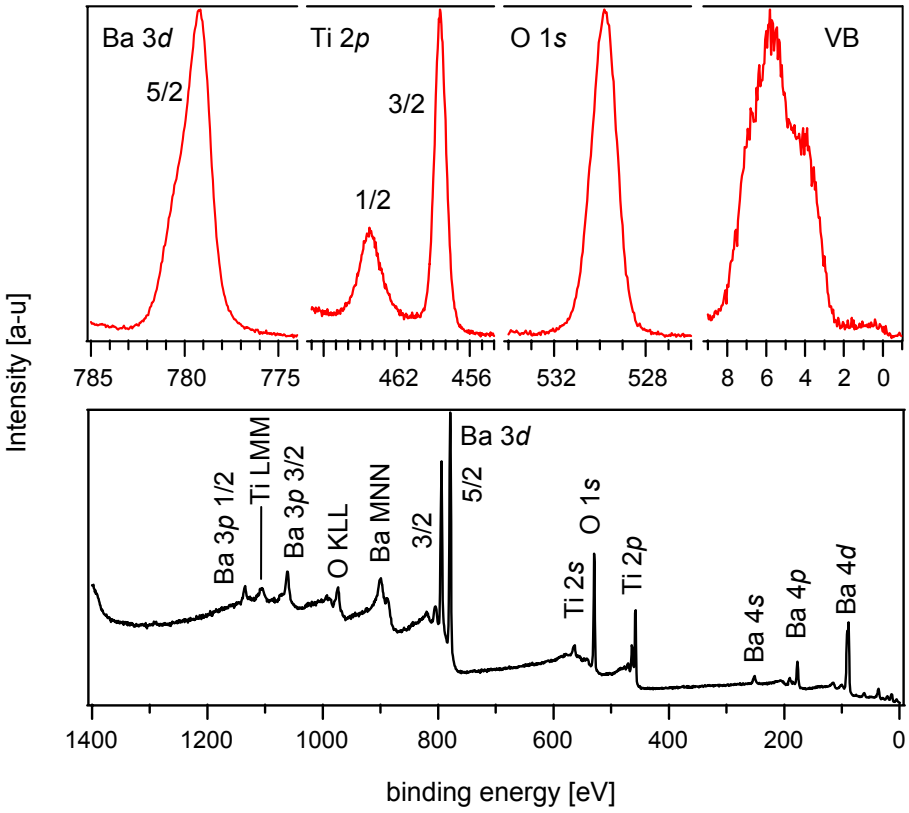

Figure 2.2.3: XPS core-levels (top) and survey (bottom) of a $BaTiO_3$ thin film recorded with monochromatized Al Kα radiation. The survey spectrum is typically used to determine all the elements present at the surface whereas detailed spectra (top) are used for fine analysis of chemical state, composition and electronic structure. As discussed above, 0 eV refer to the Fermi energy position.

With the core levels presented above, one can quantify the chemical composition of the observed surface. The relative composition (e.g. Ba vs. Ti) can be determined after background substraction of the secondary electrons (see Fig. 2.2.1). Different mathematical approaches can be used for the subtraction, for example with the methods described by Shirley [26] or Toogard [27]. After background subtraction, since the integrated intensity of a photoemission line depends on the atomic concentration of the respective elements, the stoichiometry can be determined. It is also important to note that the intensity of a photoemission line depends (i) on the geometry of the spectrometer and (ii) the measured element. Atomic Sensitivity Factors (ASF) have been defined to include (i) and (ii). Therefore, each element possesses its own ASF, related to the spectrometer being used. ASF are usually given by the manufacturer of the surface analysis system. For homogeneously distributed elements A and B, the relative concentrations are given by:

$$\frac{n_a}{n_b} = \frac{I_a . ASF_b}{I_b . ASF_a} \qquad (2.2.2)$$

where *n* is the concentration of the respective element and *I* the intensity of the photoemission line. Schafranek *et al.* have shown that stoichiometry calculations from XPS measurements can differ from those measured by Rutherford Backscattering Spectrometry RBS [28]. In fact, accurate absolute stoichiometry determinations by photoemission require well-known standard samples, which are often impossible to obtain. However, photoemission is well suited to detect changes in composition , for instance in dependence on sample treatment. It can be particularly useful to measure compositions with different take-off angles, in order to reveal a possible chemical change in the very near surface region as smaller take-off angles lead to a higher surface sensitivity. As exemplified in Fig. 2.2.4, we can observe a change on the Ba $3d_{5/2}$ spectra. This result shows a typical change in the Ba-coordination between surface and bulk. The details of the change will be discussed § 3.4. However since the decomposition of the Ba3d line in two components will be reported at several places in this manuscript, we specify now the notations that will be used. The lower energy component which is resulting from bulk barium will be called Ba1 while the higher energy part which is stronger for the barium located at the near surface will be named Ba 2

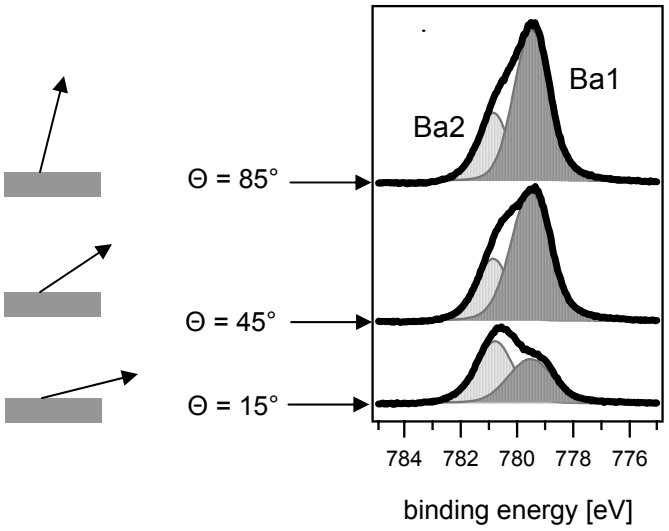

Figure 2.2.4: Ba $3d_{5/2}$ core level spectra of a clean $BaTiO_3$ surface. Different takeoff angle have been used as schematized on the left side. At low angle (surface), the light-grey component is much more pronounced

2.2.2 XPS in $ATiO_3$ compounds

The valence band (VB) emission presented Fig. 2.2.3 shows a well-known two peak structure extending approximately 8 eV below the Fermi Energy (FE) level (FE = 0 eV). This typical emission has been observed at $SrTiO_3$ single crystal [9,29], ceramic and single crystals of $BaTiO_3$ [1,2,30], single crystals of $KNbO_3$ [30], and thin films of $(Ba,Sr)TiO_3$ [8,13,19]. To facilitate the discussion, the valence band (VB) emission of Nb-doped $SrTiO_3$ single crystal and $BaTiO_3$ thin film are reported in Fig. 2.2.5 with the annotations **A**, **B** and VBM.

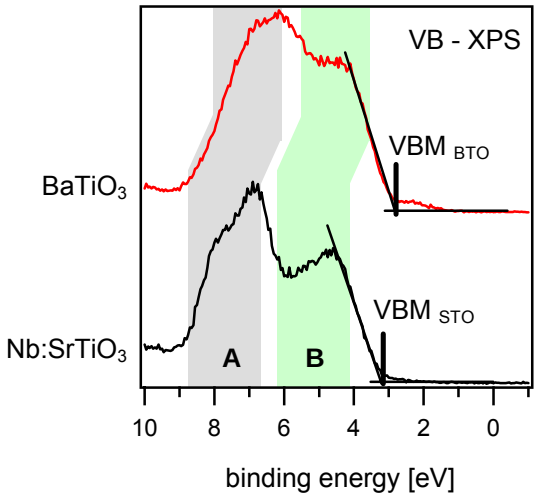

Figure 2.2.5: XPS valence band spectra of $SrTiO_3$:Nb single crystal and $BaTiO_3$ thin film. Two well-defined structures are denoted A and B and discussed in the text. The VBM positions are also reported.

B corresponds to the O 2*p* nonbonding states, while **A** denotes the bonding between the O 2*p* and Ti 3*d* states [6]. We thus clearly see that the valence band is mainly of oxygen 2*p* character and show a significant degree of covalent character in the Ti 3*d* – O 2*p* bonding, which is expected in $ATiO_3$ compounds [31]. Since $SrTiO_3$:Nb is single crystalline and highly conducting, the peak structure is more pronounced than for the polycrystalline, low conducting $BaTiO_3$ thin film.

The valence band maxima (VBM) of the spectra are determined by linear extrapolation of the leading edge of the valence band emission as the zero of binding energy corresponds to the Fermi level position. Since the optical band gap of $SrTiO_3$ and $BaTiO_3$ is ~ 3.2 eV [32], a VBM value recorded around 3 eV, indicate a n-type semiconducting character (Fermi Energy position close to the conduction band). The VBM value recorded with its presented Nb:$SrTiO_3$ sample (VBM_{STO}) exhibit a value of 3.1 eV, in good agreement with the expected semiconducting character. At the surface of the shown $BaTiO_3$ thin film, the measured VBM_{BTO} is located at 2.4 eV, denoting a more resistive character. The VBM position will be largely discussed in the course of the manuscript, for instance in dependence of thermal treatment. (see § 3.3).

2.2.3 Typical experiments

In photoemission, samples can be prepared ex-situ, i.e. prepared outside the vacuum system and inserted in the analysis chamber. Therefore, a surface treatment is required to clean the surface. During this PhD work, in-situ experiments have been performed; the preparation chamber (or deposition chamber) was directly connected to the analysis chamber by an ultra-high vacuum sample transfer system. The layout of this system which is operated by the surface science group at TU Darmstadt is sketched in Fig. 2.2.6.

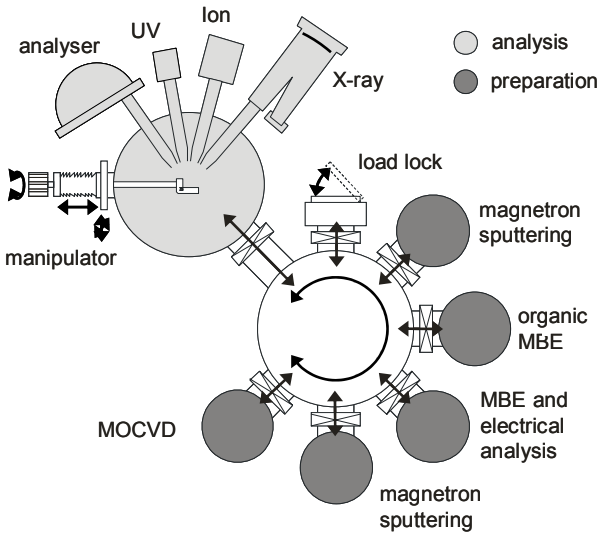

Figure 2.2.6: Layout of the integrated ultra-high vacuum system combining a multi-technique surface analysis system including a photoelectron spectrometer for XPS and UPS. Several chambers for thin films deposition are connected to the system, like magnetron sputtering deposition used during this PhD.

With such setup, the surface properties of $BaTiO_3$ thin films have been studied in dependence of thermal treatment and sputtering deposition conditions (see III.3.1.1 and III.3.4). Furthermore, interfaces between two different materials (e.g. Substrate/film or film/metal) have also been measured using a step-by-step deposition approach (see III.3.1.2 and III.3.1.3). We are now going to briefly describe the sputtering deposition technique which has been used for thin film growth.

2.3 Magnetron sputtering deposition

This section concentrates on magnetron sputtering. Sputtering is the removal of atomized material from a solid due to energetic bombardment of its surface layers by ions or neutral particles. Prior to the sputtering procedure, a vacuum of less than ten millionth of an atmosphere must be achieved. From this point, a closely controlled flow of an inert gas such as argon is introduced. This raises the pressure to the minimum needed to operate the magnetrons, although it is still only a few ten thousandth of atmospheric pressure. When power is supplied a negative voltage of typically ~ 50/100V or more is applied to the target. This negative voltage attracts high speed positive ions (e.g. argon) to the target surface. Usually, when a positive ion collides with atoms at the surface of a solid an energy transfer occurs. If the energy transferred to a lattice site is greater than the binding energy, primary recoil atoms can be created which can collide with others atoms and distribute their energy via collision cascades. The situation is summarized in Fig. 2.3.1.a. Sputtering of a target atom is just one of the possible results of ion bombardment on a surface. The other possibilities are summarized in Fig. 2.3.2.b. Aside from sputtering, the second important process is the emission of secondary electrons from the target surface. These secondary electrons enable the discharge to be sustained.

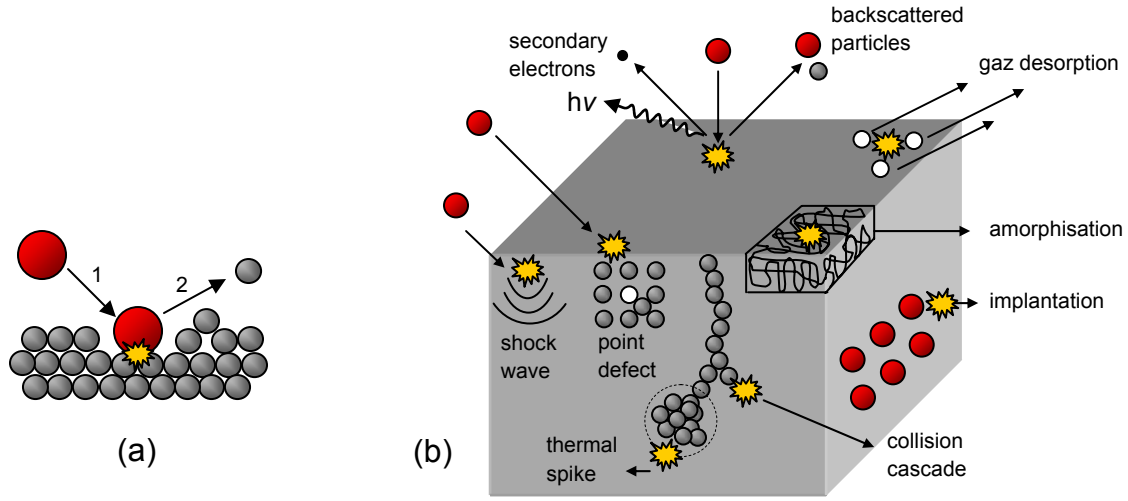

Figure 2.3.1: (a): Sputtering of a target atom (grey) by ion bombardment (red) resulting in collision cascades and backscattered particles. (b): summarized the other possibilities also occurring in a sputtered material. The emitted secondary electrons enable the discharge to be sustained.

During the sputtering process a magnetic field can be used to trap secondary electrons close to the target. The electrons follow helical paths around the magnetic field lines increasing the probability for ionizing collisions with neutral gas atoms near the target. Thereby the gas pressure can be reduced, leading to a higher deposition rate. The sputtered atoms are neutrally charged and so are unaffected by the magnetic trap. The conventional planar magnetron has been designed such that a looping magnetic field round the inner and outer magnet pole confines the plasma in a closed loop on the target surface, as exemplified in Fig. 2.3.2.

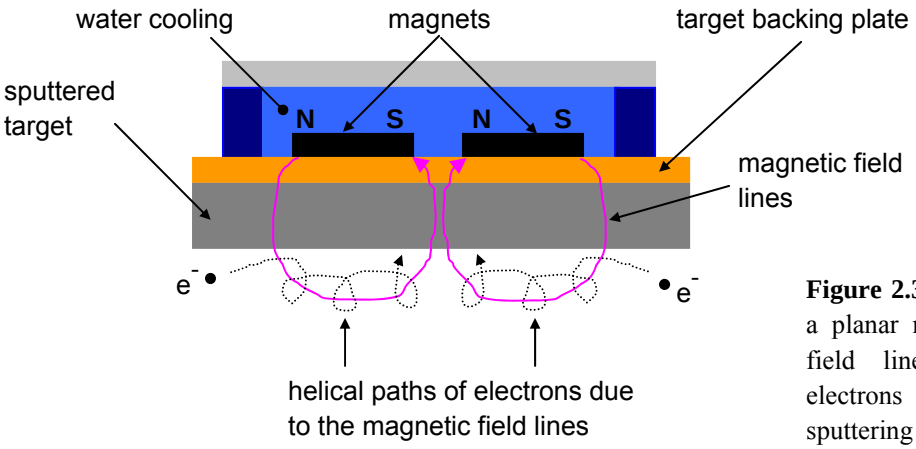

Figure 2.3.2: Schematic diagram of a planar magnetron. The magnetic field lines trap the secondary electrons increasing thus the sputtering yield.

Since $BaTiO_3$ is an oxide, it is necessary to inject in the plasma a gas mixture of argon and oxygen (reactive mode sputtering (RMS)) in order to obtain stoichiometric deposition. The resulting film properties are affected by several factors such as the sputtering power, the work pressure, the composition of the gas (Ar vs. O_2), the position of the substrate with respect to the target and mainly the substrate temperature [33]. These factors depend on each other and the optimum deposition parameters have to be found prior to the experiment. The influence of sputtering deposition conditions on the $BaTiO_3$ surface properties are discussed in III.3.1.1.

During this PhD, the films have been mostly sputtered under on-axis configuration, i.e., with the substrate facing the target (see figure 2.3.3). With such geometry, resputtering from the film surface can arise from fast ions collisions complicating faithful composition transfer from the target to the film. In $ATiO_3$ compounds, Ti excess has been frequently reported in sputtered thin films due to preferential Ba resputtering or re-evaporation [34–36]. The Institute of Condensed Matter Chemistry of Bordeaux (ICMCB) has recently been equipped with a sputtering deposition chamber in off-axis configuration (see Fig. 2.3.3). This technique, developed at Stanford University [37], places the target at 90° to the substrates plane reducing thus the effect of the ion resputtering. The resputtering effect occurs particularly when volatile elements are deposited like Pb in $Pb(Zr,Ti)O_3$ compositions [38].

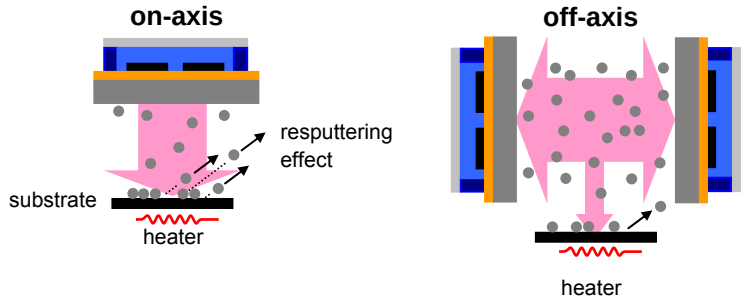

Figure 2.3.3: **Left**: on-axis configuration. Due to fast ions collisions, resputtering effect occurs. **Right**: off-axis geometry reducing the growth rate and thus the energy transfer collision on the substrate

We have also deposited $BaTiO_3$ and $(Ba,Sr)TiO_3$ thin films using the off-axis sputtering system geometry. The dielectric properties of thin films sputtered under on/off-axis conditions are compared in section III.3.2. In the following paragraph, the dielectric setup for impedance spectroscopy is reported.

2.4 Impedance spectroscopy setup for thin films

Metal/Insulator/Metal (MIM) capacitor structures have been used to perform the electrical characterization. With such a geometry, one can easily deduce the permittivity value following:

$$\varepsilon_R = \frac{C.t}{\varepsilon_0.S} \tag{2.2.3}$$

where ε_r is the relative permittivity of the film, C its capacitance, t the film thickness, S the surface of the electrode and ε_0 represents the vacuum permittivity. The Pt top electrodes are deposited of room temperature using rf magnetron sputtering through a 12-hole mask after etching to previously clean the surface. Typically, two kinds of measurements can be carried out: (i) at room temperature using a probe tip station; the electrical connection between the impedance analyzer and the films is achieved through a Karl Süss wafer holder including two tips that can be pressed to the metal electrodes, and (ii) under variable temperature, using a home-made cell connected alternatively to a membrane-pump and helium so that no humidity could affect the measurement, (see Fig. 2.4.1). In both cases (i) and (ii), the dielectric properties (capacitance and dielectric losses) are measured using an HP4194A impedance analyzer with a frequency which can be swept between 100Hz and 10MHz.

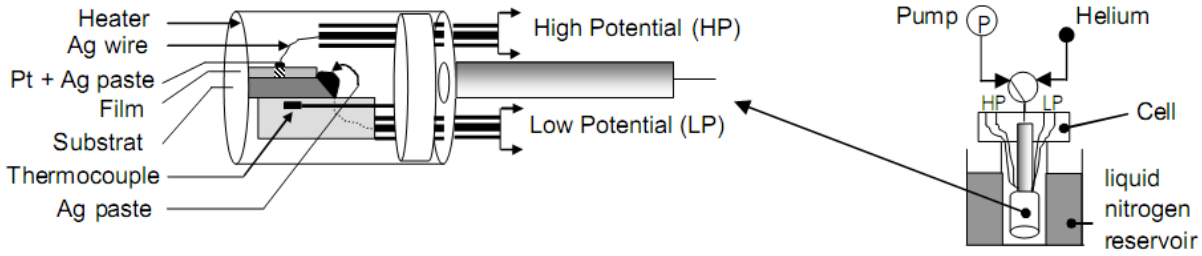

Figure 2.4.1: Sketch of the cell used for thin films impedance spectroscopy. On the right side, the cell has been plunged into liquid nitrogen for measurement. The contact with the top and the bottom electrodes are showed in details on the left side. The hatching area represents the volume investigated.

2.5 Literature

[1] L.T. Hudson, R.L. Kurtz, S.W. Robey, D. Temple, and R.L. Stockbauer. (1993), *Phys. Rev. B.* **47**, 16.

[2] B. Cord, and R. Courths. (1985), *Surf. Sci.* **152**, 1141.

[3] S. Kumar, V.S. Raju, T.R.N. Kutty. (2003), *Appl. Surf. Sci.* **206**, 250.

[4] H. Jena, V.K. Mittal, S. Bera, S.V. Narasimham, K.V. Govindan Kutty, and T.R.N. Kutty. (2008), *Appl. Surf. Sci.* **254**, 7074.

[5] M. Wegmann, L. Watson, and A. Hendry. (2004), *J. Am. Ceram. Soc.* **87**, 371.

[6] L.T. Hudson, R.L. Kurtz, S.W. Robey, D. Temple, and R.L. Stockbauer. (1993), *Phys. Rev. B.* **47**, 1174.

[7] B. Psiuk, J. Szade, H. Schroeder, H. Haselier, M. Mlynarczyck, R. Waser, and K. Szot. (2007), *Appl. Phys. A.* **89**, 451.

[8] M. Copel, P.R. Ducombe, D.A. Neumayer, T.M. Shaw, and R.M. Tromp. (1997), *Appl. Phys. lett.* **70**, 3227.

[9] J.D. Baniecki, M. Ishii, K. Kurihara, K. Yamanaka, T. Yano, K. Shinozaki, T. Imda, K. Nozaki, and N. Kin. (2008), *Phys. Rev. B.* **78**, 195414.

[10] K. Szot, F.U. Hillebrecht, D.D. Sarma, M. Campagna, and H. Arend. (1985), *Appl. Phys. Lett.* **48**, 490.

[11]: K. Szot, W. Speier, U. Breuer, R. Meyer, J. Szade, and R. Waser. (2000), *Surf. Sci.* **460**, 112.

[12] X.L. Li, B. Chen, H.Y. Jing, H.B. Lu, B.R. Zhao, Z.H.Mai, Q.J. Jia. (2005), *Appl. Phys. Lett.* **87**, 222905.

[13] R. Schafranek, S. Payan, M. Maglione, and A. Klein. (2008), *Phys. Rev. B.* **77**, 195310.

[14] D. Ehre, H. Cohen, V. Lyahovitskaya, and I. Lubomirsky. (2008), *Phys. Rev. B.* **77**, 184106.

[15] J.D. Baniecki, M. Ishii, T. Shioga, K. Kurihara, and S. Miyahara. (2006), *Appl. Phys. Lett.* **89**, 162908.

[16] V. Craciun, and R.K. Singh. (2000), *Appl. Phys. Lett.* **76**, 1932.

[17] M. Kurasawa, and P.C. McIntyre. (2005), *J.Appl.Phys.* **97**, 104110.

[18] Y. Fujisaki, Y. Shimamoto, and Y. Matsui. (1999), *Jpn. J. Appl. Phys.* **38**, L52-L54.

[19] R. Schafranek, and A. Klein. (2006), *Solid. Stat. Ionics*. **177**, 1659.

[20] K. Szot, H. Hoffmann, W. Speier, U. Breuer, M. Siegert, and R. Waser. (2000), *Int. Ferroel.* **33**, 303.

[21] M. Mlynarczyk, K. Szot, A. Petraru, U. Poppe, U. Breuer, R. Waser, and T. Tomala. (2007), *J. Appl. Phys.* **101**, 023701.

[22] A. Klein, T. Mayer, A. Thissen, and W. Jaegermann. *Photoelectron Spectroscopy in Materials Science and Physical Chemistry: Analysis of Composition, Chemical Bonding and Electronic Structure of Surfaces and Interfaces*, Bunsenmagazin **10** (2008), 124.

[23] M. Cardona, and L. Ley. (1979), *Photoemission in Solids*, SpringerVerlag, Berlin.

[24] J.F. Moulder, W.F. Stickle, P.E. Sobol, and K.D. Bomben. (1992), *Handbook of X-ray Photoelectron Spectroscopy*, Perkin-Elmer Corp., Eden Prairie, MN, USA.

[25] S. Tanuma, C.J. Powell, and D.R. Penn. (1991), *Surface and Interface Analysis*, **17**, 911.

[26] S.P. Kowalczyk, F.R. McFeely, L. Levy, V.T. Gritsyna, and D.A. Shirley. (1977), *Solid. St. Commun.* **23**, 161.

[27] S. Tougaard. (1986), *Phys. Rev. B.* **34**, 679.

[28] R. Schafranek, A. Giere, A.G. Balogh, T. Enz, Y. Zheng, P. Scheele, R. Jakoby, and A. Klein. (2008), *J. Eur. Ceram. Soc.* **29**, 1433.

[29] V.E. Henrich. (1978), *Phys. Rev. B.* **17**, 4908.

[30] P. Pertosa, *et. al,* (1978), **17**, 2011.

[31] H. Thomann. (1987), *Ferroel.* **73**, 183.

[32] M. Cardona. (1965), *Phys. Rev. B.* **140**, A651.

[33] V. Reymond, D. Michau, S. Payan, and M. Maglione. (2004), *J. Phys. Cond. Mat.* **16**, 9155.

[34] X. Wang, U. Helmersson, L. D. Madsen, I.P. Ivanov, P. Münger, S. Rudner, B. Hjövarsson, and J.E. Sundgren. (1998), *J. Vac. Sc. Technol. A.* **17**, 564.

[35] J. Im, O. Auciello, P. Baumann, S.K. Streiffer, D.Y. Kaufman, and A.R. Krauss. (2000), *Appl. Phys. Lett.* **76**, 625.

[36] V. Reymond. (2004), *Thesis*, University of Bordeaux.

[37] C.B. Eom *et. al.* (1989), *Appl. Phys. Lett.* **55**, 595.

[38] J.M. Triscone *et. al.* (1996), *J. Appl. Phys.* **79**, 4298.

Chapter III

Results and discussion

This Chapter III is composed of 5 sections as follow:

Brief description

3.1 Surface and interface properties

The first section describes (i) the influence of sputtering conditions in surface properties of sputtered $BaTiO_3$ thin films, (ii) contact formation with top electrode and, (iii) contact formation with bottom electrode.

3.2 Dielectric properties and microstructure

After having investigated the electrode/film contact formation in the previous section, we show in section 3.2 the actual dielectric properties of such stacks.

3.3 Surface segregation in Nb-doped $BaTiO_3$ thin films

The electrical properties of donor-doped $BaTiO_3$ are first compared between thin films and ceramics according the literature. The results are much more contrasted in thin film form. We suggest that dopant segregation at the surfaces can occurs as probe in our sputtered thin films.

3.4 Surface layer of $BaTiO_3$ thin films under oxidation condition

This section also compares thin film and bulk surface properties when subsequently annealed. It has been demonstrated that subsequent stoichiometry change occurs in the near-surface region under thermal treatment.

3.5 The Ba components

This last section is discussing the Ba components observed in the photoemission spectra. Typical splitting of Ba levels have been observed and debated in the literature. We compile the major results of this PhD related to this question.

3.1 Surface and interface properties

3.1.1 Influence of sputtering deposition parameters on surface properties of $BaTiO_3$

In this section the influence of sputtering conditions of $BaTiO_3$ thin films on their properties are investigated with the help of photoemission spectroscopy (XPS) and X-ray diffraction (XRD). Target to substrate distance, oxygen content, substrate orientations, and doping concentrations were used as parameters. Fermi level position, surface stoichiometry and core-level emissions have been studied in dependence of these parameters. Finally, the surface properties of Nb-doped $SrTiO_3$ single crystal will also be described since they are well-known to be suitable as bottom electrode.

3.1.1.1 $BaTiO_3$ deposited onto polycrystalline Pt

In order to find the optimal deposition parameters to obtain stoichiometric and crystallized BTO thin films, sputtering has been performed under several conditions and characterized with XPS and XRD. This approach is particularly fruitful to tune the parameters in function of the observed surface properties.

Thin film depositions were carried out by radio-frequency magnetron sputtering using ceramic targets of 2 in. diameter, a power of 25 W (power density = 1.22W/cm²), a total gas pressure of 0.5 Pa, an Ar/O_2 gas mixture of 99/1 (1% O_2), a substrate temperature of 650°C at varying substrate to target distances (5, 7, 9 and 10 cm). Figure 3.1.1.1 shows typical XRD patterns of BTO thin films deposited onto platinised (111) Si wafers with different target to substrate distances. The patterns give evidence that the films are free of parasitic phases whatever the distance. In addition, no preferential crystallographic orientations can be observed as expected with deposition on polycrystalline substrate. It is clear that the target to substrate distance does not induce fundamental change in the structural properties. However, electronic and chemical surface properties analyzed by XPS have been drastically modified for the same samples as shown in Fig. 3.1.1.2.

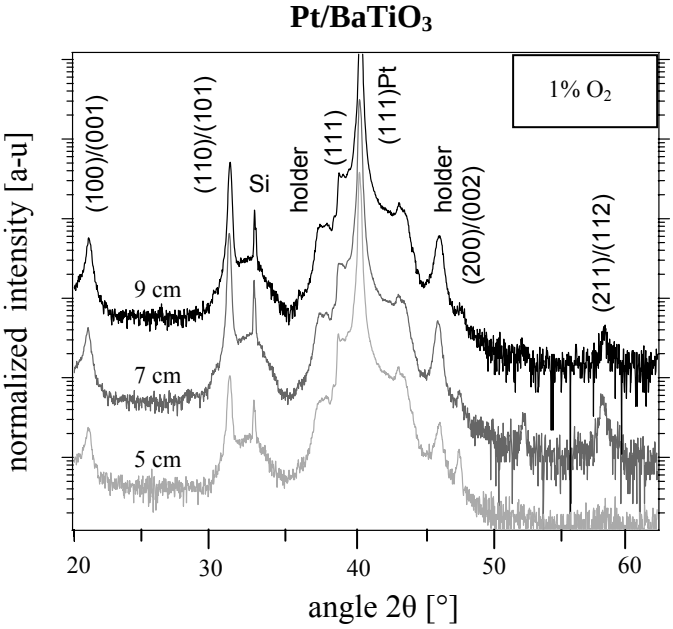

Figure 3.1.1.1: XRD diffraction patterns of BTO deposited onto polycristalline Pt(111) at different target to substrate distances. No preferential orientations and absence of extra-peak can be observed. Therefore, deposition at varying distances does not induce significant change in the microstructure.

The valence band maximum (VBM) position with respect to the Fermi energy (E_F) is plotted versus substrate to target distance for several gas mixture ratio (Ar/O_2) in Figure 3.1.1.2. The oxygen content is indicated in percent in the graph with respect to the total gas mixture. Thin films measured with XRD measurements are reported in the graph (red). A clear Fermi energy shift toward lower values is observed when increasing target to substrate distance. In addition, similar tendency is observed under increased oxygen content which also induces a downshift of the Fermi level. This strongly suggests a reduced state when sputtering is performed at low oxygen content leading to *n*-type character.

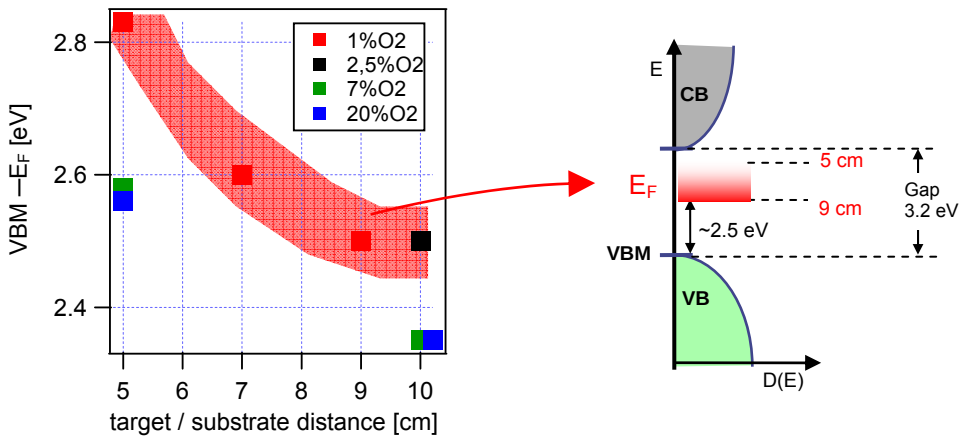

Figure 3.1.1.2: Valence band maximum (VBM) with respect to the Fermi energy (E_F) evolution in function of target to substrate distance. E_F decreases for higher distances and higher oxygen content used during sputtering. This lowering indicates a decreasing of charge carrier density at the surface inducing a shift in the Fermi level as sketched on the right side.

For the highest target to substrate distance (10cm) and for anomalously high oxygen partial pressure, XRD results have shown the occurrence of parasitic phases mainly from Ba-rich origin (Fig. 3.1.1.3).

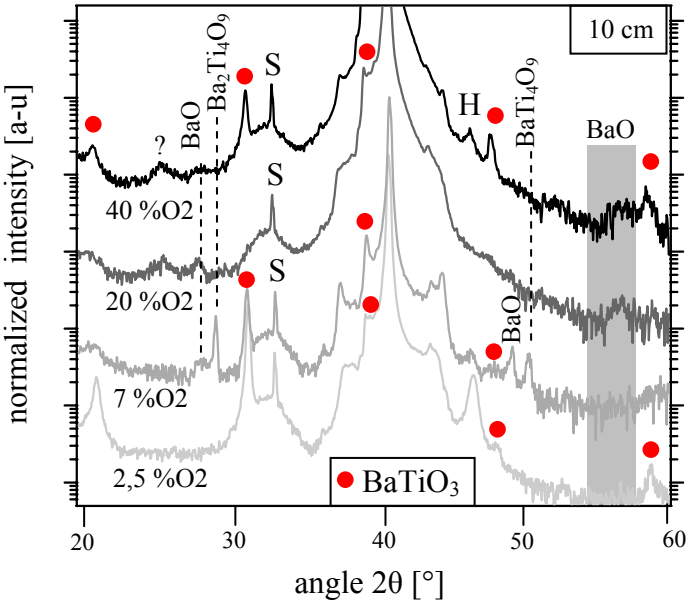

Figure 3.1.1.3: XRD diffraction patterns of BTO deposited onto polycristalline Pt(111) with different oxygen contents. Numerous extra peaks appear when the oxygen content is increased. $\%O_2$ is thus more influent than substrate to target distance on the film microstructure properties. The parasitic phases are mainly Ba-rich related in good agreement with our stoichiometry calculations derived from XPS (see Fig. 3.1.4).

If the Fermi energy position is shifted under different sputtering conditions (fig 3.1.1.2), the chemical compositions derived from photoemission spectroscopy are also submitted to modifications as shown in Fig. 3.1.1.4. The cationic (Ti/Ba) ratio has been plotted versus the target to substrate distance for different oxygen contents. Clear Ti-rich surfaces are observed at low distances. The Ti-excess can be reduced by increasing the distances and for high oxygen content. Ba-rich surface has even been obtained at 10cm with 20% of O_2. Resputtering or re-evaporation effect is often involved [1-3] to explain the observed Ti-excess for undoped $ATiO_3$ compositions. For small target to substrate distance, the sputtered species reach the substrate with high kinetic energy. This probably leads to preferred resputtering of Ba leaving thus a titanium excess of 10─20% most probably located at the grain boundaries. Thus, simultaneous adjustment of distance and oxygen content are necessary to obtain thin films free of parasitic phase and reasonable surface stoichiometry. We note that ex-situ XPS with Ar ion sputtering for surface cleaning can hardly be used for such composition analysis since the defects created during the cleaning step preclude a right integration of the Ti XPS lines.

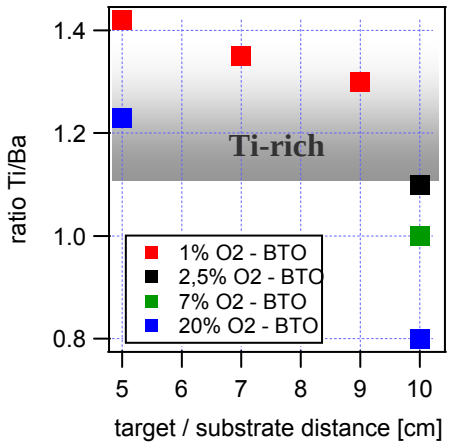

Figure 3.1.1.4: Cationic ratio (Ti/Ba) versus target to substrate distance. A clear Ti excess is observed at low distance and low oxygen content whereas Ba excess is found for subsequent oxygen content at 10cm.

The Fermi level position can also be plotted as a function of the oxygen partial pressure during deposition (Fig.3.1.1.5). E_F is mostly modified at low oxygen concentration (less than 7%). Again, the creation of surface charges leading to the up-shift of the Fermi level is ascribed to resputtering effects which are reduced on increasing oxygen partial pressure. This lower resputtering of Ba ions results from the lower mean free path of ionised Argon ions in oxygen-rich plasmas.

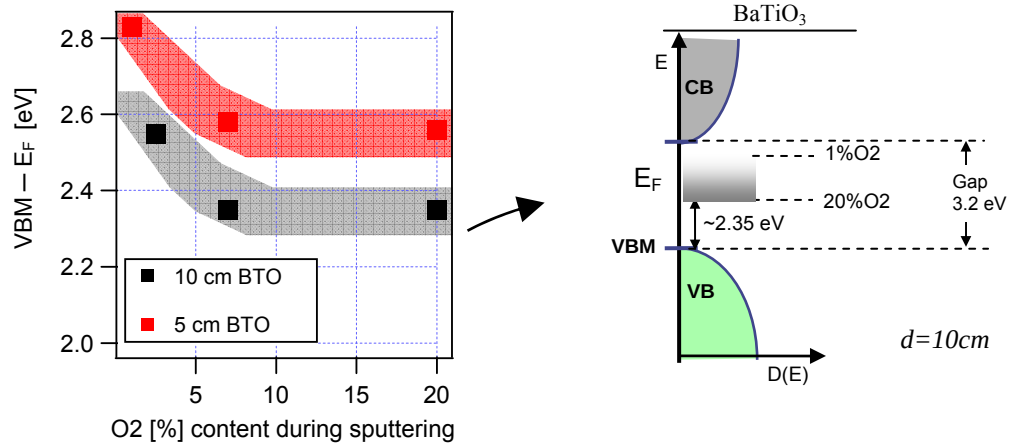

Figure 3.1.1.5: Valence band maximum (VBM) with respect to the Fermi energy (E_F) evolution in function of the oxygen content used during sputtering. E_F decreases for higher oxygen content. The situation is summarized through a schematic energetic band diagram.

Up to now, we have seen a clear dependence of electronic and chemical surface properties under different sputtering conditions. By varying the substrate to target distance (*d*), we did not observe any significant change in the structural parameters. However, decreasing *d* leads to Ti surface enrichment and shifts the Fermi level towards higher values (denoting *n*-type character). Depositions performed at high oxygen partial pressure give rise to parasitic phases

attributed as Ba-rich phases in good agreement with the observed Ba excess derived in in-situ XPS. Reasonable surface stoichiometry can be achieved using a substrate to target distance of 10cm with an oxygen content of 2.5 %. These parameters were thus used as typical deposition conditions in the following of this report.

3.1.1.2 Intrinsic BTO and Nb-doped BTO deposition

In bulk materials, one can substantially decrease the resistivity of $ATiO_3$ compounds using donor dopant (e.g. Nb^{5+}, or La^{3+}), as discussed in section I.1.2. In this context, one can expect different Fermi level positions between pure $BaTiO_3$ and donor-doped $BaTiO_3$ samples. Such electronic level tuning is usually inferred indirectly from macroscopic experiments on bulk samples. The present section is aimed at showing directly these effects in thin films. We have shown above that photoemission spectroscopy is particularly powerful to locate the Fermi level by recording the valence band (VB) emission. Consequently, Nb-doped $BaTiO_3$ target has been sputtered to obtain semi-conducting thin films and to compare the surface properties of intrinsic BTO and Nb-doped BTO. It will be the topic of section III.3.3 to show all the details of such Nb doping effect on electronic levels. However, since influence of substrate orientation is studied in the next paragraph for Nb-doped BTO thin films, we show now the overall difference between pure and Nb-doped BTO thin films (see Fig. 3.1.1.6).

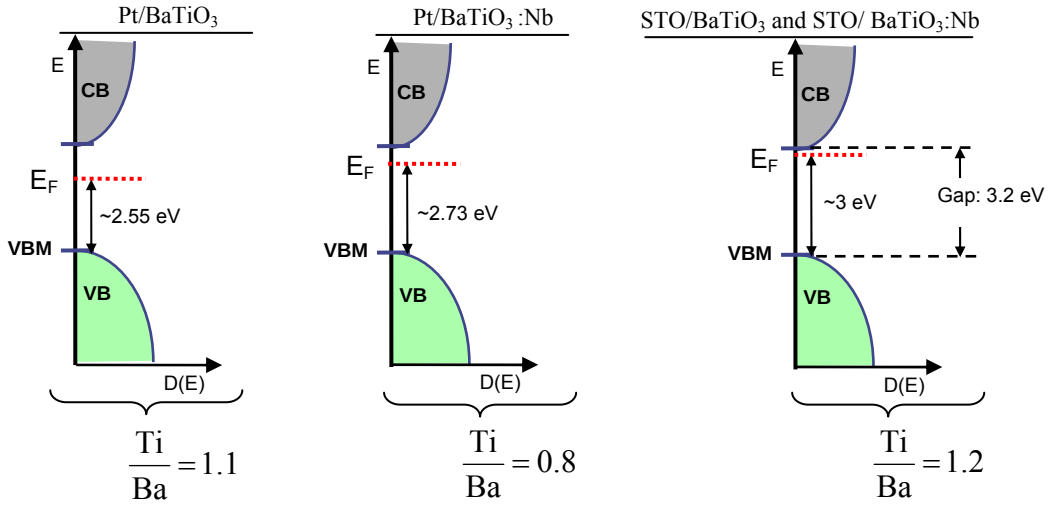

Figure 3.1.1.6: Fermi level position for pure and Nb-doped BTO thin films deposited onto Pt(111) and STO:Nb(100) using the optimised deposition conditions determined in the first paragraph. For Pt/BTO thin film, the E_F values are derived from the previous paragraph. However, Pt/BTO:Nb exhibit higher Fermi level due to doping effect (see **III**.3.3). For STO:Nb crystal substrates, no change is observed in the Fermi level on Nb doping of the films.

Nb-doped $BaTiO_3$ target with 0.05 wt% niobium concentration was sputtered using optimised deposition conditions determined in the previous paragraph (10cm, 2,5% O_2, 650°C, 5 Pa). For Si/Pt substrates, we observe an increase of the Fermi level for BTO:Nb as expected for *n*-type doping. However similar depositions onto single crystal of $SrTiO_3$:Nb do not produce any change in the Fermi level. The films exhibit a strong *n*-type character whatever their Nb content as evidenced by the Fermi energy position located just below the conduction band. This difference between Si/Pt and $SrTiO_3$:Nb substrates is quite important since the latter are often used in the literature as reference for the large scale use of Si/Pt wafers. These results are commented in details in section III.3.3. The purpose of the present paragraph was rather to introduce the substrate influence which induces obviously different surface properties for identically sputtered $BaTiO_3$ films with and without Nb doping. To attempt a clarification, different substrate orientations were compared for sputtered thin films of BTO:Nb.

3.1.1.3 Influence of substrate orientation

We have compared BTO:Nb films deposited onto STO(111) and (100) as well as Pt(111) and (200). The corresponding XRD patterns for all the films are shown on Fig. 3.1.1.7.

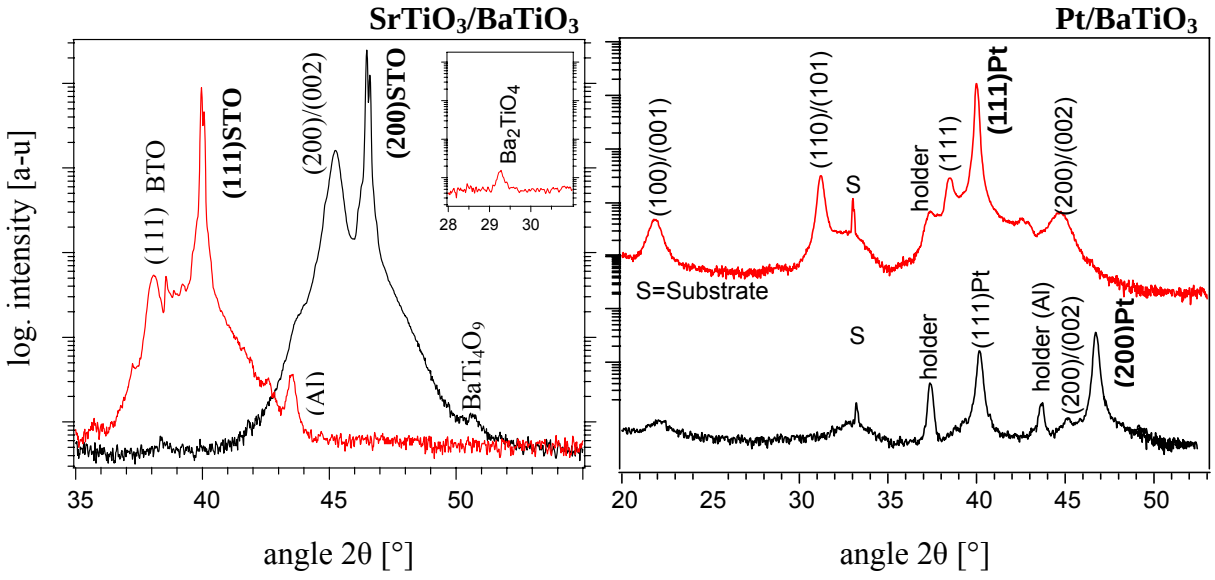

Figure 3.1.1.7: XRD patterns of $BaTiO_3$:Nb thin films deposited onto single crystals of $SrTiO_3$:Nb and polycrystalline Pt for different orientations. BTO films are highly oriented with respect to STO orientations whereas thin films deposited onto Pt do not show any preferential orientations as expected for polycrystalline substrates. As shown in the inset, small amount of Ba_2TiO_4 and $BaTi_4O_{12}$ extra phases are observed for STO substrate. No extra peak has been found for Pt substrates.

Thin films deposited onto STO are well oriented with respect to the substrate whereas polycrystalline Pt does not induce any preferential orientation. We stress that discussion about the orientation effect on the electronic levels will be more explicit for the textured thin films. The different core-levels and valence band emissions are shown in Fig. 3.1.1.8. Different valence band maximum values are observed. As shown previously, STO:Nb substrate induces higher Fermi level than Pt substrate when identically oriented. The corresponding shift is seen as well in all the core levels but the shift occurs only in the second barium components for STO:Nb substrates. As already mentioned this second barium component located at higher binding energy stems from Ba ions situated at the film surface and these are sensitive to the $SrTiO_3$:Nb substrate orientation while the bulk Ba1 located at lower binding energy are not. Clear oxygen shoulders are observed for (111) orientations. The more pronounced the oxygen shoulder is the weaker the second barium component (Ba2) is. The tendencies of the spectra demonstrate a dependence of the core levels emissions on substrate orientation. This is particularly visible on textured thin films obtained with STO:Nb substrate.

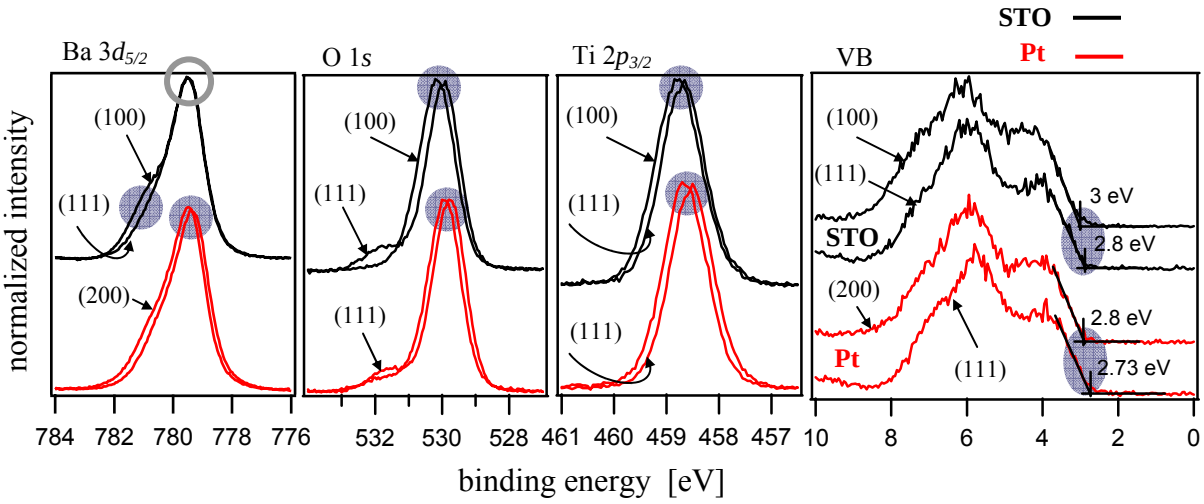

Figure 3.1.1.8: Ba3$d_{5/2}$, O 1s, Ti 2$p_{3/2}$, and VB emissions for $BaTiO_3$:Nb thin films deposited onto $SrTiO_3$:Nb single crystal (111) and (100) oriented (black curves) and polycrystalline Pt (111) and (200) oriented (red curves). The amplitude of the spectra have been normalized to reveal the change in line shape and binding energy. Oxygen shoulder is evident for samples (111) oriented.

Since surface chemistry variations from one film to the other may change the valence band as well as core-levels, the surface stoichiometry was determined. Table 1 indicates the cationic ratio (Ti/Ba) extracted from the XPS lines of figure 3.1.1.8. For fully disoriented films, the cationic ratio remains unchanged independently of the Pt orientation and a clear Ba-excess is observed as shown in the previous paragraph. However, Ba-excess and Ti-excess are

respectively found for (111) and (100) $SrTiO_3$:Nb orientations. In both cases, the surface Ba2 component is observed but its intensity is higher for (100) oriented films which have strong Ti excess. The oxygen shoulder shows exactly the reverse trend, being smaller for Ti-excess (111) films. In good agreement with the XRD patterns, Ti excess is derived from XPS calculation when a Ti-rich phases is detected as well as Ba excess can be observed when Ba-rich phases are found. However, whatever the cationic excess (Ba or Ti), the splitting between the two Ba components is still visible. No extra-phases were found for sputtered thin films onto Pt but an amorphous phase can not be ruled out.

Table 1 – Surface stoichiometry composition (**Ti/Ba**)

orientation	STO substrate	Pt substrate
(111)	0.77	0.8
(h00)	1.21	0.8

Since the link between Ba2 and O shoulder components and the surface stoichiometry is ambiguous, we look in the next part for possible influence of the crystallographic orientation. To clarify the crystallographic influence on the core levels in Nb doped titanates, we have measured the surface properties of Nb-doped STO single crystal for (100), (110), and (111) orientations. It would also be nice to perform similar experiments on Nb-doped BTO single crystals differently oriented but such samples are not easily available. We will thus investigate here the oxygen shoulder as a function of crystallographic orientation in $SrTiO_3$:Nb crystals.

3.1.1.4 Surface properties of Nb-doped $SrTiO_3$ single crystals

a) Different crystallographic orientations

XRD patterns of Nb-doped STO single crystals with (100), (110) and (111) orientations are shown in Fig.3.1.1.9. These samples were introduced in the vacuum system and annealed to a moderate temperature (400°C, 0.05 Pa in oxygen, 1h00) prior to the measurement to remove the usual hydrocarbon contaminations from the surfaces.

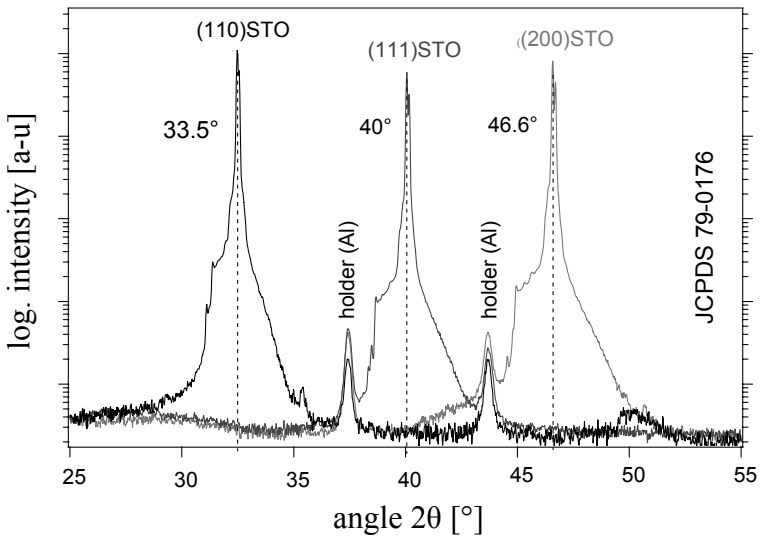

Figure 3.1.1.9: X-ray diffraction pattern of typical Nb-doped $SrTiO_3$ single crystal used as substrate, with (100), (110), and (111) orientations.

The O 1*s* core levels for these 3 different orientations are presented in Fig. 3.1.1.10. The spectra were normalized to underline the shape differences. It is clear that different orientations induce different oxygen shoulder intensities with respect to the main O component. In contrast, the valence band maximum (VBM) values remain unchanged for all the crystals which shows that the free electrons energy levels do not depend on the crystal orientation

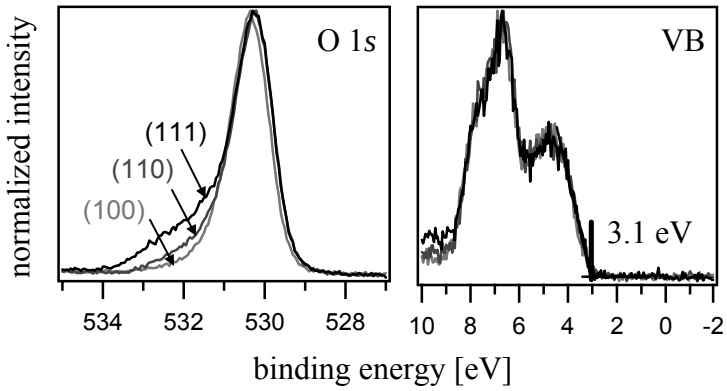

Figure 3.1.1.10: O 1*s* and valence band for Nb-doped $SrTiO_3$ single crystals for (111), (110), and (100) orientations. The spectra have been normalized to their maximum intensities. The Fermi level is independent of crystallographic orientations but the oxygen shoulder is obviously higher for polar orientations.

Cubic $SrTiO_3$ perovskite is paraelectric in broad range of temperature especially in our operating measurement (T_{room}). There is thus no bulk ferroelectric polarisation that would support the anisotropic shape of the oxygen shoulder. However, Noguera [4] has shown that the topmost surface of $SrTiO_3$ includes polar terminations and is thus highly unstable.

For instance, along [110] and [111], the surface terminations are polar. As shown on figure 3.1.1.11, the (111) surface plane is made of $SrO3^{4-}$. However, Along [100], if formal charges are assumed (Sr^{2+}, Ti^{4+}, and O^{2-}), both SrO and TiO_2 terminations are neutral. Even, without

using these formal charges, $SrTiO_3$(100) and $BaTiO_3$(100) have been referred as *weakly polar* surfaces [5]. The (111) and (100) top lattice plane have thus very different polar states.

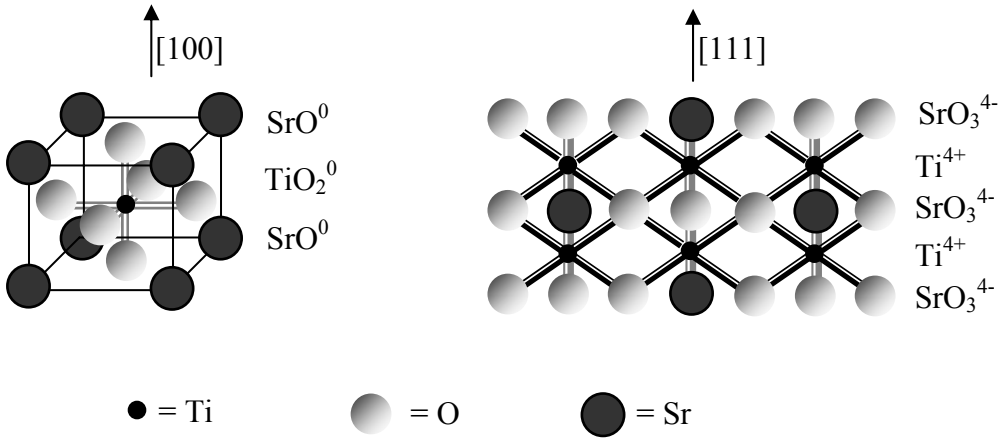

Figure 3.1.1.11: Structural representations of $SrTiO_3$ in the cubic state. The (100) direction is indicated in the left, while the (111) directions SrO_3-terminated, is showed on the right side

As a consequence, the oxygen shoulders observed in the O levels in $BaTiO_3$:Nb thin films of different orientations may well be attributed to the same changes of surface polar state for different crystal orientations. However, the comparison between $SrTiO_3$:Nb single crystals and $BaTiO_3$:Nb oriented films is limited. Even strongly textured, films are always made of grains (or columns) and this microstructure undermined one to one correspondence with bulk single crystals. Since the possible chemical segregation at the film surface was not 100% ruled out in the former paragraph, we will now check the surface chemistry of $SrTiO_3$:Nb doped single crystals.

b) Different niobium concentrations

As mentioned above, Nb-doped STO single crystals are largely used as bottom electrode for thin films processing while keeping reasonable lattice matching with for example $BaTiO_3$ films. However, we have not succeeded to measure the resistance of the $SrTiO_3$:Nb crystals using mechanical contact with conventional multimeter tips suggesting a rather insulating surface layer.

We have thus studied the surface properties of $SrTiO_3$ single crystal with different Nb concentrations 0.05 wt% and 0.5 wt% corresponding respectively with a doping level of $1.7 \cdot 10^{19} cm^{-3}$ and $1.7 \cdot 10^{20} cm^{-3}$. These concentrations are those given by the provider (Crystec)

and Nb emission is clearly observed for the 0.5 wt% concentration as showed Fig. 3.1.1.12 while it is in the noise for 0.05 wt% (weight percent).

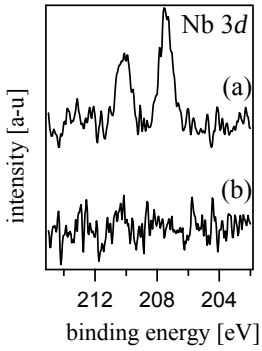

Figure 3.1.1.12: Nb 3*d* core levels for Nb-doped $SrTiO_3$ single crystals with 0.05 wt% (a) and 0.5 wt% (b) niobium concentrations. No niobium could be detected for (b). A Nb concentration of 0.8 wt% has been derived from the peak intensity in good agreement with the nominal Nb content given by the provider.

Ideal Fermi level position for oxide electrode is shown in Fig. 3.1.1.13 (a) in which E_F is located in the conduction band. This behaviour is often named as a degenerate state [6] and is suitable to provide sufficient charge carrier density for good electrical contact. However, we do not observe such Fermi level position even by increasing the doping concentration (Fig 3.1.1.13 b).

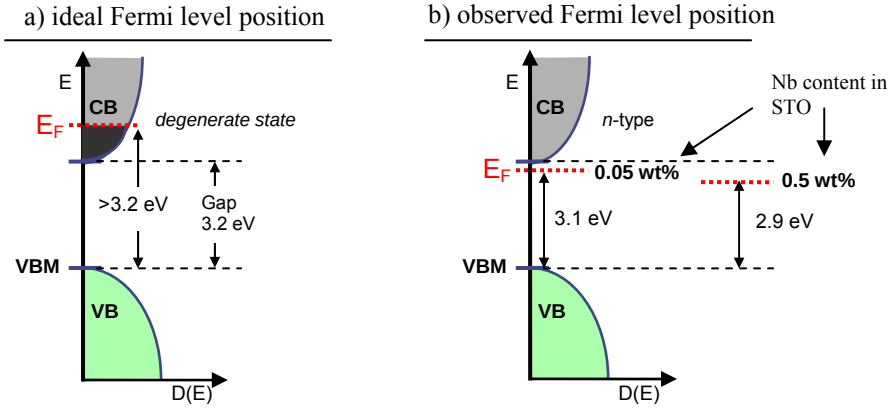

Figure 3.1.1.13: Schematic energy band diagram illustrating a) an ideal Fermi energy position for suitable electrode material. E_F should be located above the minimum of the conduction band to provide sufficient charge carrier density. Instead, E_F is measured below the conduction band level in b).

The measured VBM are respectively 3.1eV and 2.9eV for 0.05 wt% and 0.5 wt% doping concentrations. They do probably not represent the Fermi level position in the bulk but in the high doping limit, the Fermi level position at the interface should approach the Fermi level in the bulk. Instead, we observe a decreasing of E_F with increasing the Nb concentration. In this context, different takeoff angle of measurements were used to elucidate if any chemical

change could be observed between low and high angles, i.e., surface and bulk sensitive. The cationic ratio Sr/Ti is shown in Fig. 3.1.1.14 with different takeoff angles

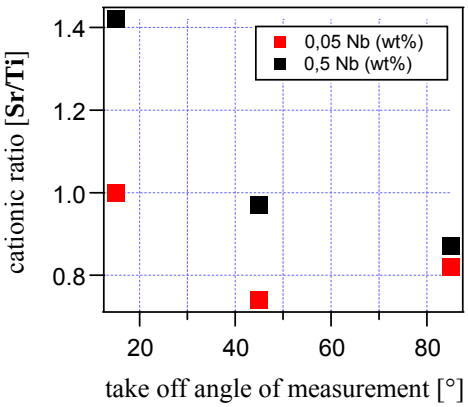

Figure 3.1.1.14: surface stoichiometry of single crystal of Nb-doped $SrTiO_3$ with 0.5 and 0.05 wt% niobium concentration. A clear Sr enrichment is observed at the near-surface region (low angle). Obviously, Sr enrichment is more pronounced for higher doping content. This might be a possible explanation for the low Fermi energy position observed in such a system.

A clear Sr enrichment is observed at low angle when the geometrical configuration is surface sensitive. This might be explained by two possible explanations:

- This surface Sr enrichment may follow from the Nb^{5+} substitution to Ti^{4+} leading to Sr^{2+} vacancies formation for charge neutrality. The expelled Sr could thus be accumulated at the surfaces of Nb-doped $SrTiO_3$ single crystal. We however have no direct evidence of Sr vacancies formation in the bulk but they have been suggested in the literature [7,8]. Obviously Sr-enrichment is much more pronounced for higher doping concentrations. We did not observe any change in the O emissions for both niobium concentrations at a given takeoff angle. The observed oxygen shoulder (discussed above) is thus not related with doping effect.

- At single crystal surfaces, the photoelectron diffraction might lead to an oscillating intensity when the emission angle is modified. For certain excitation energies and emission angles, the intensity can also strongly depend on the azimuthal orientation of the crystal, i.e. when the sample is rotated along its surface normal. Thus it might be induces by anisotropic effect. Similar effect has been observed in $SrTiO_3$ single crystal in the Sr 3*p* levels [9].

3.1.1.5 Summary

We can summarize the results of this first sub-section as following:

- Varying the target to substrate distance does not induce significant changes in the microstructure but affect considerably the Fermi level position as well as surface stoichiometry. If thin films are sputtered with high oxygen content, Ba-rich phases are formed in good agreement with the surface stoichiometry calculation.
- Nb-doped BTO thin films have higher Fermi level than undoped samples, which can, however, only be observed on Pt substrates. Their surfaces are Ba-rich (10─20%) whereas pure BTO exhibit typical Ti-excess (10─20%) of excess which can be reduced by increasing the oxygen partial pressure and the target to substrate distance.
- When identically prepared samples are deposited onto polycrystalline Pt and single crystal of $SrTiO_3$:Nb, we observed higher Fermi level for STO:Nb/BTO system. This is related to the different energy band alignment of the BTO film with the Pt and STO, respectively.
- Different substrate orientations of STO:Nb affect the Ba and O emissions of sputtered $BaTiO_3$. With [111] texture, the oxygen asymmetry is much more pronounced whereas (100) orientation induces higher Ba2 component (located at higher binding energy).
- For Nb-doped single crystals, the electronic level of O is also modified under different crystal orientations. The higher is the surface polar character, the stronger is the O shoulder. Therefore a correlation between the polarity of the surface and the surface core-level features is raised.
- Important Sr-enrichment has been found at the near-surface region of $SrTiO_3$:Nb single crystals. The Sr excess is higher when increasing doping concentrations. No change was observed in the oxygen levels at different Nb concentrations excluding a correlation with the previous point and the observed Sr excess. The observed Sr excess at the near surface region might explain by doping or anisotropic effect du to small angle of measurement.

3.1.2 Interface formation of $BaTiO_3$ materials with top electrode

In this sub-section, photoemission studies of $BaTiO_3$ surfaces upon metal deposition are presented. Thin films of BTO as well as Pt were sputtered with in-situ thermal substrate preparation. During metal deposition a partial reduction of Ti occurs and a Schottky barrier for electrons of ~0.6 eV is found.

Ceramics of Nb-doped $BaTiO_3$ have also been investigated with metal contact formation. Identical Schottky barrier height is found regarding intrinsic BTO, but a band bending regime occurs for Nb-doped BTO. The bending is assumed to be a direct consequence of doping effect inducing charge depletion at metal/BTO interface. Finally, the metal contact formation with Pt deposition is compared to indium deposition. For the latter, a negligible barrier height has been found corresponding to an ohmic contact. Therefore, the contact nature has been directly probed with the help of XPS, confirming previous electrical experiments which showed that In is a good ohmic contact for *n*-type $BaTiO_3$.

3.1.2.1 $BaTiO_3$/Pt interface formation

Photoelectron spectra have been recorded during deposition of Pt onto $BaTiO_3$ thin films. BTO was deposited with a thickness of ~100nm onto SiO_2/TiO_2/Pt coated Si wafer at the beginning of the experiment using the deposition conditions described in the previous section. With increasing Pt thickness the substrate core levels are gradually attenuated and the Pt emissions increase. All substrate emissions decay exponentially with decay constants corresponding to the inelastic electron mean free path of the individual lines as shown in Fig. 3.1.2.1. This shows that the Pt deposition is a layer by layer one.

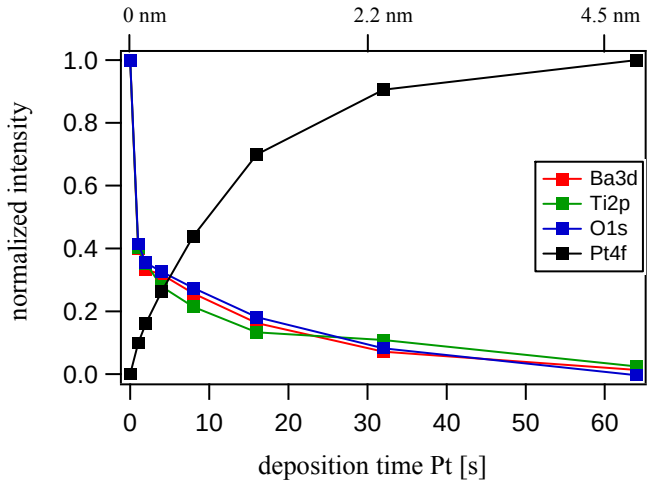

Figure 3.1.2.1: Attenuation of the substrate core levels and increasing of the Pt peak intensity. All the emissions change exponentially indicating a layer by layer growth mode of Pt onto BTO.

To determine the Schottky barrier height of the $BaTiO_3$/Pt interface, Pt is stepwise deposited onto freshly sputtered BTO. After each deposition step, a full set of photoelectron spectra is recorded. Since the sample transfer from the deposition chamber to the analysis chamber takes only few minutes, surface contaminations are avoided during the entire experiment. Figure 3.1.2.2 shows the valence band emissions of the BTO sample used for the experiment as well as Pt valence band spectra in which a sharp Fermi edge is found at 0 eV as expected for metallic Pt [10].

Figure 3.1.2.2: X-ray valence band emission recorded from sputtered $BaTiO_3$ thin film and the same film covered with Pt layer of 4.5 nm. The determination and position of the valence band maxima is indicated for BTO thin film.

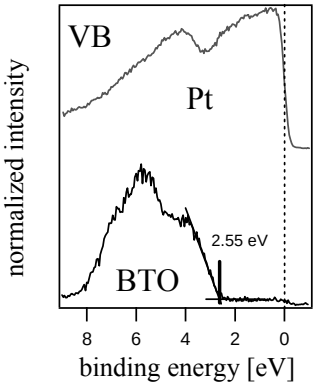

To show the gradual evolution between these two extreme cases, photoelectron spectra recorded during deposition of Pt on $BaTiO_3$ are shown in Fig. 3.1.2.3. The Pt thickness is indicated in the graph in nm. The black emissions are derived from uncovered BTO thin films, which are gradually attenuated in the course of the Pt deposition. Consequently the Pt 4*f* emission increases. Only a single Pt doublet is found with asymmetric shape and binding energy of 71.0 eV typical for metallic platinum [10]. After deposition of 4.5 nm of Pt, the Ba $3d_{5/2}$, Ti 2*p*, O 1*s* lines are completely attenuated. Except for a small shoulder at the low binding energy side of Ti 2*p* and the high binding energy side of O 1*s*, no significant change of the line shapes and half widths of the substrate emissions are observed during Pt deposition. This indicates a largely non-reactive interface. At low coverage, the Pt 4*f* emission has binding energies of up to 71.9 eV, which is considerably higher than for the thick Pt film (71.0 eV). Such behaviour is frequently explained by incomplete screening of the core hole in small islands [11] and is in good agreement with similar experiment performed with BST/Pt [12]. There are noticeable changes in the Ba 3*d* line shape during the experiment. The spectrum of uncovered BTO thin film exhibits the known Ba2 structure with a high binding energy surface component as described in the previous section [13-15]. The energy separation between both components decreases in the course of the Pt deposition as already observed during BST/Pt interface formation [12,16]. The Ba 3*d* change will be largely discussed later

in the section III.3.4 and is thus not described in the present section. It is assumed that this change does not induce any active contribution to the Schottky barrier height since it is rather an intrinsic property of the surfaces of $BaTiO_3$.

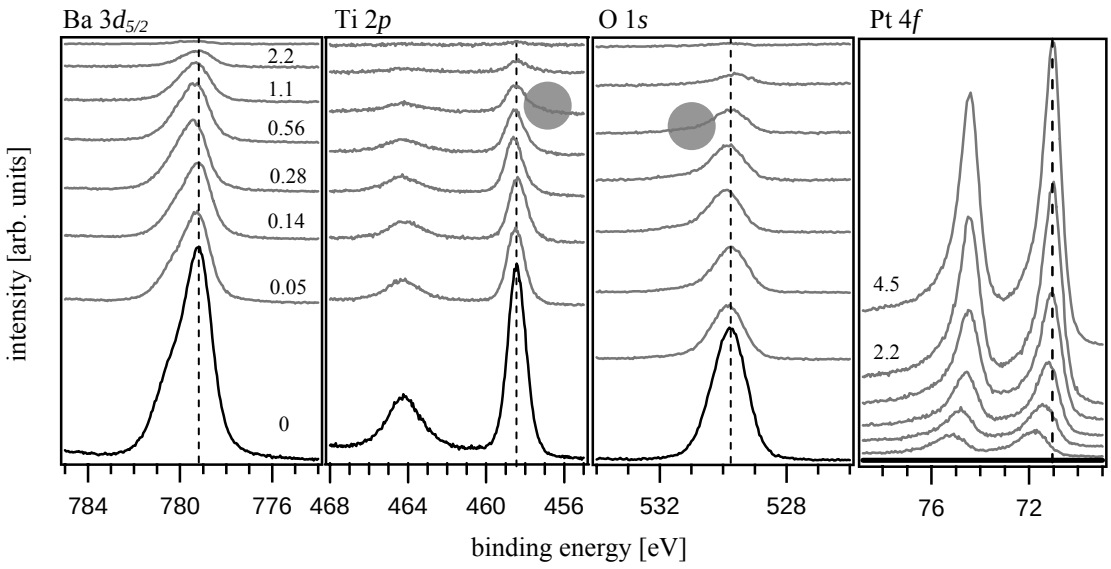

Figure 3.1.2.3: X-ray photoelectron spectra of a $BaTiO_3$ thin film surface in the course of Pt deposition. The Pt thickness is indicated in nm. All spectra were referenced to pure metallic Pt surface layer. The gray circles are highlighting the extra components in the Ti and O levels due to Pt deposition as discussed in the text.

As evidenced by the gray circles in Fig. 3.1.2.3, the Ti 2*p* and O 1*s* exhibit asymmetric emissions when BTO is covered by Pt. This behaviour is going to be described now and is better evidenced below in Fig. 3.1.2.4 using normalization and shift in energy of the spectra.

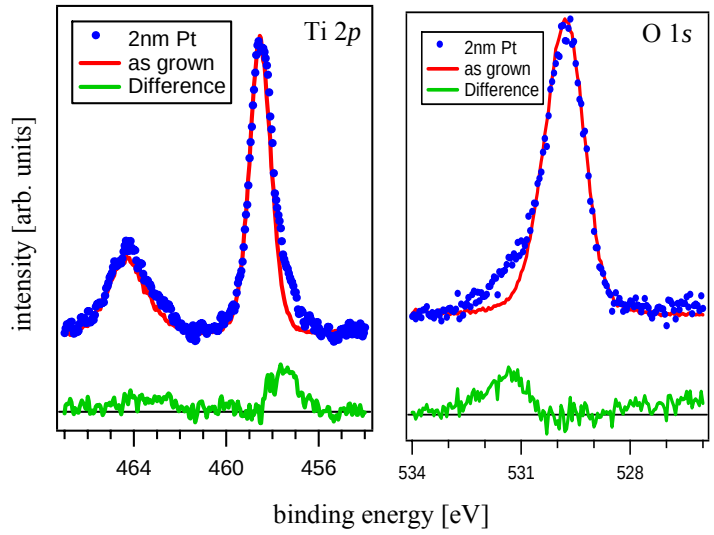

Figure 3.1.2.4: Ti 2*p* spectra for uncovered BTO surface (red) and covered with 2nm of Pt (blue). The spectra are normalized in intensities and shifted in energy to underline the shape change. Pt deposition induces asymmetric emissions for both core levels

The Ti 2*p* spectra of uncovered BTO show symmetric emission whereas Pt deposition induce small component at lower binding energy. This can be attributed to the presence of Ti^{3+} states [12,17] according to previous experiments. Simultaneously, the O 1*s* core level shows an asymmetric shape after Pt deposition. This suggests again a correlation between Ti^{3+} occurrence and creation of oxygen vacancies. The change in the Ti level is in good agreement with Schafranek *et al.*[12] but these authors did not observe asymmetric O core levels in the course of Pt deposition.

To confirm the occurrence of such defects, thermal oxidation and reduction treatments were performed in situ after 2 nm of Pt deposition. X-ray photoelectron spectra of BTO/Pt interface after different preparation steps are shown in Fig. 3.1.2.5.

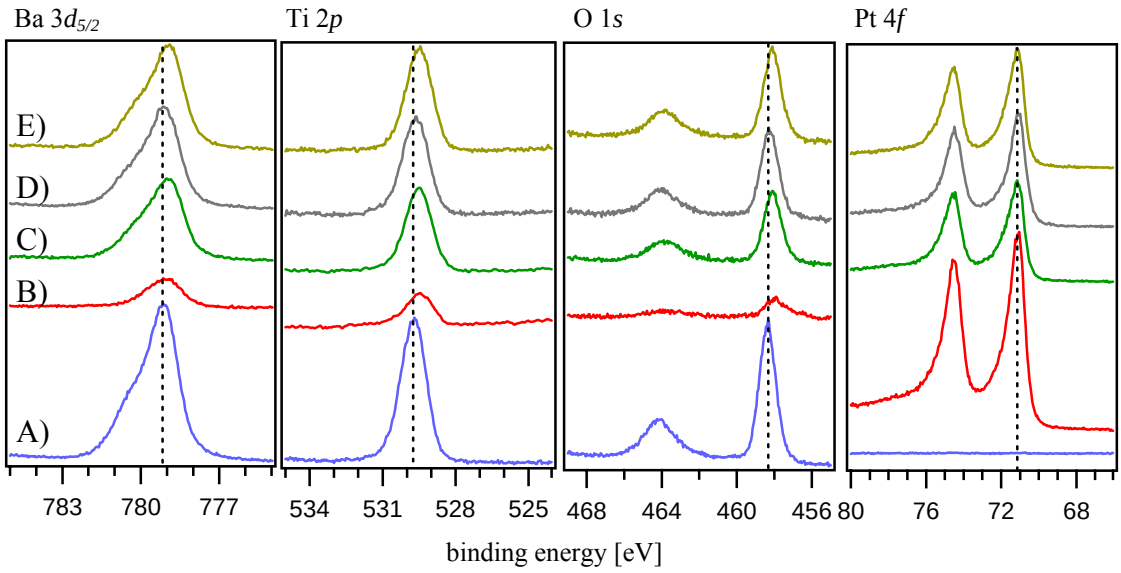

Figure 3.1.2.5: Photoelectron core level for (A) uncovered BTO deposition of ~100nm, (B) Pt deposition of ~2nm, (C) annealing in 0.05 Pa oxygen at 450°C for 30min, (D) annealing in ultra high vacuum (10^{-5} Pa) at 450°C for 30 min, and (E) second oxygen annealing using the conditions of (C).

As previously described, the Ba $3d_{5/2}$, Ti 2*p*, and O 1*s* emissions are attenuated after Pt deposition whereas the Pt 4*f* is clearly observable. However, the BTO emission lines are strongly increased in intensity and the intensity of Pt 4*f* level is decreased after annealing in good agreement with previous experiments [12]. This is explained by the formation of three-dimensional islands of the 2nm Pt film after thermal treatment [18-20]. The substrate intensities increase again slightly after the second heating in vacuum (reducing). The oxidizing thermal treatment also induces a shift of all BTO core levels to lower binding energy, while the binding energies are increased after the reducing treatment. The shifts are

evidenced by the dashed lines in Fig. 3.1.2.5. The shifts are clearly related with change in the Schottky barrier due to oxidation step (discussed later).

By superimposing the Ti 2*p* and O 1*s* core levels between Pt deposition step and oxygen annealing step, it becomes clear that the extra components observed in both levels disappear after oxygen annealing as sketched in Fig. 3.1.2.6.

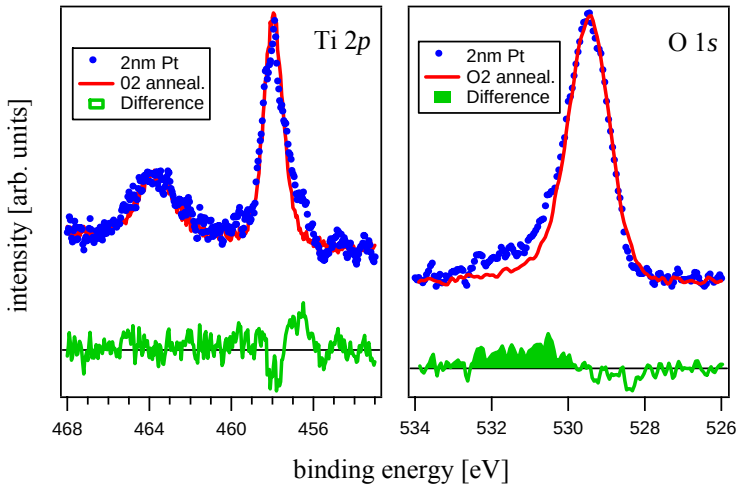

Figure 3.1.2.6: Ti 2*p* and O *1s spectra* after Pt deposition (blue) and oxidation treatment (red). The extra component located at lower binding energy is removed after oxygen annealing confirming Ti^{3+} states after Pt deposition. The same behaviour is observed for the O 1s core level.

Therefore, Pt deposition leads to the formation of oxygen vacancies as indicated from the occurrence of asymmetric XPS spectra from the Ti 2*p* levels. The asymmetric O level seems to confirm this assumption. The vacancy formation is attributed to chemical interaction with the Pt layer [12]. The oxygen vacancies are removed after oxygen annealing as confirmed by the symmetric O 1*s* and Ti 2*p* features. Additional reducing thermal treatment does not re-establish Ti^{3+} states and extra oxygen shoulder.

The evolution of substrate core level binding energies in the course of deposition is displayed in Figure 3.1.2.7. Core level to valence band maximum binding energy differences are subtracted for better comparison. The values are derived from the spectra in Fig. 3.1.2.3.

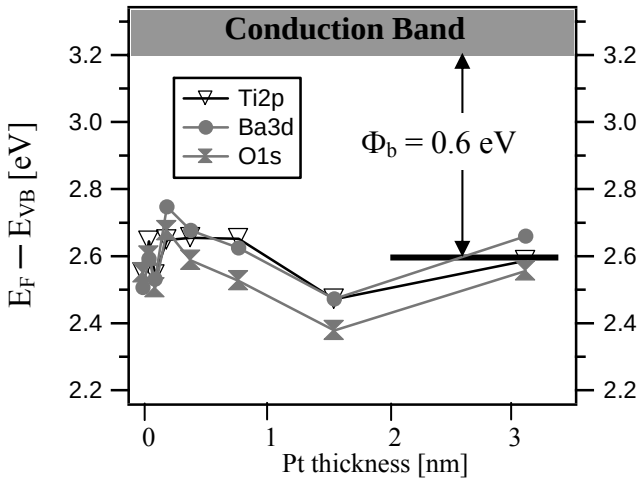

Figure 3.1.2.7: Evolution of BTO core levels binding energy with increasing film thickness for deposition of Pt onto BTO. A Schottky barrier of 0.6 eV is extracted from the present plot.

No large shifts occur during Pt deposition but the remaining small shifts of all BTO core level are parallel. This also indicates the absence of strong interface reaction. For the thick Pt layer, the binding energies correspond to a valence band maximum of *BE* (VB) = 2.6 eV. Together with the band gap of 3.2 eV, this corresponds to a Schottky barrier for electrons of 0.6 eV in good agreement with values reported in the literature [12,13]. In addition, this Schottky barrier height is increased to 0.8 eV after oxidation treatment as concluded by the core-level shifts observed in Fig. 3.1.2.5 after oxidation treatment.

To briefly summarize this section, the interface formation of BTO/Pt has been investigated. No strong chemical reactions were found. However, Pt deposition induces the occurrence of oxygen vacancies leading to Ti^{3+} states which can be removed by oxygen thermal treatment. This induces direct consequences on the Schottky barrier height which is thus increased to 0.8 eV after oxidation treatment, in good agreement with similar experiment on BST [12].

The next section will deal with the contact formation of Pt onto Nb-doped BTO in order to study the doping influence on the interface properties.

3.1.2.2 Nb-doped $BaTiO_3$/Pt

We have studied the interface formation of Nb-doped $BaTiO_3$ ceramics with a niobium concentration of 0.2 wt%. This concentration corresponds to a semiconducting character as described in section I.2.1. The *n*-type behaviour is well confirmed by the valence band emission recorded for the Nb-doped ceramic shown in Fig. 3.1.2.8, which exhibits a valence band maximum of 3.13 eV as expected from *n*-type $ATiO_3$ compounds [22,23] and already shown on section III.1. The experimental approach to study the interface formation with Pt deposition is similar than previously, i.e. using stepwise deposition steps.

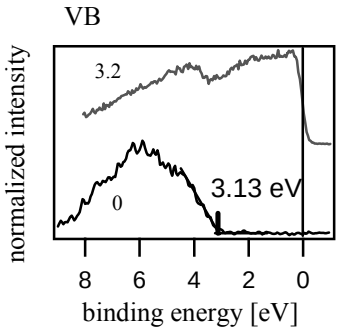

Figure 3.1.2.8: X-ray valence spectra of uncovered Nb-doped $BaTiO_3$ ceramic and covered with deposition a Pt ~3.2nm thick.

X-ray photoelectron spectra of a Nb-doped $BaTiO_3$ ceramic recovered by Pt deposition are shown in Fig. 3.1.2.9.

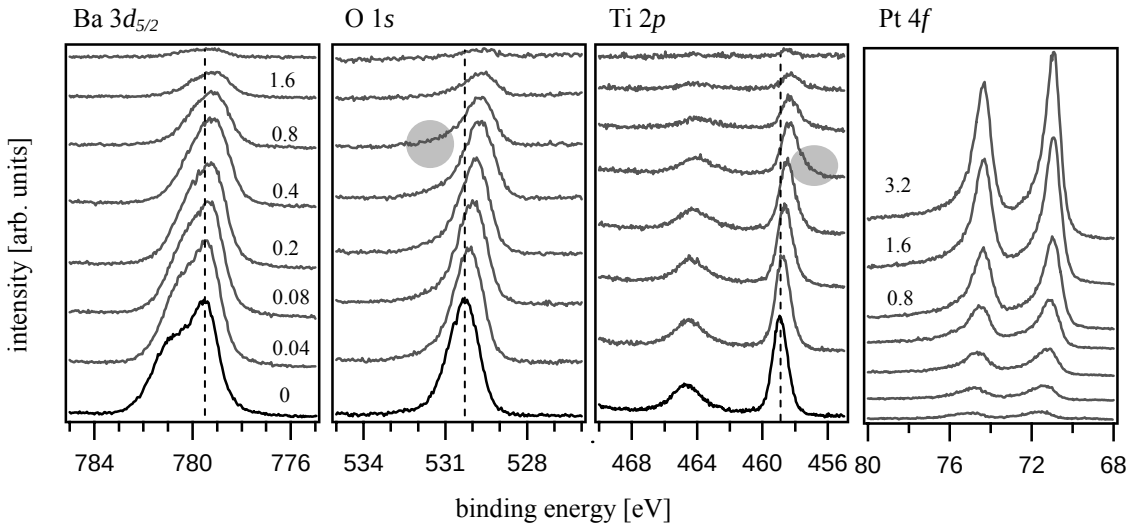

Figure 3.1.2.9: XPS spectra of a BTO:Nb ceramic in the course of Pt deposition. The indicated numbers correspond to Pt thickness. The black spectra are related to the uncovered surface. The dashed lines indicate the initial binding energy position prior to the Pt deposition and can be used as a reference to reveal the shift induces by the covering.

Obviously, Pt deposition induces a shift of the BTO:Nb core levels to lower binding energies, corresponding to a band bending . As in the case of undoped BTO thin film shown in the previous section, Pt deposition induces Ti^{3+} states and an oxygen shoulder as evidenced by the gray circles. Therefore, this effect seems also to occur for bulk materials. The evolution of the binding energies of the substrate core-levels in the course of increasing metal film thickness are shown in Fig. 3.1.2.10. The gray points correspond to undoped BTO and are derived from the experiment shown in Fig. 3.1.2.7. The blue dots are related to the Nb-doped BTO and are derived from Fig. 3.1.2.9. By subtracting suitable offsets from the core-level binding energies, we clearly see a decrease of the Nb-doped BTO core levels to finally reach those of undoped BTO at higher Pt thickness. The "saturation" value observed in both samples is ~2.6eV. Together with the band gap value of 3.2eV, this corresponds again to a Schottky barrier of ~0.6eV for undoped thin film and Nb-doped ceramic. However, the difference in the valence band maximum values between both uncovered samples leads to different energy band diagrams of intrinsic $BaTiO_3$ and Nb-doped $BaTiO_3$ as schematized in Fig. 3.1.2.11.

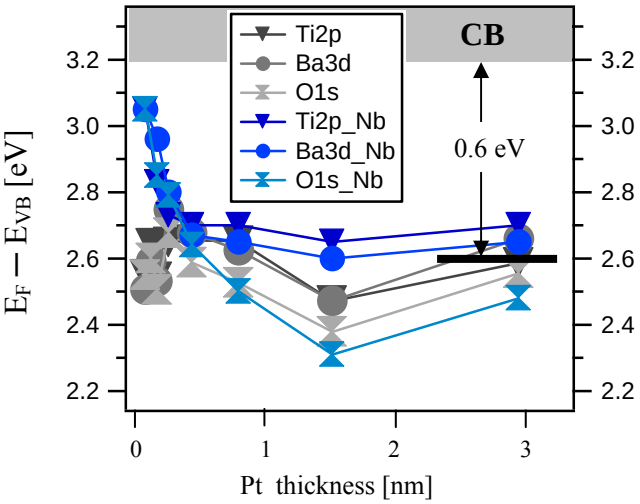

Figure 3.1.2.10: Evolution of core-level binding energies in dependence on deposition time of Pt on undoped BTO thin film and Nb-doped BTO ceramic. The binding energies are referenced to the position of the valence band maximum of the BTO and Nb-doped BTO by substracting corresponding offset values.

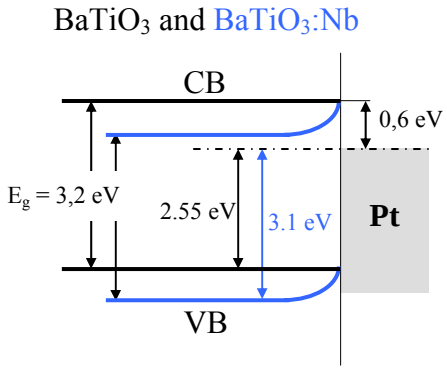

Figure 3.1.2.11: Experimentally determined energy band diagrams for $BaTiO_3$/Pt and $BaTiO_3$:Nb/Pt. The undoped film exhibits a flat band regime whereas a band banding appears at the interface with Nb doping. The barrier height in both cases is 0,6 eV.

Therefore, deposition of Pt onto intrinsic BTO does not induce a band bending as the Fermi level position in the bulk and at the interface are identical, whereas deposition of Pt onto Nb-doped BTO induces a band bending due to higher Fermi level in the doped substrate. This result is in a very good agreement with the typical semiconducting character encountered at low donor concentrations in $BaTiO_3$ as described in section I.2.1. Indeed, when suitably selected, a small amount of donor dopants (e.g. few ppm of Nb, La, Sm…) is able to induce a macroscopic increase of conductivity [24] because of energy levels located relatively close to the conduction band. As in any conventional n-type semiconductor, an upward band bending causes depletion of conduction electrons thus leaving the charged donor states uncompensated, which induces a space charge region. The space charge is provided by the ionized Nb_{Ti} donors. The present result show direct evidence for such a space charge at the BTO:Nb/Pt interface. The present XPS investigation is thus a microscopic confirmation of a well known behaviour of $BaTiO_3$:Nb ceramics.

We have seen the contact properties at the interface between $BaTiO_3$ and noble metal such as Pt. A clear non-ohmic contact (rectifying contact) has been evidenced with a Schottky barrier height of ~0.6 eV independent on substrate doping and microstructure (films or ceramics). Functional materials based on barium titanate can have their properties subsequently modified by changing the metal used as electrode. For instance, in multilayered ceramic devices, it is well known that noble metals such as Au, Pt, and Pd are not suitable as an internal electrode

for PTCR ceramics (see section I.2.1) due to the non-ohmic nature of the interface as in the previous paragraph. This rectifying contact is indeed equivalent to high resistivity contact which overcomes the sample resisitivity by several orders of magnitude [16]. Flaschen and Van Uitert [26] made a low-resistance ohmic contact to ferrite and semiconducting titanate ceramics with indium-gallium on the surface to avoid such a screening. Voltage-current relation has been used to define the ohmic contact nature. Nowadays, indium-gallium alloy is largely used [27,28] to ensure ohmic contacts to semiconducting ceramics. However, if it is well established that metals with large oxygen affinity yield ohmic contact [29] (e.g. In, Zn, Fe, Sn, Ni, and Cd) no direct experimental proof was given to probe such a junction. Therefore, the next section will show that semiconducting Nb-doped $BaTiO_3$ ceramic covered with In exhibit a negligible Schottky barrier for electrons.

3.1.2.3 Ohmic and non-ohmic contact with In and Pt top electrodes

In this study, indium was evaporated from a temperature controlled effusion cell using an Al_2O_3 crucible. The vacuum during metal deposition was below 10^{-6} Pa in order to minimize In oxidation by residual oxygen. The same ceramic of Nb-doped $BaTiO_3$ as used for the Pt deposition was used in the present experiment using the uncovered face. The ceramic was held at room temperature during In growth. Figure 3.1.2.12 shows X-ray photoelectron spectra of O 1*s*, and In 3*d* core levels during In deposition. Pt deposition is also reported to address a comparison between both kind of metal. In contrast to Pt deposition, indium does not induce any binding energy shift of the BTO emissions. Ba and Ti levels are not reported here since they behave like the O 1*s* level. This indicates a largely non-reactive interface. In 3*d* core-level emission line a small shoulder develops on the high binding energy side, as indicated by arrows in Figure 3.1.2.12 and better evidenced in Fig. 3.1.2.13. This shoulder disappears at higher coverage to induce almost symmetric core-level line in good agreement with similar emission in the literature [30]. The observed shoulders can be attributed to a small amount of In_2O_3 formation. As no reduction of the substrate is evident (no Ti^{3+} observed), the small amount of In_2O_3 at the beginning of film growth might be related to reaction of In with adsorbed oxygen or with oxygen from the residual gas in the vacuum chamber. At higher coverage, this might not be observed due to superimposition with the intense and asymmetric metallic In emission.

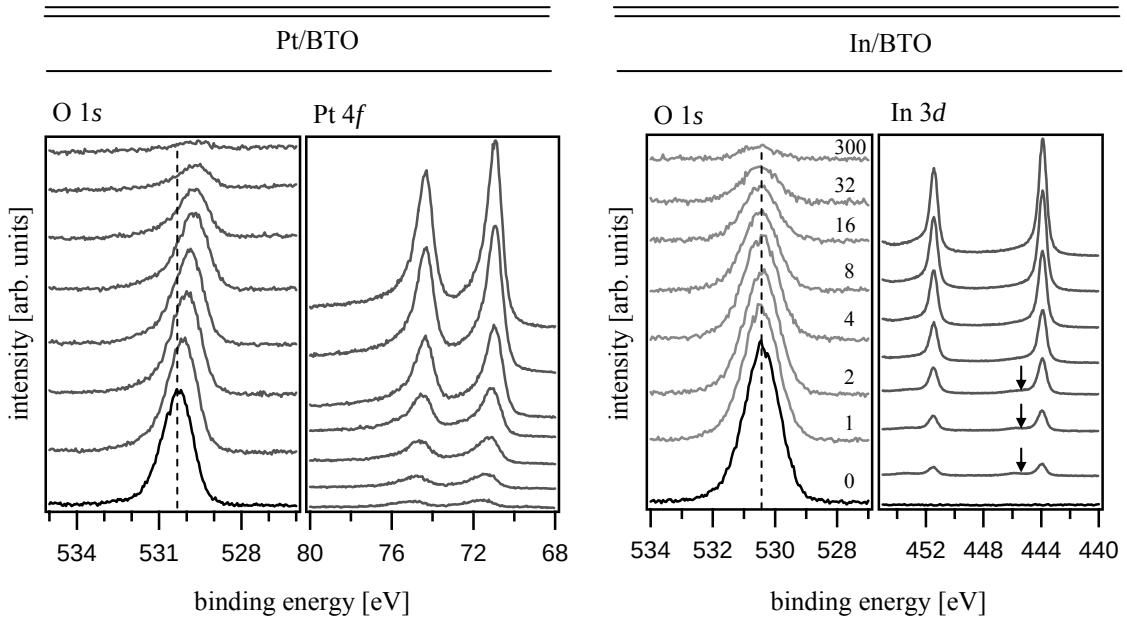

Figure 3.1.2.12: O 1*s*, Pt 4*f*, and In 3*d* core levels recorded after stepwise deposition step. The Pt thickness is indicated in nm whereas In coverage is indicated by the deposition time in min. The dashed lines denote the initial binding energy of uncovered ceramic. We note that indium deposition does not induce any binding energy shift in the course of the deposition in contrast with Pt coverage.

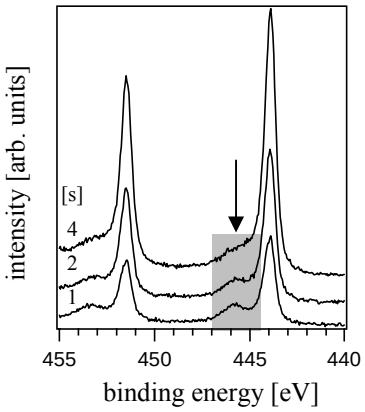

Figure 3.1.2.13: In 3*d* core-levels derived from Fig. 3.1.2.12 at very low coverage. Shoulders at higher binding energy are observable. Oxygen shoulder decreases in the course of In deposition.

By looking at the initial position denoted by the dashed line, we can observe that indium deposition does not produce any binding energy shift in the O *1s* core-level in the course of In deposition. Also no binding energy shifts are observed in the Ba 3*d* and Ti 2*p* core-levels (not shown here). This behaviour is in contrast with the shift observed under Pt deposition and gives clear evidence that In deposition on semiconducting ceramic of Nb-doped $BaTiO_3$ does not induce a band bending. Due to the high Fermi level position in doped BTO, the absence of a band bending indicates a negligible Schottky barrier height, which should give rise to ohmic

contact properties. Furthermore, no noticeable Ti^{3+} states were found after In deposition in agreement with similar experiment of Cu onto $SrTiO_3$ also giving rise to ohmic contact formation [8]. The results presented here are in excellent agreement with the literature in which the contact properties have been determined by electrical measurements [29-30].

The present work presents an insight picture of ohmic contact formation to semiconductor oxide materials using photoemission spectroscopy. The reduction of the $BaTiO_3$ by metal deposition is evident from the Ti^{3+} species with Pt deposition but no reduced species could be identified with In deposition. It was however expected that In rapidly formed In_2O_3 especially at low coverage when adsorbed in the oxide substrate giving rise to reduced species in the $BaTiO_3$:Nb. However, we did not observe such reduction in the Ti core levels. The situation is briefly summarized in Fig. 3.1.2.14 for Pt and In deposition onto Nb-doped $BaTiO_3$.

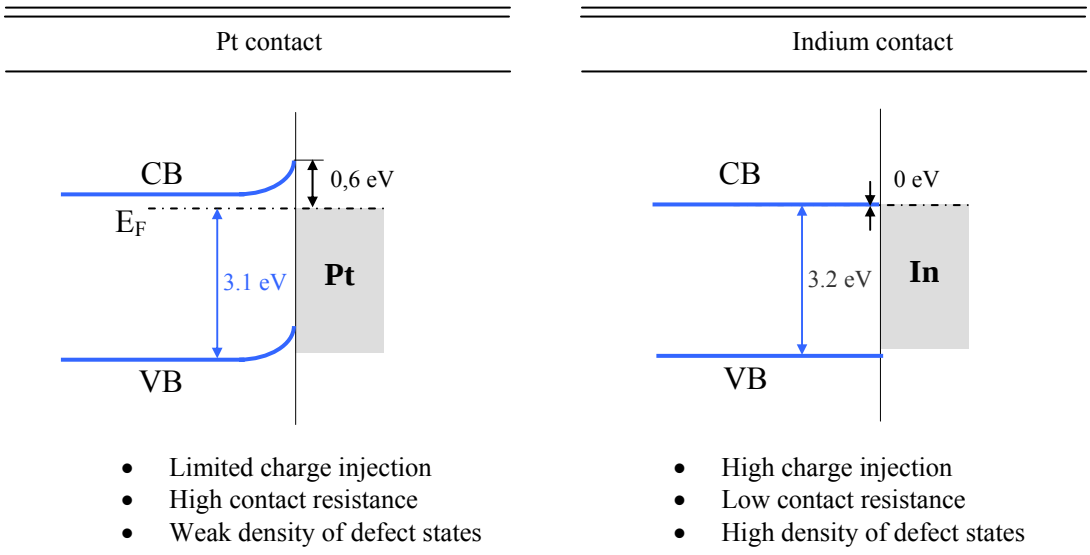

Figure 3.1.2.14: Schematized energy band diagram for Pt and In contacts with Nb-doped $BaTiO_3$. High Schottky barrier height is required to reduce the charge injection from the electrode to the oxide. However if a low interface resistance is desired, In deposition will be suitable to avoid resistance screening of the bulk ceramic.

3.1.3 Interface formation of substrate / $BaTiO_3$

This paragraph describes the interface formation of $BaTiO_3$ thin films deposited onto Nb-doped $SrTiO_3$ single crystal and platinised wafer. Thin films were identically prepared and deposited simultaneously on both substrates. We focus here on the band offset, i.e. the relative position of the energy levels on both electrodes/film interfaces. The energy band offset as well as the Schottky barrier height are investigated in situ when thin films are deposited onto bottom electrodes. These band discontinuities play indeed a fundamental role in the determination of transport properties through electrode interfaces, which are a key for the investigation of the dielectric properties.

3.1.3.1 Bottom Pt electrode / $BaTiO_3$ interface formation

BTO has been stepwise sputtered onto clean platinised Si wafer (111). Photoelectron spectra recorded during deposition of BTO onto Pt are shown Fig.3.1.3.1. With increasing BTO deposition the Pt 4*f* core level is gradually attenuated and the BTO emissions increase. Substrate emissions decay exponentially indicating a layer-by-layer growth mode of BTO onto Pt. Before each deposition, the sample was heated to 650°C during half an hour to reach a complete thermalisation. To control the deposition rate, the sample could be set in front of the target for an appropriate deposition time to obtain the desired thickness and then rotated back. After cooling, the sample was transferred to the analysis chamber for measurement. No change could be observed in the Pt 4*f* shape indicating obviously no formation of Pt-oxides [31] during BTO growth.

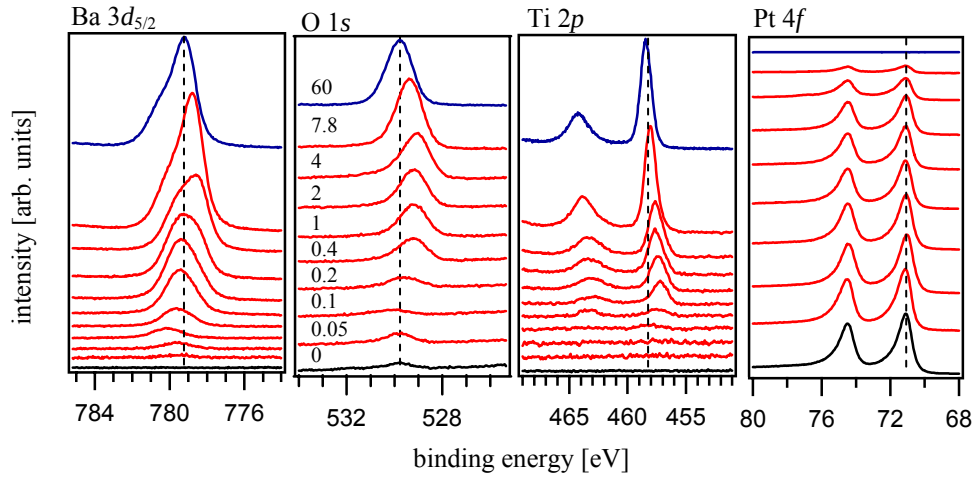

Figure 3.1.3.1: X-ray photoelectron spectra of a platinised wafer (111) in the course of $BaTiO_3$ deposition. The BTO thickness is indicated in nm. The dashed lines denote the final binding energy (BE) position.

Except for the Ba emission, no obvious changes in peak shape are observed in the O 1s, and Ti 2*p* levels indicating the absence of reduction phenomena as evident for the top interface experiment (see sub-section 3.1.2). A shift toward higher binding energies (BE) occurs in the course of BTO deposition as evidenced by the dashed line indexing the final BE position. For the uncovered state, a small oxygen emission is observed (see black spectra of O 1s level) which is explained by oxygen chemisorbed on the Pt surface after the cleaning step. The evolution of substrate core level binding energies in the course of deposition is displayed in Fig.3.1.3.2 for undoped BTO.

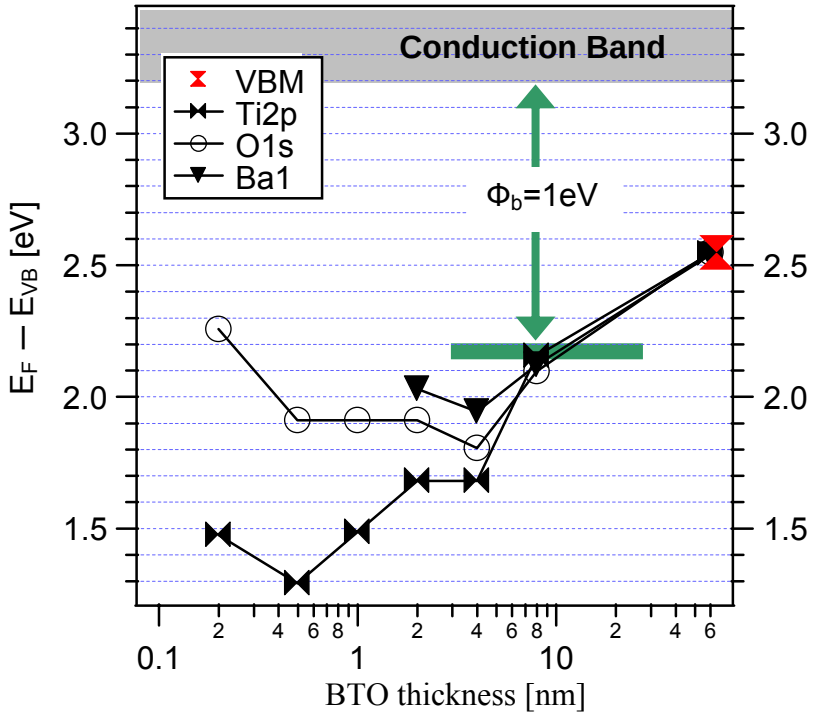

Figure 3.1.3.2: Evolution of undoped $BaTiO_3$ valence band maximum binding energy with increasing film thickness for BTO onto Pt. The arrow indicates the corresponding Schottky barrier height (Φ_b) deduced from the present graph.

By subtracting suitable offsets from the core-level binding energies, these represent the evolution of the valence band maxima (VBM) binding energy with respect to the Fermi energy. The offsets are determined after subsequent deposition of BTO (~60nm) defining the reference. Therefore VBM position from undoped (~2.55eV) is reported and used as the reference for the corresponding core-levels (Ti 2*p*, O 1s, and the main Ba component named Ba1). This procedure is convenient to observe the interface reaction occurring during the film growth and to quantify the Schottky barrier height. Obviously, all the core-levels do not exhibit parallel shift for a film thickness ≤ 10nm indicating the effect of incomplete development of the electronic structure. We also observe smaller Ti 2*p*─VBM and higher O 1*s*─VBM at very low coverage as observed in similar experiment on BST [12]. This indicates

high reactivity of the oxygen at very low coverage. The Ba1─VBM is not reported at low thickness since the Ba emission exhibit a broader peak due to the presence of two components (see Fig. 3.1.3.1). However, for the present spectrum, one can see binding energy saturation at ~10 nm thick (green line). The Schottky barrier then amounts to Φ_b = **1** ± 0.1eV when $BaTiO_3$ is deposited onto Pt. Similar experiment has been performed using Nb-doped $BaTiO_3$ target and identical Schottky barrier height was determined (not shown). Together with the previous experiments performed with Pt onto BTO and Nb-doped BTO, one can discuss the energy band diagrams for the entire stacks: Pt/BTO/Pt and Pt/BTO:Nb/Pt.

3.1.3.2 Intrinsic $BaTiO_3$ and Nb-doped $BaTiO_3$

The energy band diagrams experimentally determined are given below in Fig. 3.1.3.3. It includes the interface experiments with top and bottom contact for intrinsic and Nb-doped BTO compositions.

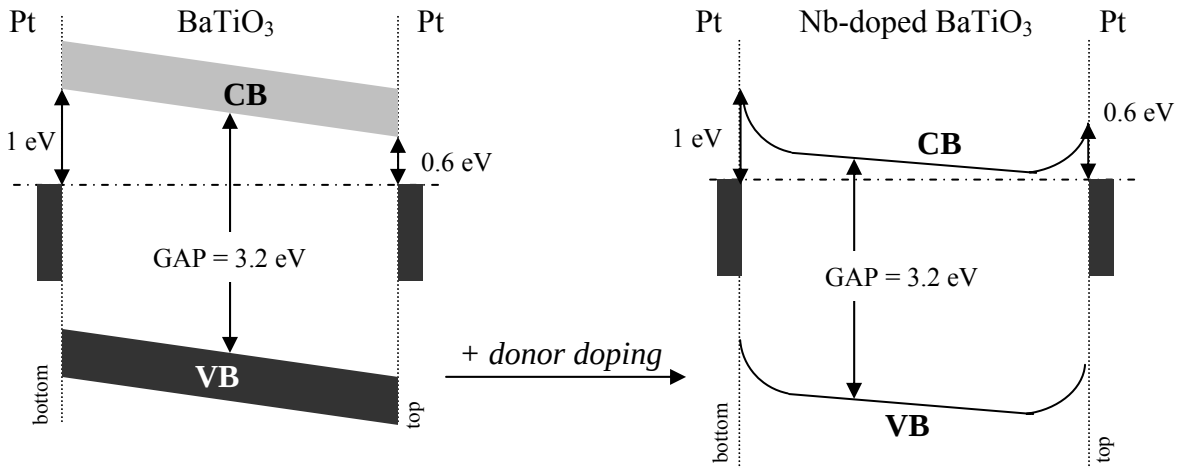

Figure 3.1.3.3: Energy band diagrams for Pt/BTO/Pt and Pt/BTO:Nb/Pt thin film capacitors with barrier heights derived from the results presented above. Doping induce space charge at the metal/film interfaces as sketched by the energy band bending.

According to Fig. 3.1.3.3, the barrier heights obtained during the deposition of Pt onto BTO is higher than those obtained during deposition of BTO onto Pt. By analogy to comparable experiments in BST [12] this tendency is in good agreement with what is typically observed for sputtered materials. In fact, reduced Ti^{3+} states induce by oxygen vacancies were evidenced during growth of Pt onto BTO and Nb-doped BTO and are not detected when BTO and Nb-doped BTO are deposited onto Pt (present paragraph). These extrinsic interfacial

defects (which can be cancelled after oxygen annealing) can induce the observed asymmetry in the barrier heights between top and bottom contacts. The asymmetrical behaviour is observed for both compositions. However, the doping effect seems to influence the interface properties by inducing a band bending in the band alignment as sketched on the right side of Fig. 3.1.3.3. This band bending is in fact a direct consequences of space charge depletion at the Pt/BTO:Nb as well as BTO:Nb/Pt. As discussed in I.1.2 and III.1.2.2, donor dopant (e.g. Nb) increase the charge carrier density in $ATiO_3$ compounds resulting in lower resistivity. These resulting free charges can thus accumulate at the metal/$ATiO_3$ interface inducing space charge region at both side of the ferroelectric.

3.1.3.3 Heterojunction Nb:$SrTiO_3$/$BaTiO_3$

This paragraph reports the chemical and electronic properties and band offsets of STO/BTO heterojunctions. Fig. 3.1.3.4 presents the STO/BTO interface cross-section using Transmission Electron Microscopy (HRTEM). The SAED pattern (Selected Area Electron Diffraction) indicates the single crystalline nature of BTO film

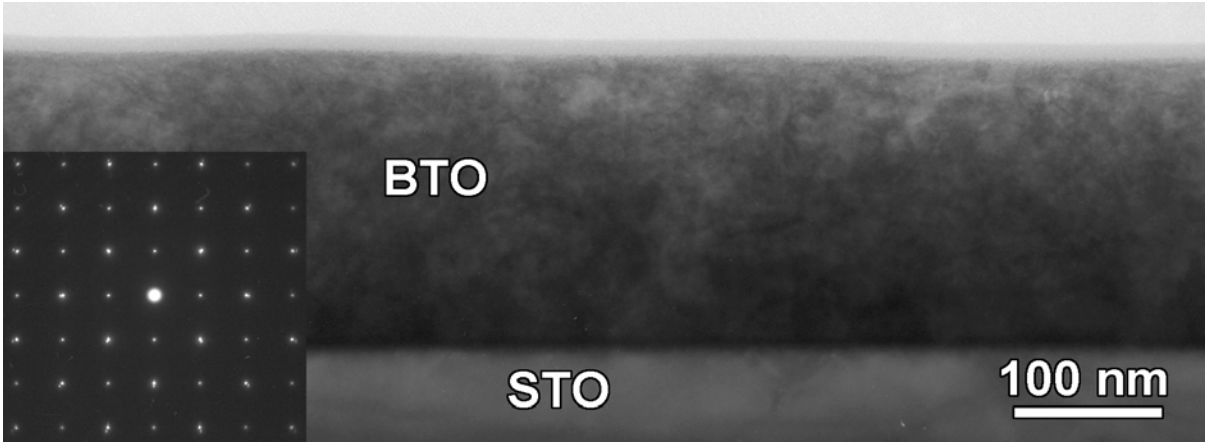

Figure 3.1.3.4: Typical cross-sectional scanning transmission electron microscopy of $SrTiO_3$/$BaTiO_3$ system. BTO thin film is singlecrystalline as evidenced by the inset SAED pattern

Note: The TEM investigations reported here have been performed by Oleg Lebedev from the Electron Microscopy for Materials Research (EMAT) at Antwerp (Belgium).

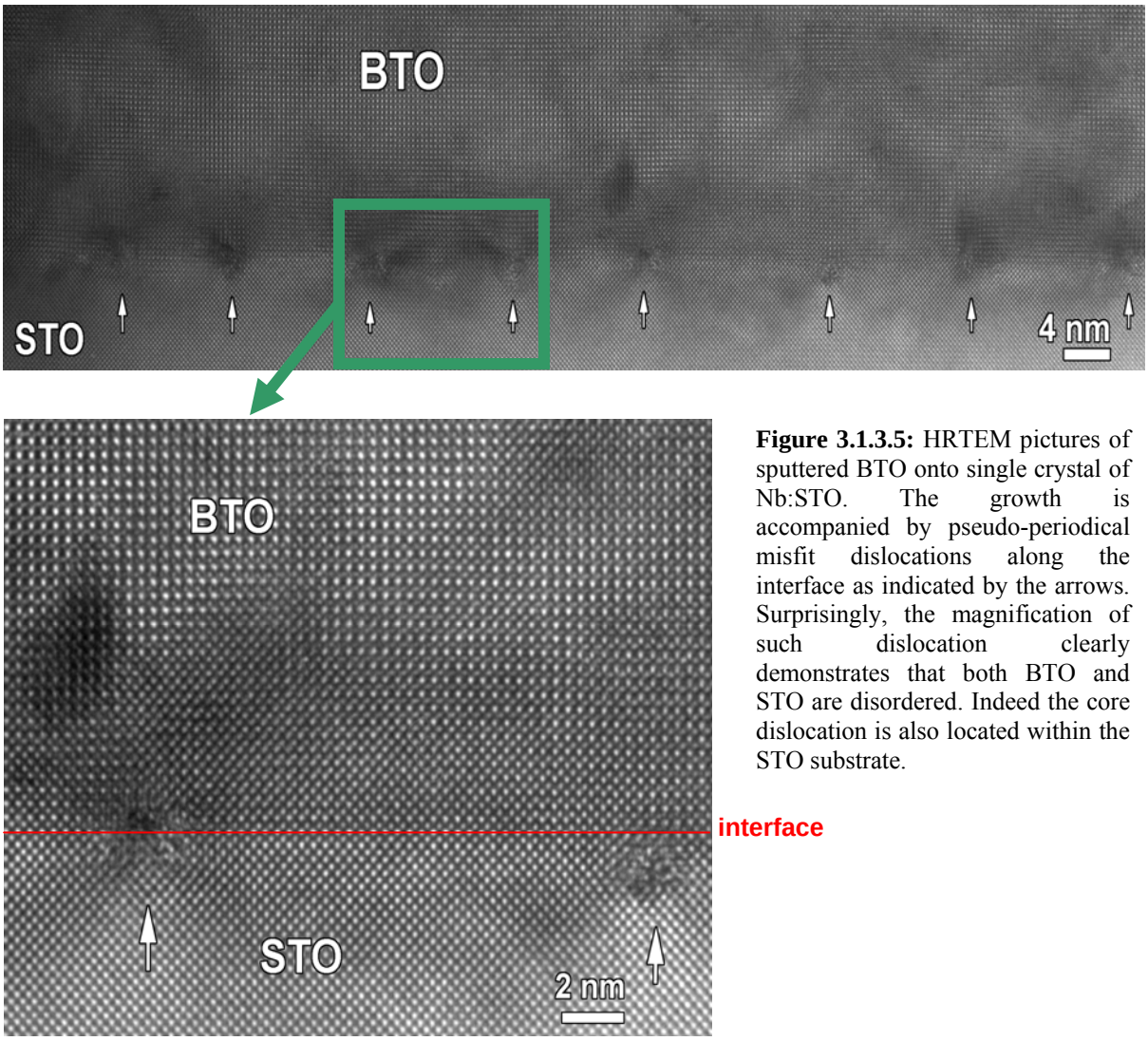

Figure 3.1.3.5: HRTEM pictures of sputtered BTO onto single crystal of Nb:STO. The growth is accompanied by pseudo-periodical misfit dislocations along the interface as indicated by the arrows. Surprisingly, the magnification of such dislocation clearly demonstrates that both BTO and STO are disordered. Indeed the core dislocation is also located within the STO substrate.

As shown on HRTEM cross-section in Fig. 3.1.3.5, there are pseudo-periodical misfit dislocations along the interface. These dislocations are obviously alternatively located at the interfaces and more surprisingly, within the STO substrate with a periodicity of ~20nm. Sample preparation has been performed using Focus-Ion Beam (FIB) which can likely produce extrinsic defects. However, the periodic character of such dislocations allowed us to reasonably exclude an origin from the FIB preparation. It is also very unlikely to generate such damage during the sputter deposition process as the deposited particles do not have enough energy. These defects might be present prior to the BTO deposition but based on the available data no conclusion on the origin of the dislocations is possible. From the present pictures, except for the dislocations, one can moreover see that no Ruddlesden-Popper phases or any extra-phases could be identified at the interface and along the BTO growth.

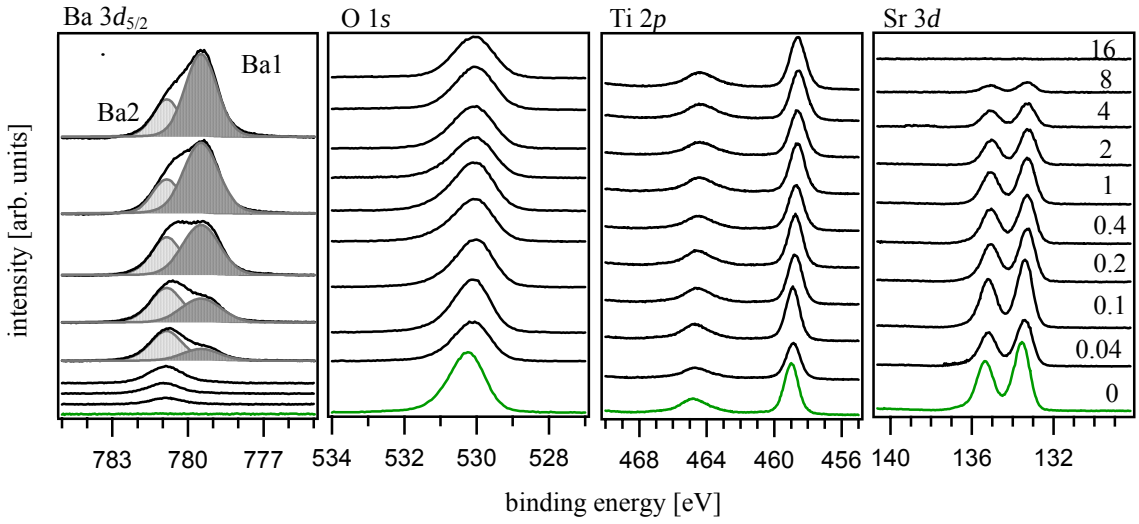

Figure 3.1.3.6: X-ray photoelectron spectra of a $SrTiO_3$:Nb(100) single crystal in the course of $BaTiO_3$ deposition. The BTO thickness is indicated in nm. The green spectra indicate the uncovered state (nude STO). The Ba emissions exhibit two components which have been deconvoluted and indexed in the spectra.

Photoelectron spectra recorded during deposition of $BaTiO_3$ onto Nb-doped $SrTiO_3$ single crystal are shown in Fig. 3.1.3.6. Similarly to the interface experiment performed with Pt wafer, BTO has been stepwise deposited onto STO and after each deposition step, Ba $3d_{5/2}$, O1*s*, Ti 2*p*, and Sr 3*d* levels spectra were recorded. The initial stage of the experiment (uncovered state) can be identified by the green spectra (see Fig. 3.1.3.6). A layer-by-layer growth mode of BTO can be assumed since the Sr 3*d* emission decay exponentially when increasing BTO thickness. No pronounced change of the shape of O, and Ti levels occurs indicating the absence of extrinsic defects as e.g. Ti^{3+} species. However, the Ba level emission is drastically modified in the course of BTO deposition. At very low coverage only the component located at higher binding energy (indexed Ba2 in the graph) appears. Then, Ba1 occurs when increasing film thickness and become higher than Ba2 after subsequent deposition of BTO. A detailed discussion of the Ba components is given in section 3.5.

The evolution of core-level binding energies in the course of deposition is displayed in Fig. 3.1.3.7. An appropriate offset of each core levels was applied to highlight each binding energies change during BTO deposition. The values of each core levels shift is indicated in the graph. Before deposition of BTO, the valence band maximum value of STO was recorded at ~3.05eV after oxygen annealing for surface cleaning. After subsequent BTO deposition a VBM of ~2.85eV ± 0.05eV can be determined. The valence band offset is determined from the difference of the valence band maximum binding energy of the $SrTiO_3$ substrate as given

from the Sr 3*d* line and the $BaTiO_3$ film as given from the two Ba 3*d* lines for the thickness range where both valence band maxima are visible. The corresponding thickness range used for the valence band offset determination is indicated by the gray squares. This range also corresponds to the thickness where Ba1 and Ba2 are following the same binding energy evolution. Regardless of the doping of the $SrTiO_3$ substrate (inducing higher VBM), the Sr 3*d* line and the Ba 3*d* line are at the same binding energies in the transition region indicated in Fig. 3.1.3.7. Consequently, the valence band offset at the STO/BTO junction is determined as 0 eV. Similar experiment has been performed with Nb-doped $BaTiO_3$ target (Nb: 0.5 wt %) and identical procedure was used to plot the BE change in the course of BTO:Nb deposition in Fig. 3.1.3.8.

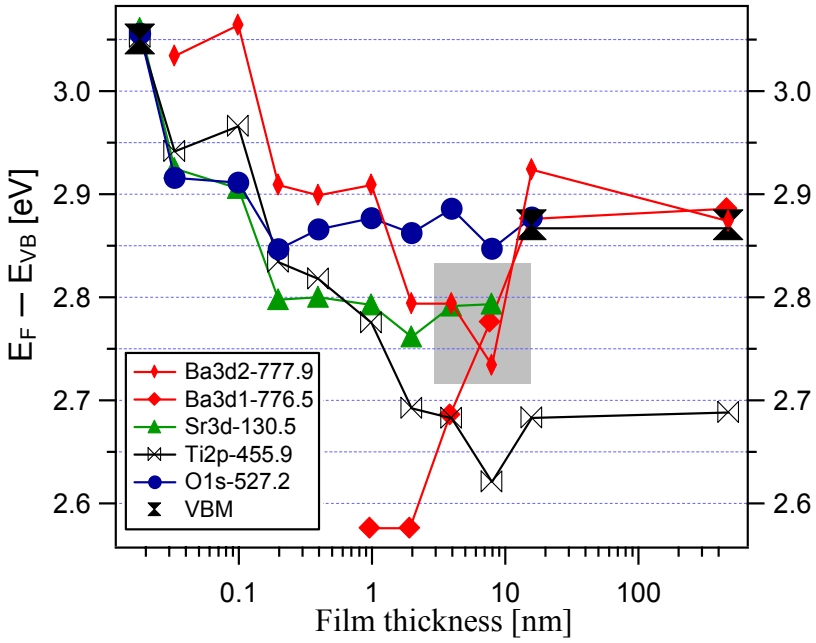

Figure 3.1.3.7: Evolution of $BaTiO_3$ valence band maximum binding energy with increasing film thickness for BTO onto STO. The different shifts are derived from Fig. 3.1.3.6. The gray square indicates the thickness range used for the determination of the valence band offset.

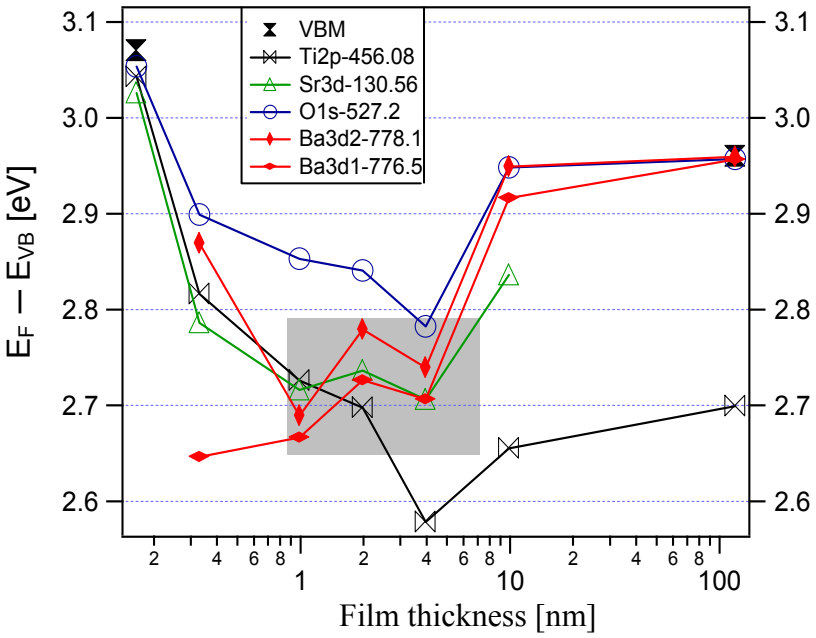

Figure 3.1.3.8: Evolution of Nb-doped $BaTiO_3$ valence band maximum binding energy with increasing film thickness for BTO:Nb onto STO. Identical notation is used to indicate the thickness range for the determination of the valence band offset.

For the Nb-doped sample a quasi similar band offset is extracted from the present plot. We observe higher valence band maxima value for thick Nb-doped $BaTiO_3$ (~2.95eV ± 0.05eV) compared to thick undoped BTO (~2.85eV ± 0.05eV), in good agreement with doping effect induces by donor dopant. We note however that the differences are much larger when BTO and BTO:Nb are deposited onto Pt substrates as showed in section III.3.3. The small difference is a result of the determined band alignment and the doping of the $SrTiO_3$ substrate. Figure 3.1.3.8 also indicates that Sr 3*d* line and Ba 3*d* line in the transition region are similar. This also indicates no valence band offset between $SrTiO_3$ and Nb-doped $BaTiO_3$ similarly to undoped BTO.

In addition, it appears that Ti2*p*─VBM is ~200─250meV larger in STO compared to BTO. This suggests different electronic structures in BTO compared to STO with lower positive charge on the Ti sites in $BaTiO_3$. In addition, by comparing the XPS valence band emissions of STO and BTO, we can also exhibit remarkable differences as shown in Fig. 3.1.3.9 between both titanium perovskites. The spectra were normalized and shifted in energy to emphasize the differences. Typical shape observed in $ATiO_3$ compounds is recalled below (see also II.1.2.2.2).

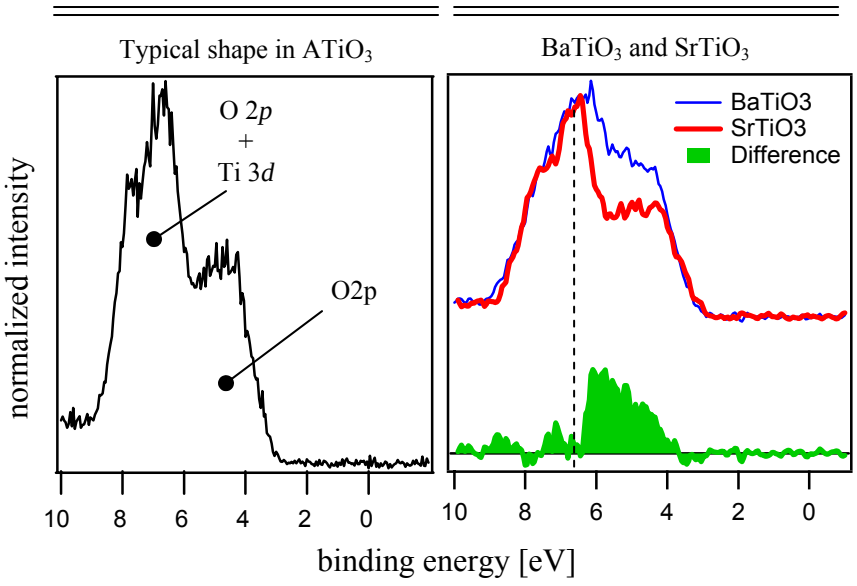

Figure 3.1.3.9 Left: Typical valence band emission for $ATiO_3$ compounds. Two well distinct peaks are observable and indexed in the spectra. **Right**: Observed valence band emission of $BaTiO_3$ thin film and Nb:$SrTiO_3$ single crystal. Both spectra have been normalized and subtracted to elucidate the difference in shape. They are discussed in the text.

When well crystallized, the valence band emission exhibits typical well define peaks containing nearly pure oxygen states (O2*p*) as well as (O2*p* + Ti3*d*) mixed states [32]. Both contributions are indexed on the left side of Fig. 3.1.3.9. The main peak located at ~7eV (dashed line) is clearly broader for BTO than STO. It means that hybridizations of O 2*p* orbitals with Ti 3*d* states are larger in the case of BTO in very good agreement with partial

density of states calculation [33,34] as well as covalency model in perovskites describe by H. Thomann [35]. The well-known paraelectric states in a broad range of temperature for STO is often explained by the bonding nature of Ti─O much more ionic compared to BTO showing several ferroelectric transitions. The present data might be a direct evidence of the covalent character for such system. Measurement of Nb-doped $BaTiO_3$ single crystal seems to support the observed differences (not shown). Systematic studies of different $ATiO_3$ compounds ($CaTiO_3$, $PbTiO_3$, $KNbO_3$, etc…) are required to confirm this point.

According the above experiments, energy band diagrams for Nb-$SrTiO_3$/$BaTiO_3$/Pt can be drawn. Band offset and Schottky barrier are reported according the XPS spectra recorded during interface formation (see Fig. 3.1.3.10). The energy band diagram is highly asymmetric with a Fermi level at the $SrTiO_3$/$BaTiO_3$ interface close to the conduction band as determined in the present section. Usually, the doping level of the $SrTiO_3$ crystal used in the present experiments ($1.7 \cdot 10^{19} cm^{-3}$) is expected to induce a Fermi level position above the conduction band. In our XPS spectra, we observe lower Fermi level (E_F ─ E_{VB} = 3.05 eV) after oxygen annealing that we assumed to be related with lower surface doping. This explains the upward band bending in the $SrTiO_3$ band diagram see in Fig. 3.1.3.10. The origin of the low surface doping is not understood (see also III.3.1.1.4.b).

Identical junctions were studied by Junquera *et al.* [36] using first-principles density-functional theory pseudopotential calculations. Their major results are indicated in Fig. 3.1.3.10.

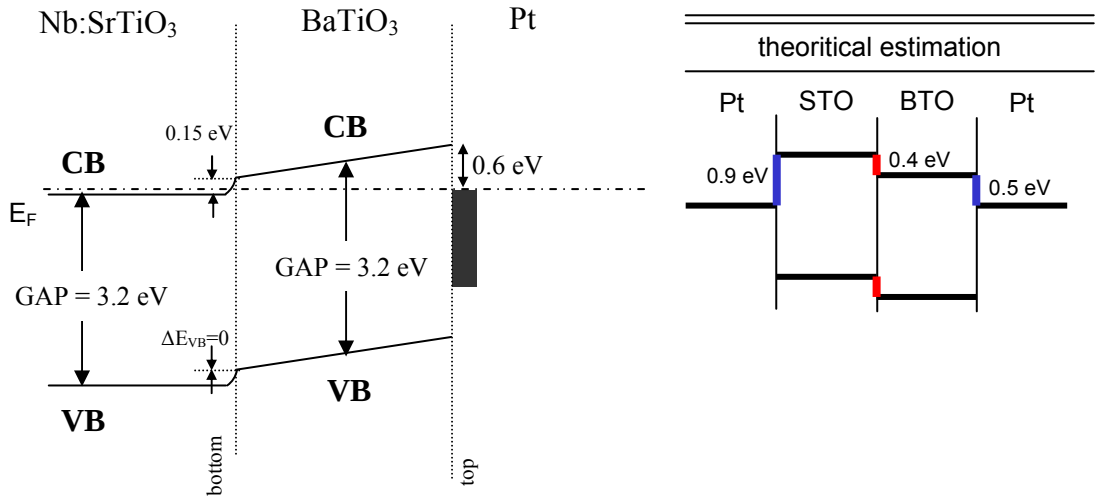

Figure 3.1.3.10: Left: Energy band diagrams for STO/BTO/Pt thin film capacitors with barrier heights derived from the results presented above. The observed offset between STO/BTO junction is reported (~0eV) and an upward band bending in the STO of 0.15 eV can also be observed due to low surface doping. **Right**: Theoretically calculated energy band offset for similar system using first-principles calculation [36].

Junquera *et al.* have in fact determined the valence band offset of Si/SrO/$SrTiO_3$ as well as Si/BaO/$BaTiO_3$ interfaces. Their theoretical estimations showed in Fig. 3.1.3.10 are derived from these two systems. A transitivity of the band alignment with respect to the Si where thus assumed to estimate their STO/BTO band alignment. Similar band diagrams have been determined by Amy *et al.* [37] between $BaTiO_3$/Si and $SrTiO_3$/Si depending on surface treatment using x-ray photoemission spectroscopy. Their results under reduction are showed in Fig. 3.1.3.11 for BTO/Si and STO/Si. The derived band offsets at STO/BTO junction is indicated on the right side as deduced from an ideal transitivity of the band alignment through Si.

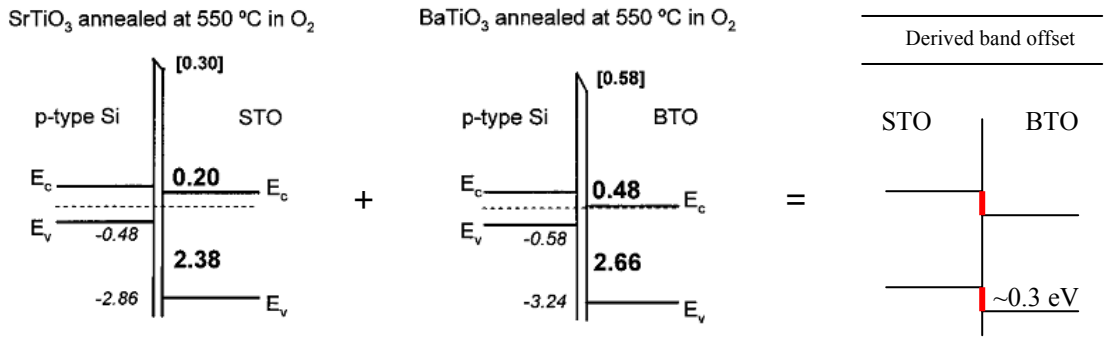

Figure 3.1.3.11: Summary of the band alignment for BTO/Si and STO/Si interfaces from [37]. Assuming transitivity of the band alignment through the Si layer, one can deduce the valence band offset at the STO/BTO interface.

Therefore, our experimentally determined energy band offset at the STO/BTO interfaces (~0 eV) is comparable with the indirect determination of Junquera *et al.* (~ 0.4 eV) and Amy *et al.* (~0.3 eV).

The energy band diagram showed in Fig. 3.1.3.10 thus questions the electrical behaviour of such stacks. As an ohmic contact is clearly established at the STO/BTO interface and a rectifying contact at the BTO/Pt, one can expect strong asymmetry in the current voltage (I–V) measurement. Abe *et al.* [38] have measured the current density of Pt/BTO/Pt and STO:Nb/BTO/Pt stacks respectively. Their results are shown below in Fig. 3.1.3.12:

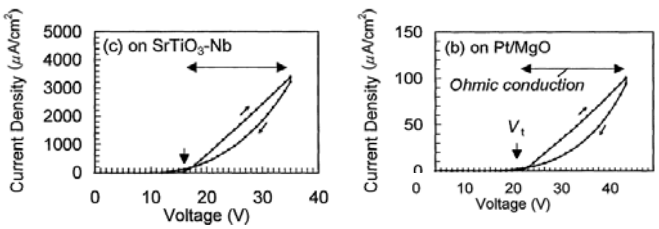

Figure 3.1.3.12: Current density vs. voltage for STO:Nb (left) and Pt (right) bottom electrodes of $BaTiO_3$ thin films. The top electrode is made of Pt for both stacks.

Fig. 3.1.3.12 indicates that current density is substantially larger with STO:Nb substrate compared to Pt substrate. In this measurement, the voltage has been defined as having a positive polarity when a positive bias voltage was applied to the top electrode (Pt-cathode). In this configuration and according the energy band diagram experimentally determined, the electronic charge injection cannot be limited by the ohmic contact of the STO/BTO interface. Thus the energy band diagram shown in Fig. 3.1.3.10 seems to be well appropriate.

3.1.3.4 Conclusion

We can summarize the main results as follow:

- No extrinsic defects were found at the Pt/BTO interfaces. Subsequent higher Schottky barrier could be measured at the bottom contact (1eV) compared to the top contact (0.6eV). This might be explained by the absence of defects at the bottom contact.
- Asymmetrical potential could also be identified for Nb-doped $BaTiO_3$. Charge depletion region inducing band bending was evidenced. The niobium acting as a donor increases most likely the charge carrier density in the BTO generating charged metal/BTO contact.
- HRTEM cross-sectional pictures have revealed periodical-misfit dislocations along the interface STO/BTO. Surprisingly, the dislocations are sometimes located within the STO substrate. No extra structures could be identified. The growth of $BaTiO_3$ onto $SrTiO_3$ is epitaxial allowing consistent analysis of our XPS measurements.
- No strong interactions have been observed during growth of BTO onto Nb-doped $SrTiO_3$ single crystal substrate. The Ba emissions exhibit two components, which are modified in the course of BTO deposition. The component located at higher binding energy (Ba2) initiate the growth at low coverage. Ti, and O levels were not found to be profoundly modified. However, subsequent differences are observed in the valence band emission between STO and BTO. The observed valence band emissions might be correlated with the different covalent character of STO and BTO. At least, both oxides are well-known to exhibit drastically different polarization states as a function of the temperature.

- No direct experimental determination of the band alignment between $SrTiO_3$ and $BaTiO_3$ has been presented so far in the literature. A sharp interface with a zero valence band offset has been experimentally determined at the STO/BTO interface expected to form ideal ohmic contact.

After having investigated the electrode/$BaTiO_3$ contact formation in this section, we show in the next section the actual dielectric properties of such stacks.

3.2 Dielectric properties and microstructure

Catastrophic decrease of dielectric constant is typically observed in ferroelectric thin films regarding their bulk parents (see I.3.1). “Curies anomalies” in dielectric constant normally seen in bulk material and single crystal are progressively suppressed, with (i) increase in diffuseness, (ii) decrease of the dielectric anomaly temperature, (iii) and in some cases, full suppression of ferroelectricity. This section will show that dielectric properties of thin films can be considerably enhanced by improving their microstructure. To probe this, deposition of $BaTiO_3$ and $(Ba,Sr)TiO_3$ thin films have been performed using two kinds of sputtering method. *Off*-axis and *on*-axis sputtering geometries were thus employed for thin film deposition. Then, microstructure studies (AFM, XRD) as well as dielectric properties have been compared to correlate dielectric anomalies and microstructures.

3.2.1 Sputtering deposition under on and *off-axis geometries*

As described in chapter II.2.2.4, sputtering parameters can strongly change thin films stoichiometry as well as the degree of sample crystallinity [39]. When substrates are placed at 90° to the target’s azimuthal axis, *off*-axis sputtering configuration is used. This kind of configuration induces lower back-sputtering damage at the film surface since the resputtering problem arising from fast ion is reduced [40] compared to conventional geometry where substrate is facing the sputtered target (*on*-axis). In off-axis geometry, the deposition rate is also strongly reduced resulting in better films cristallisation. The different configurations are schematically sketched in Fig. 3.2.1 (also shown in chapter II.2.2.4).

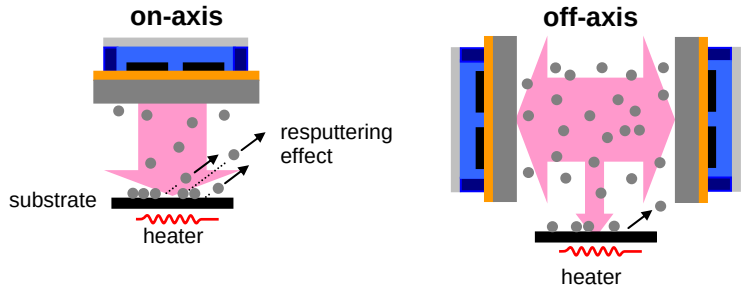

Figure 3.2.1: **Left**: on-axis configuration. Due to fast ions collisions, resputtering effect occurs. **Right**: off-axis geometry reducing the growth rate and thus the energy transfer collision on the substrate.

In this section, both configurations were used for thin film deposition of $BaTiO_3$ and $(Ba,Sr)TiO_3$ compositions. Thin films deposited with *off*-axis technique were grown on (111) oriented platinised Si wafer with a substrate temperature of 650°C, a gas pressure of 5Pa

(99% Ar and 1% O_2) and a power density of ~1W/cm². The growth rate using these conditions was ~0.5 nm/min. The base pressure before sputter deposition was 10^{-5} Pa. For the depositions under *on*-axis configuration, we have used similar deposition conditions except for a power density of ~2.5 W/cm^2 and a substrate to target distances of 7cm for BST and 10cm for BTO with planar geometry. These deposition conditions have been optimized to obtain stoichiometric and crystallised thin films. Such parameters led to a deposition rate of ~1.9 nm/min, 4 times faster than transverse sputtering geometry. In the following sub-section, it will be shown that such a difference in growth rate can drastically modify the microstructure and dielectric properties of thin films.

3.2.2 Microstructure of polycrystalline thin films of $BaTiO_3$

The surface morphologies for the different deposition techniques and for $BaTiO_3$ composition are shown below in Fig. 3.2.2. Two major tendencies are extracted from the present AFM scanning. First, it appears that grain sizes are larger in the case of off-axis sputtered thin films. We can estimate an average size of ~75nm and ~50nm respectively for BTO grains prepared by *off*-axis and *on*-axis geometry. Then, higher roughness are observed for with larger grains as a direct consequences from grain size effect as sketched below in Fig. 3.2.3.

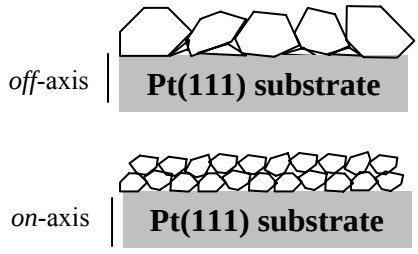

Figure 3.2.2: Large grains induce higher surface roughness. Similar observations are measured for both compositions

It would also be nice to measure the surface morphology for sputtered thin films of (Ba,Sr)TiO_3 deposited under *on*/*off*-axis configuration but the comparison could not be clearly established due to technical problem arising from the deposition step.

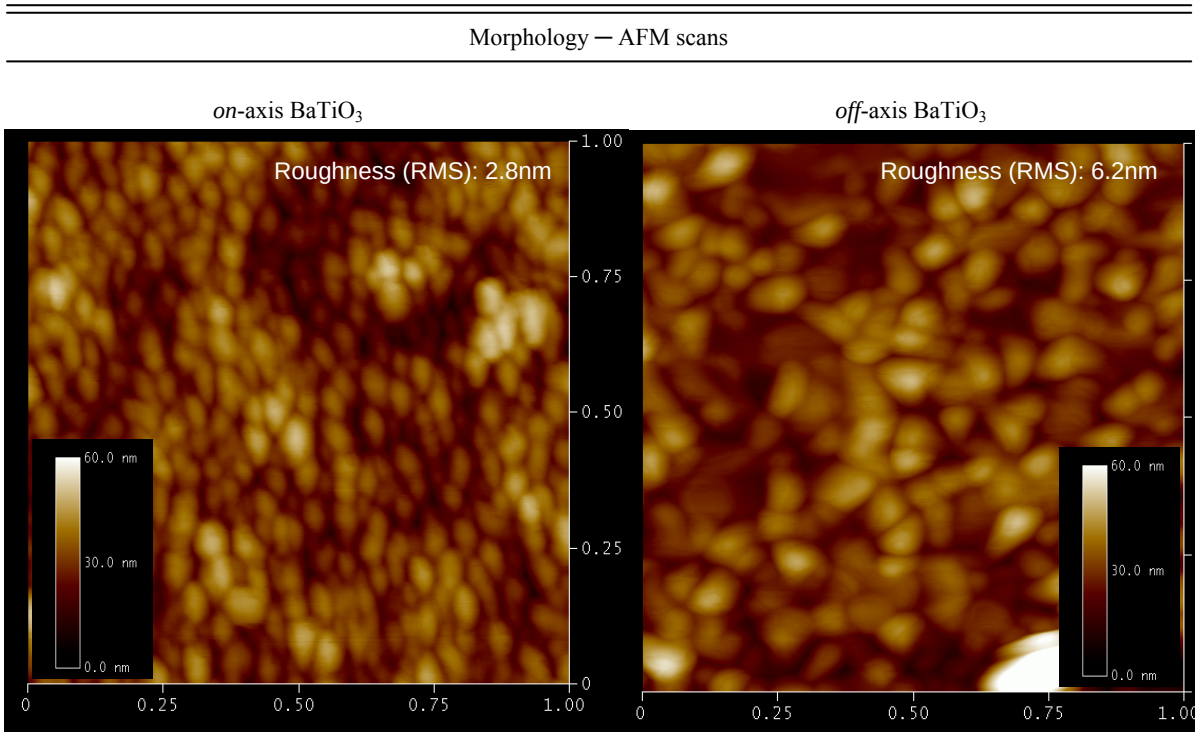

Figure 3.2.3: AFM pictures of the surface of $BaTiO_3$ thin films deposited onto polycrystalline Pt(111) under different sputtering geometries. The thicknesses are respectively ~300nm and ~200nm for on-axis and off-axis depositions. These pictures give evidence that grain sizes are larger with off-axis condition (identical scanning scale is presented for better comparison). Due to grain size effect, the roughness is consequently flattened for smaller grain sizes.

XRD patterns for the different investigated systems are presented in Fig. 3.2.4. All diffractograms were normalized to the Pt(111) diffraction peak to evidence the differences in shape and intensity. All the films are polycrystalline and show the (100), (110) and (200) perovskite peaks of the BTO (Left) and BST (Right) phases. The corresponding samples are indicated in their respective frames. *Off*-axis sputtered films (red) alone display a strong (h00) preferred orientation whereas *on*-axis method (black) do not induce particular preferential crystallographic orientation. In addition, the narrowee full width at half maximum (FWHM) for *off*-axis samples indicates larger crystallite size (i.e., lowering of germination sites) in very good agreement with our previous AFM observations in $BaTiO_3$. This also strongly suggests bigger grains for *off*-axis BST than *on*-axis ones even if it can not be entirely confirmed due to the lack of AFM results. Therefore, based on the following results, it is concluded that the microstructure of $BaTiO_3$ and $(Ba,Sr)TiO_3$ thin films are subsequently improved (in term of crystallite size) with *off*-axis sputtering geometry compared to conventional *on*-axis deposition.

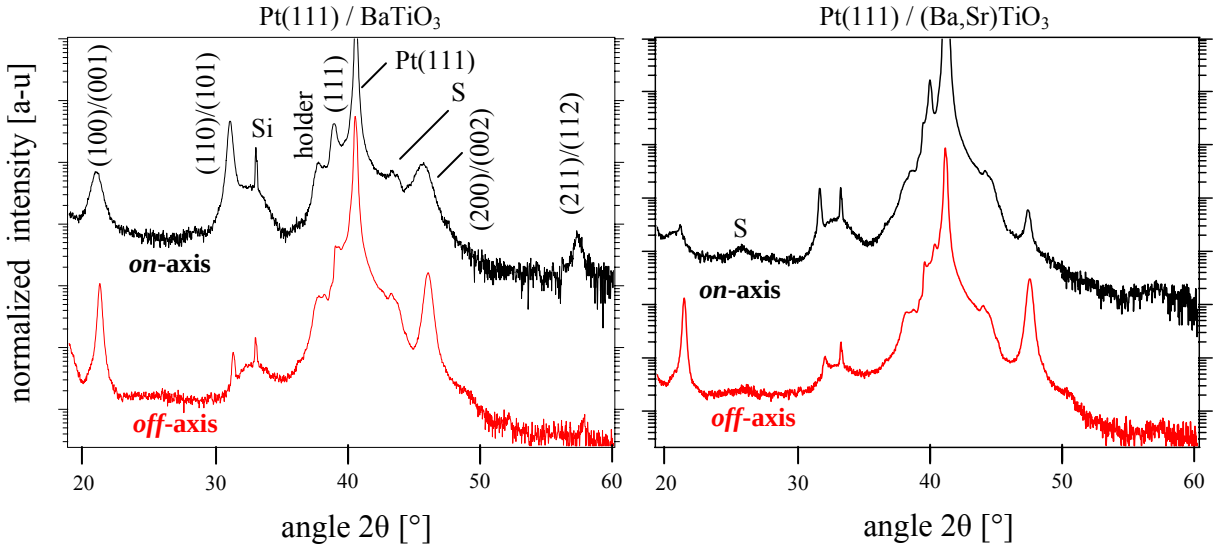

Figure 3.2.4: θ─2θ x-ray diffractograms of $BaTiO_3$ (Left) and $(Ba,Sr)TiO_3$ (right) thin films prepared by both mentioned method. The spectra have been normalized to the Pt(111) Bragg refelections and logarithmic scales were used to attest the absence of parasitic phases.

The microstructural properties have been studied and have revealed that lowering of the growth rate promote the crystallization of the sputtered materials. Since our aim is to establish a direct correlation between structures and dielectric properties, we have measured the temperature dependence of the dielectric constant (ε_R) and the electrical loss at zero bias in a broad range of temperature (-150°C to +150°C) at varying frequencies. The results are presented in the next paragraph.

3.2.3 Dielectric properties of polycrystalline Pt/ATiO$_3$/Pt capacitors (A=Ba & Ba,Sr)

The top and bottom Pt electrodes were connected to an HP4194A impedance analyzer as described previously in chapter II.2.2.5. The plot of the dielectric constant (ε_R) as a function of temperature is displayed in Fig. 3.2.6 for Pt/BTO/Pt stacks prepared with both sputtering methods. A strong increase of the permittivity is observed at high temperature (T>100°C) and mostly in the low frequency range (f<100 kHz). Such behaviour is often attributed to conduction phenomena occurring at high temperatures for thin film samples [41]. This consequently explains the decrease of the dielectric constant when decreasing the temperature due to "freezing" of the conduction mechanism (i.e., when no longer thermally activated). Two major observations are extracted from the present plot. First, ε_R is notably higher for BTO *off*-axis sputtered (~370 at T_{room} and 100 kHz) compared to *on*-axis deposition (~260 at

T_{room} and 100 kHz). Then, both samples exhibit a dielectric anomaly at high temperature which is superimposed to the conduction phenomena. Both anomalies have been highlighted in the spectra by gray squares.

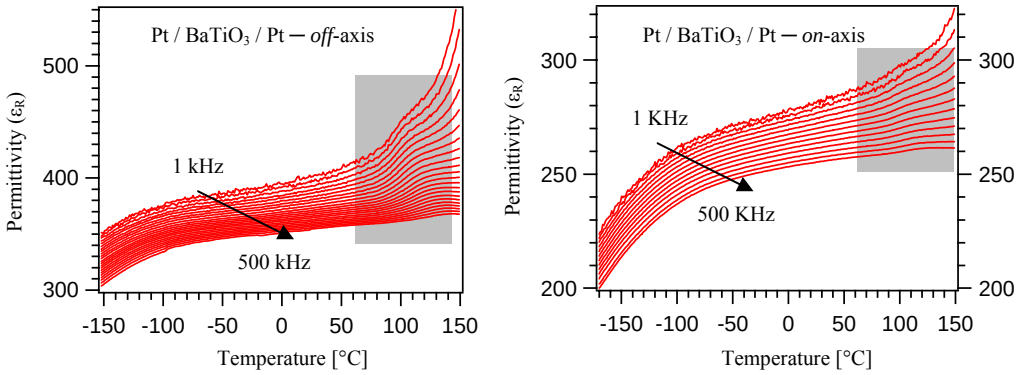

Figure 3.2.6: Relative permittivity (ε_R) versus the temperature for identical composition of $BaTiO_3$ deposited under off-axis and on-axis geometries. Gray square indicate dielectric anomaly around 120°C as discussed in the text.

Under rescaling,, we can reveal more closely these dielectric anomalies as presented in Fig. 3.2.7. The corresponding loss factor have also been reported since important information can only be concluded by examining simultaneously dielectric permittivity and loss factor as discussed in details in the first part of this manuscript (see chapter I.1.1.1.b *Mechanism of polarization*). Following Fig. 3.2.7, both dielectric anomalies become evident for both BTO thin films. The observed anomaly is obviously much more well defined in shape and is also frequency independent for the *off*-axis sputtered BTO compared to *on*-axis sputtered BTO. In this latter case, the smaller crystallites observed in AFM and confirmed with XRD may alter the dielectric maximum. In ceramics and thin films, the smearing of the dielectric anomalies is usually observed because of reduced grain sizes.

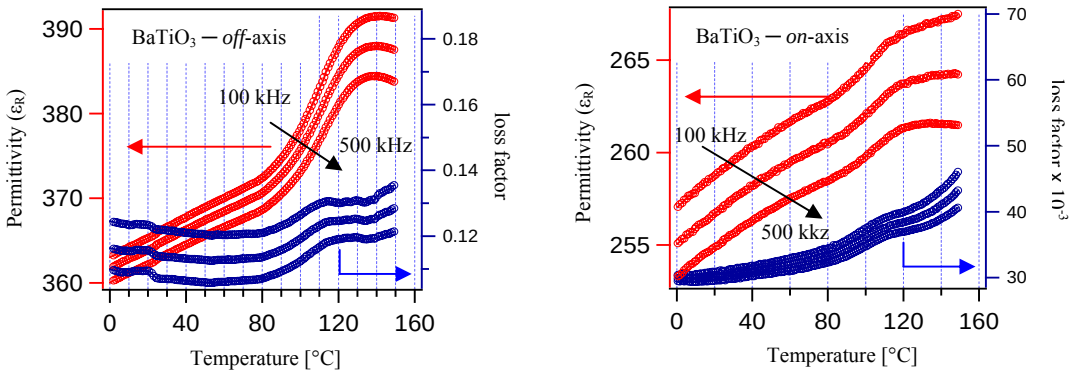

Figure 3.2.7: Magnification of the dielectric anomaly showed in Fig. 3.2.6 for both deposition geometries. The corresponding loss factors are also reported showing good agreement for true phase transition at least for *off*-axis sputtered thin films.

Furthermore the dielectric anomaly appears at ~140°C in good agreement with typical Curie temperature in single crystal or ceramic of $BaTiO_3$ (T_c=130°C). In addition, the loss factor adopts almost similar tendency but has smaller maximum temperature than the dielectric permittivity. This might be explained by the superimposition of both contributions (conduction phenomena + phase transition). The conduction phenomenon is indeed frequency dependent as evident from Fig. 3.2.6. Similar conclusion can not be entirely assumed for thin film deposited under *on*-axis condition since the observed maximum is highly frequency dependent for ε_R. To underline this frequency dependence, the same spectra have been shifted along the permittivity axis in Fig. 3.2.8. It would also be nice to record additional data at higher temperature to observe the Curie-Weiss behaviour by plotting the inverse of permittivity in the paraelectric state (see chapter I.1.3.2). However, technical limitations did not allow increasing the temperature above 150°C since the sample holder was made of Teflon.

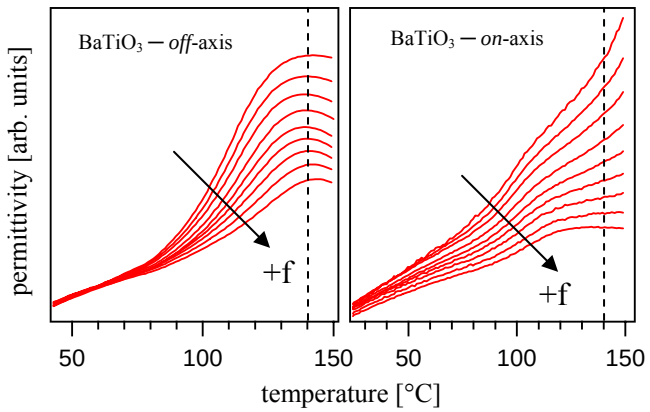

Figure 3.2.8: Permittivity profiles versus the temperature. The data are derived from Fig. 3.2.7 and shifted only the y-axis to evidence the frequency dependence. From the present plot, *off*-axis sputtered BTO are clearly frequency independent contrary to *on*-axis BTO dielectric dispersion.

Similar comparison has been performed for $(Ba,Sr)TiO_3$ thin films deposited with both sputtering methods. The situation is summarized below in Fig. 3.2.9 for BTO and BST at 500 kHz..

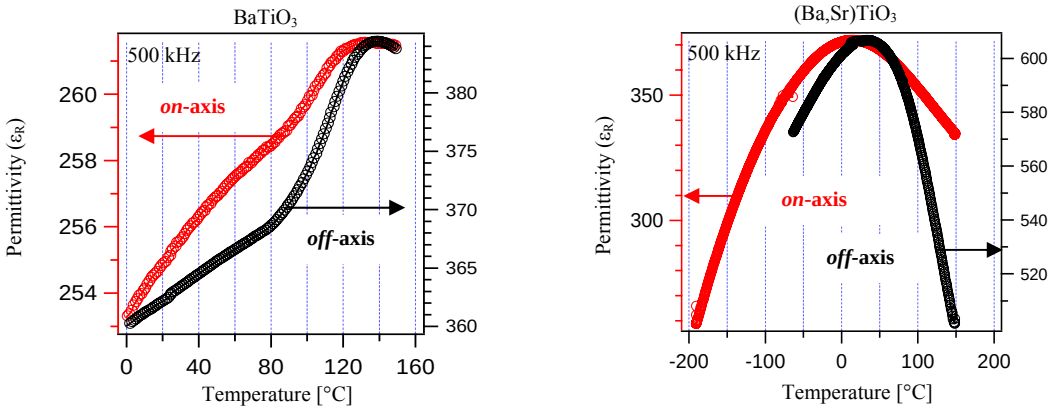

Figure 3.2.9: Comparison between thin films prepared is off/on axis geometry for both $BaTiO_3$ and $(Ba,Sr)TiO_3$ compositions with (Ba/Sr=60/40). Off-axis sputtered thin films exhibit sharper profiles and higher permittivity than on-axis .deposition.

There is an excellent agreement with the Curie temperature expected for bulk materials for $Ba_{60}Sr_{40}TiO_3$ compositions (Tc=0°C). Therefore, it can be concluded that true phase transitions occur in sputtered BST thin films with a permittivity which is considerably improved using *off*-axis sputtering geometry in good agreement with the previous tendencies observed for $BaTiO_3$ thin films. Thus, Curie-Weiss behaviour is plotted for BST thin films since the amount of collected data above the maximum of permittivity is now sufficient to extrapolate the Curie-Weiss temperature ($T_{c\text{-}w}$). The results are indicated in Fig. 3.2.10 for thin films and typical behaviour encountered for bulk materials. The plot confirms improvement of ferroelectric properties using *off*-axis deposition even if they remain largely below those observed in bulk materials. For instance, one of the most important features observed in bulk materials is the temperature range separating the Curie (T_c) and the Curie-Weiss ($T_{c\text{-}w}$) of only few degrees. However, *off*-axis sputtered film exhibits rather $T_c >> T_{c\text{-}w}$.

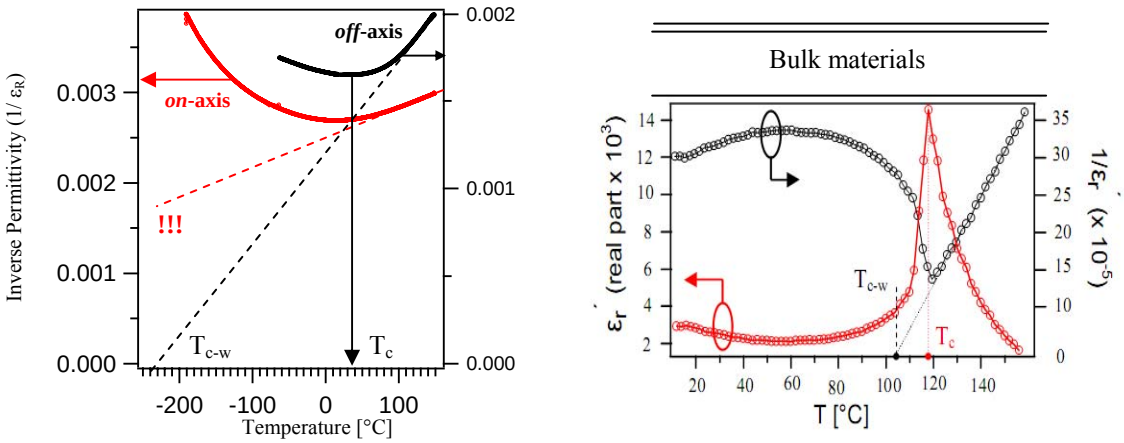

Figure 3.2.10: Left: $(Ba,Sr)TiO_3$ thin films sputtered with *on*/*off*-axis geometry. Curie-Weiss behaviour is subsequently improved for *off*-axis deposition but remains largely below the bulk value expected to occur at ~0°C for $Ba_{60}Sr_{40}TiO_3$ composition in the bulk form. **Right**: Curie-Weiss behaviour is indicated for bulk BTO in order to show that T_c and $T_{c\text{-}w}$ are expected to be separated by only few degrees for ceramic or single crystal.

Tunability (τ) properties have also been compared between both kinds of depositions for BST compositions. The results are displayed in Fig. 3.2.11.

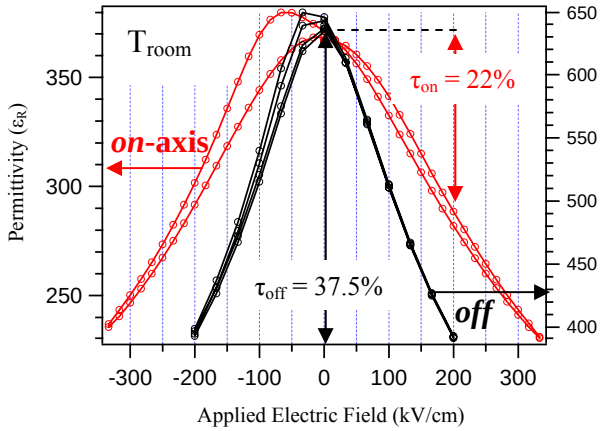

Figure 3.2.11: Permittivity versus applied electric field for Pt/BST/Pt capacitors. At 200 kV/cm, the tunability (τ) of on-axis thin film is much lower than the one obtained by off-axis geometry as indicated in the graph.

Here again, the ability to tune the permittivity by varying the electrical field is subsequently improved with *off*-axis deposition. A quantitative comparison is indicated in the above graph for a given electrical field.

3.2.4 Conclusions

To summarize, excellent correlations are evidenced between the results obtained with AFM, XRD, and impedance spectroscopy. *Off*-axis sputtering deposition subsequently (i) enlarge the crystallite, (ii) increase thin films texture, and (iii) improve ferroelectric properties as compared to conventional *on*-axis deposition. Therefore, clear correlation between microstructure and dielectric properties has been successfully demonstrated. However, further investigations on BST crystallite sizes and texture are required to directly probe bigger grains for *off- axis* sputtered BST thin films.

Nevertheless, the tendency of the results strongly suggests that interfaces such as grain boundaries play a fundamental role in the polarization states of $ATiO_3$ compounds since they can be assumed in lower density for thin films containing larger grains.

Consequently, this is a strong motivation in the present PhD work to study interface properties of such capacitor systems.

3.3 Surface segregation in Nb-doped $BaTiO_3$ thin films

This section describes in-situ photoemission spectroscopy to investigate niobium doping in polycrystalline $BaTiO_3$ materials. Ceramics and single crystal have been measured for comparison with thin films. Nb-doped $BaTiO_3$ ceramics and Nb-doped $SrTiO_3$ single crystal show higher Fermi level position regarding the films. This was confirmed by impedance spectroscopy under variable temperature. Large amount of niobium is clearly observable at surface but the amount of dopant is drastically reduced below the near-surface region, as evidenced by depth profile. This surface segregation may arise from a low solubility of niobium in sputtered BTO films which would explain the low conductivity of such doped films.

3.3.1 Introduction

The influence of doping has been reported in details in section I.2 for bulk $ATiO_3$ oxides. In thin film form, the available results reported in literature are much more contrasted as shown in Fig. 3.3.1.

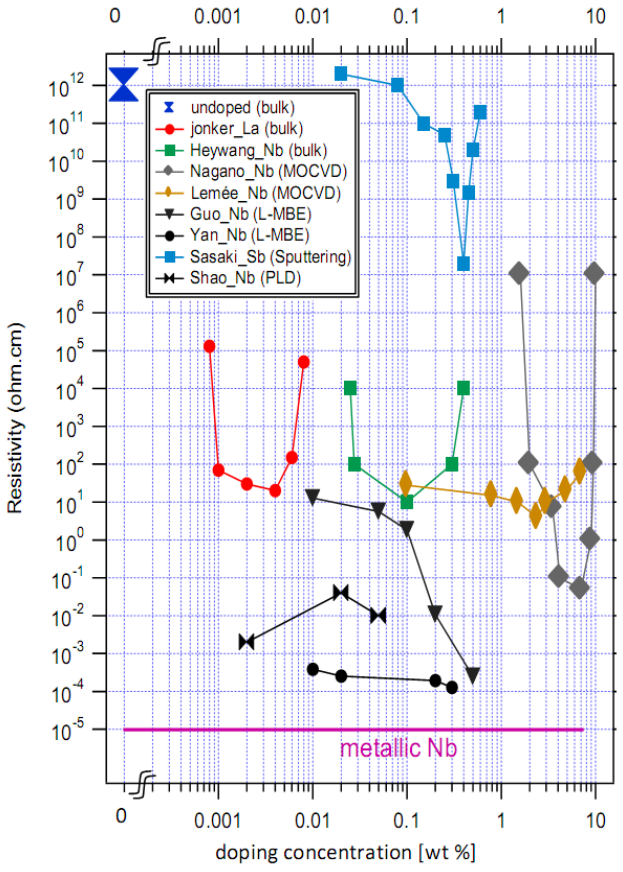

Figure 3.3.1: Resistivity of $BaTiO_3$ vs. doping concentration dependence for thin films and ceramics. The references used for the plotting are the following: Jonker [41], Heywang [42], Nagano [43], Lemée [44], Guo[45], Yan [46], Sasaki [47], and Shao [48].

All thin films behave strongly different from the bulk, regardless of the preparation technique. Large fluctuations are also observed among the films themselves. Samples prepared by Laser Molecular Beam Epitaxy (L-MBE) [45,46] show extremely low resistivity ~ (10-10^{-4} Ω.cm) in contrast with sputtered films ~ (10^{8}-10^{12} Ω.cm) [47]. The change of resistivity for films grown by chemical vapour deposition (MOCVD) [43,44] is roughly comparable to the bulk, but the minimum resistivity is only observable at higher doping concentrations. Therefore, thin film properties strongly depend on the deposition technique used for samples preparation. In this section a combination of in-situ X-ray photoelectron spectroscopy (XPS) and impedance spectroscopy is used to understand the high resistivity of magnetron-sputtered Nb-doped BTO thin films. We first determine the Fermi energy level position with respect to the band edges and the chemical composition. For oxides, the Fermi level position observed by XPS correlates well with electrical conductivity [49-51]. In the second part, permittivity and loss factor were measured using impedance spectroscopy as a function of temperature, confirming the lack of conductivity of our films. Finally, we will provide evidence that niobium is not incorporated in large amount in the grains of the films but rather segregates to the surface (and probably also to grain boundaries). Nb-doped BTO ceramics and single crystal of STO samples have also been measured for comparison.

3.3.2 Semiconducting character

The valence band maxima (VBM) were determined by linear extrapolation of the leading edge. The Fermi energy reference (0 eV) was calibrated using a sputter cleaned metallic Ag reference standard. As described in chapter II, the Fermi energy position can indeed be derived from the valence band (VB) emission. The different valence band spectra are presented in Fig. 3.3.2.

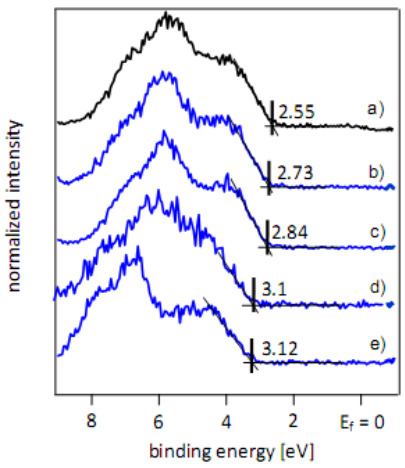

Figure 3.3.2: X-ray valence band spectra recorded from **a)** thin film of undoped BTO, **b)** thin film of BTO:Nb (0.05 wt%), **c)** thin film of BTO:Nb (0.5 wt%),**d)** ceramic of $BaTiO_3$:Nb (0.02 wt%), and **e)** single crystal of STO:Nb (0.05 wt%). For **b)** and **c)** the amount of Nb is related to the sputtered target stoichiometry.

The undoped film exhibits a VBM of ~2.55 eV whereas the film containing the highest doping has a VBM of 2.84 eV. The Nb doped film has thus higher Fermi level position, as expected for *n*-type doping. However, a typical *n*-type semiconductor sample should have its Fermi level located close to the conduction band, as observed for Nb-doped $SrTiO_3$ [12] also showed in Fig. 3.3.2. According to the band gap of BTO (3.2eV), this would lead to a VBM of 3 eV at least. Both doped films do not reach comparable high levels (2.84 eV and 2.73eV). It appears that the doping in the films does not shift the Fermi energy significantly towards the conduction band. Hence, the Nb doped films are expected to have a lower conductivity level.

3.3.3 Impedance spectroscopy

To check the resistivity behaviour of our sputtered films, impedance spectroscopy has been performed. Variation of the dielectric properties for two films is shown below in Fig. 3.3.3. We note that thin films have been sputtered under *on*-axis geometry.

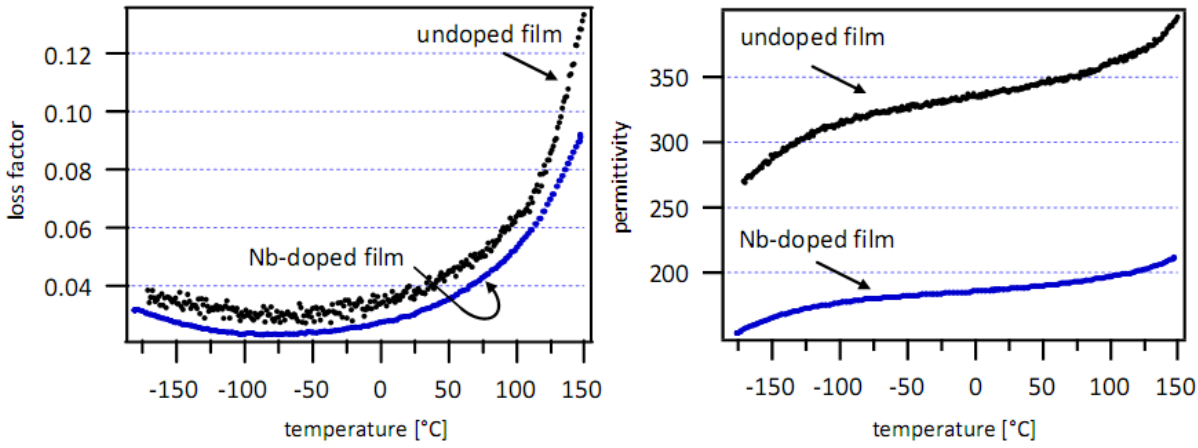

Figure 3.3.3: Relative permittivity and loss factor vs. temperature at 100 Hz for undoped $BaTiO_3$ thin film and Nb-doped $BaTiO_3$. No increase of conductivity for doped sample is observed at high temperature.

At 100 Hz and room temperature, the undoped film exhibits a permittivity value around ~350, much higher than the observed permittivity for the Nb-doped film (~200). Both profiles do not show any obvious temperature dependence. The increase of loss factor and permittivity observed at high temperature is a typical signature of thermally activated conduction mechanisms as described in section (II.2.2.). In the case of doped materials, this enhancement should be higher than for the undoped composition. But no significant difference is observed

at high temperature. The doped film appears to be even a better insulator (lower loss) as compared to the undoped film. However, both films exhibit resistances of the order of 10^{10} Ω as computed from the impedance data. In bulk form, when suitably selected, a small amount of dopants (e.g. few ppm of Nb, La…. in $BaTiO_3$) is able to induce macroscopic increase of conductivity [52] because of energy levels located relatively close to the conduction band. As in any semiconductor, such charged states are well-known to accumulate at interfaces inducing space charges. Because of the very small thickness of such depleted interfaces, the apparent capacitance can be subsequently increased, especially at low frequency/high temperature range [53]. There is thus a close link between the semiconductor behaviour of doped $BaTiO_3$ and an artificial increase of the apparent permittivity due to the additional space charge capacitance. In our sputtered BTO:Nb films we see neither an increased conductivity nor a strong apparent permittivity. This confirms the inefficient Nb doping in our $BaTiO_3$ thin films since we were not able to measure the resistivity by 4-points techniques. Both Pt and InGa electrodes were used but the observed resistivity was again too high to be measurable. This agrees with the previously reported resistivity experiments in sputtered Sb doped $BaTiO_3$ [47].

3.3.4 Surface niobium segregation

Evidence for the origin of the inefficient doping of magnetron sputtered $BaTiO_3$:Nb films can be obtained from the cation stoichiometry. As the concentration of dopant is very weak, niobium doped single crystals of $SrTiO_3$ have been measured with our XPS setup as reference. The surfaces were cleaned before photoemission measurements by in-situ thermal annealing in an oxygen pressure of 0.05 Pa. Single crystals were purchased with different niobium concentrations: 0.05 wt% and 0.5 wt% are the amounts given by the provider (Crystec). As seen in Fig. 3.3.4, a Nb emission is clearly observed for the 0.5 wt% sample. Using the sensitivity factors for the XPS setup and the appropriate molar mass, a Nb concentrations of ~0.8 wt% is extracted from the peak intensities, in good agreement with the nominal Nb content. No Nb could be detected for the 0.05 wt% Nb-doped STO crystal. Also no niobium was detected on the conducting ceramic BTO sample, which shows a high Fermi level position (see Fig. 3.3.2).

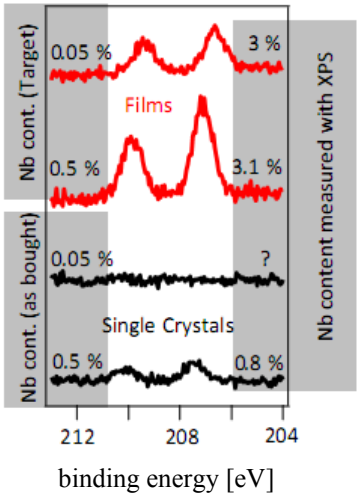

Figure 3.3.4: Nb 3*d* core-levels recorded from sputtered thin films of Nb-doped $BaTiO_3$ (red) and Nb-doped $SrTiO_3$ single crystals (black). The Nb content indicated on the right side has been experimentally determined from the XPS emissions.

Evidently, the Nb content required to induce electrical conductivity is below the detection limit for ceramic and single crystals samples. As indicated in Fig. 3.3.4., the amount of Nb is ~3 wt% for the films prepared from either 0.05 or 0.5 wt% doped targets. We are now going to show that doping enrichment is confined to surfaces.

The substantial Nb contents measured at the surfaces by XPS might be caused by segregation of Nb at the surface. To check if the dopant concentration is lower below the surface, depth profile analysis has been performed. Fig. 3.3.5 displays the effect of ion-beam etching with 1 keV Ar^+ ions on the Nb 3*d* core level.

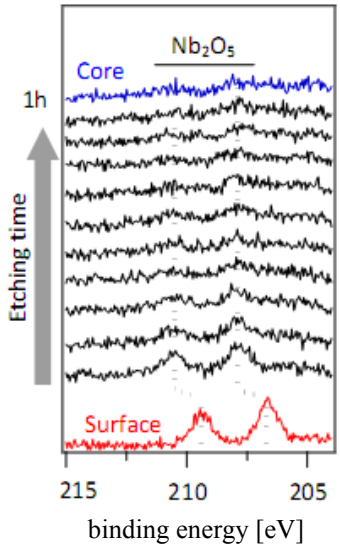

Figure 3.3.5: Nb 3*d* core level of sputtered Nb-doped BTO thin films in the course of Ar+ etching. Clear Nb enrichment at the surface is evident from the spectrum.

The red spectrum represents the situation prior to the etching and the blue one corresponds to the last etching step. The amount of niobium is drastically reduced after sputtering. The Nb concentration observed after ion etching is less than 0.5 wt%. The binding energy shift of ~1eV detected after the first etching step occurs in all core levels and can therefore be

explained by a charging of the surface due to small amounts of Ar^+ implantation rather by chemical changes of the Nb species. The reduction of niobium concentration in the course of sputtering indicates that Nb is not incorporated in large amounts in thin films but segregates to the surface.

3.3.5 Discussion

Doping effect on electrical properties seems to be drastically different between thin-films and their bulk parents. Our results show: (i) Different Fermi level position for sputtered films and ceramic, (ii) dielectric properties of $BaTiO_3$ films not affected by niobium doping and finally, (iii) niobium segregation at the surface for thin films. The measurements of large grain materials (ceramic and single crystals) show that the dopant concentrations below the detection limit of XPS can lead to strong shifts of the Fermi level. This indicates a high doping efficiency and properly incorporated dopants. The situation for sputtered thin films is strongly different. Although a large amount of niobium is observed, the Fermi level positions measured in the films are only slightly affected by Nb doping. The ineffective doping is attributed to a poor incorporation of Nb in the grains. The available Nb largely segregates to the surface, and, most likely, also to grain boundaries. The presence of impurity phases involving Nb segregation was also evidenced in Nb-doped BTO prepared by MOCVD explaining the observed loss of epitaxy [44]. TEM was used in sputtered Mg-doped BST to provide segregation evidence of MgO which was not observable in their XRD patterns [56]. For ceramics samples, non-complete Nb incorporation inducing dopant segregation in the grain boundary region was also successfully investigated [54,55]. The dielectric properties of the $BaTiO_3$:Nb films are also in agreement with poor Nb incorporation in the grains. Nb-oxide is a good insulator with a low dielectric permittivity. It can induce an increase of the resistivity and a decrease of the effective permittivity. This is exactly what has been observed on comparing pure and Nb doped $BaTiO_3$ films. The lack of conductivity in our sputtered films can thus be related to the segregation of Nb. However, the niobium segregation is not fully understood. It may occur during the deposition process due to re-sputtering and re-evaporation effects can occur [1-3]. The driving force for segregation may be related to the effective oxygen partial pressure during deposition. This is indicated by the observation that surfaces of Nb-doped films are Ba-rich while those of undoped films are Ti-rich as also observed for $(Ba,Sr)TiO_3$ (see section II.2.1). The enrichment of the A-site cation (Ba) at the surfaces of donor doped perovskite is typically observed under oxidizing

conditions as A-site vacancies act as compensating defects for donors [56,57]. However, such mechanisms require noticeable donor concentrations in the grains. Similar Ba enrichment in sputtered $BaTiO_3$ thin films have been reported such as Ba_2TiO_4 phases with Ho doping [58], Sb doping [47] and Nb doping [59]. The absence of extra peak in our XRD patterns suggests that the observed Ba enrichment might form an amorphous phase. Therefore, it seems that impurity phases are often observed in the literature for doped thin films. Nevertheless, their involvement to explain the electrical properties difference with bulk materials is rarely suspected. Further experiments are required to understand the change in composition between undoped and doped films. The tendency for donor segregation can not be ruled out to explain why no PTCR effect is observed in thin film samples.

3.4 Surface layer of $BaTiO_3$ thin films under oxidizing condition

In this section, deviations from stoichiometry and heterogeneous surface compositions of $BaTiO_3$ textured thin films, $BaTiO_3$:La ceramics, and $SrTiO_3$:Nb single crystals are presented. X-ray photoelectron spectroscopy (XPS) and atomic force microscopy (AFM) have been used to obtain information about the stoichiometry and uniformity of $ATiO_3$ [A=(Ba or Sr)] structures after extensive thermal treatment. Surface deterioration has been observed and drastic change of the cationic stoichiometry was measured in the near-surface region.

3.4.1 Introduction

As described in the first chapter (I.2.4), several well described mechanisms may affect the stoichiometry near the surface of $ATiO_3$ perovskites, such as segregation of AO under oxidizing or reducing conditions, for instance well observed in single crystals of $SrTiO_3$ [60]. Similar behaviour has been reported for $SrRuO_3$ thin films [61], donor-doped $SrTiO_3$ single crystals [62], undoped $SrTiO_3$ single crystals [63] and $KTaO_3$ single crystals [64]. Table I summarizes the different observations and the methods used.

table 1

system investigated	observations	method	ref
epitaxial thin film of $SrTiO_3/SrRuO_3$	significant excess of SrO upon reduction and oxidation at the surface	XPS, AFM XRD	61
donor-doped (La) $SrTiO_3$ single crystal	formation of precipitates at the surface after oxidation, depending on the amount of dopant.	Optical images microscopy	62
undoped $SrTiO_3$ single crystal	agglomeration of SrO precipitates after prolonged annealing (120h)	AFM	63
undoped $BaTiO_3$ ceramic and $KTaO_3$ single crystals	reversible process of defect segregation after redox treatment.	XRD	64
Nb-doped $SrTiO_3$ ceramic	The formation of precipitates at the surface is depending on the surface orientation of the corresponding grain.	Optical micrograph, AFM	65

This section will focus on *oxidation* study of Nb-doped and undoped epitaxial $BaTiO_3$ films. Ceramics of La-doped (0.02 wt %) $BaTiO_3$, and Nb-doped $SrTiO_3$ (0.05 wt %) single crystals have also been studied for comparison with thin films. A correlation between the core-level changes (mostly barium, strontium and oxygen core-levels) has not been reported so far. This work will thus clarify the evolution of peak shape with respect to the thermal treatment.

3.4.2 Experimental approach

$BaTiO_3$ thin films were grown on conducting $SrTiO_3$:Nb substrates under similar conditions than those described in section III.3.1.1. Sputtered undoped and Nb-doped $BaTiO_3$ thin films (0.05 wt %) have been used to investigate the potential segregation and to eventually identify an influence of doping, as reported for La-doped $SrTiO_3$ single crystals [62]. As recalled in chapter I, La^{3+} substitution at the Ba^{2+} site of $BaTiO_3$ as similar effects on the conduction properties as Nb^{5+} substitution at Ti^{4+} site in $BaTiO_3$ and $SrTiO_3$. This is why $BaTiO_3$:La ceramics were also investigated here.

Thin-films, ceramics and single crystals were annealed under oxidizing conditions at 1000°C during 16h ex-situ using a constant oxygen flux during the heating and the cooling (10K.min^{-1}). After thermal treatment, the samples were introduced in the Ultra-High-Vacuum (UHV) system for surface cleaning prior to the measurement. To achieve that, moderate thermal treatment (450°C) were performed under oxygen partial pressure of pO_2=0.05 Pa for the oxidized samples. Preliminary experiments have shown that moderate temperature does not modify the oxidation states of $ATiO_3$ compounds but rather promote the removal of hydrocarbons (see figure 3.4.1 and also [49]). After surface cleaning, the different samples were in-situ transferred to the analysis chamber for photoemission measurements under different take-off angles. We recall that ion bombardment was never used to clean the samples during these ex-situ XPS experiments to prevent the Ti from reduction (Ti^{4+} → Ti^{3+}).

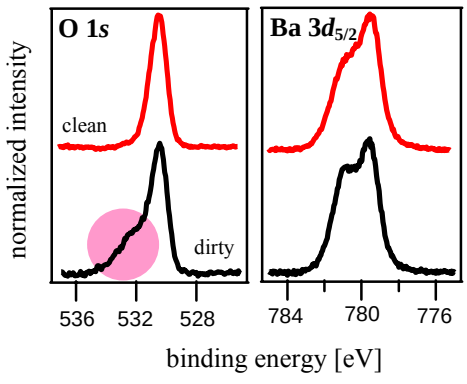

Figure 3.4.1: O 1s and Ba $3d_{5/2}$ levels of c $BaTiO_3$ ceramic. The black spectra were recorded without surface cleaning. Moderate thermal treatment can remove the surface contaminants and thus cancel the extra component (disk).

3.4.3 Oxidation treatment and discussion

In order to study the potential segregation of $ATiO_3$ perovskite structures, the core-levels of $BaTiO_3$ thin films, $SrTiO_3$ single crystal, and ceramics of $BaTiO_3$ have been measured by photoemission spectroscopy. This paragraph will describe the chemical and electronic properties under prolonged thermal annealing under high oxygen partial pressure. Different takeoff angle of measurements were used for thin films and single crystal analyses since their flat surfaces are particularly suitable to determine the compositional profile. In contrast, the angle dependence can not be employed for polycrystalline materials due to higher roughness. Figure 3.4.2 show the Ba $3d_{5/2}$, O 1*s*, Ti 2*p*, and valence band (VB) spectra of Nb-doped $BaTiO_3$ thin films. As a reference, the core-levels recorded before thermal annealing are also reported and named *as grown*. The takeoff angles used during the data collection are also aligned in the graph. All the reported spectra have been normalized to their maximum intensities for comparison. Figure 3.4.2 shows the core levels of Ba $3d_{5/2}$ and Sr 3*d* of undoped and Nb-doped $BaTiO_3$ thin films, polycrystalline La-doped $BaTiO_3$, and Nb-doped $SrTiO_3$ single crystal before and after oxidation treatment.

One can see in the Ba emission, two peaks denoted Ba1 and Ba2 on the spectra. They are already present prior to the annealing.

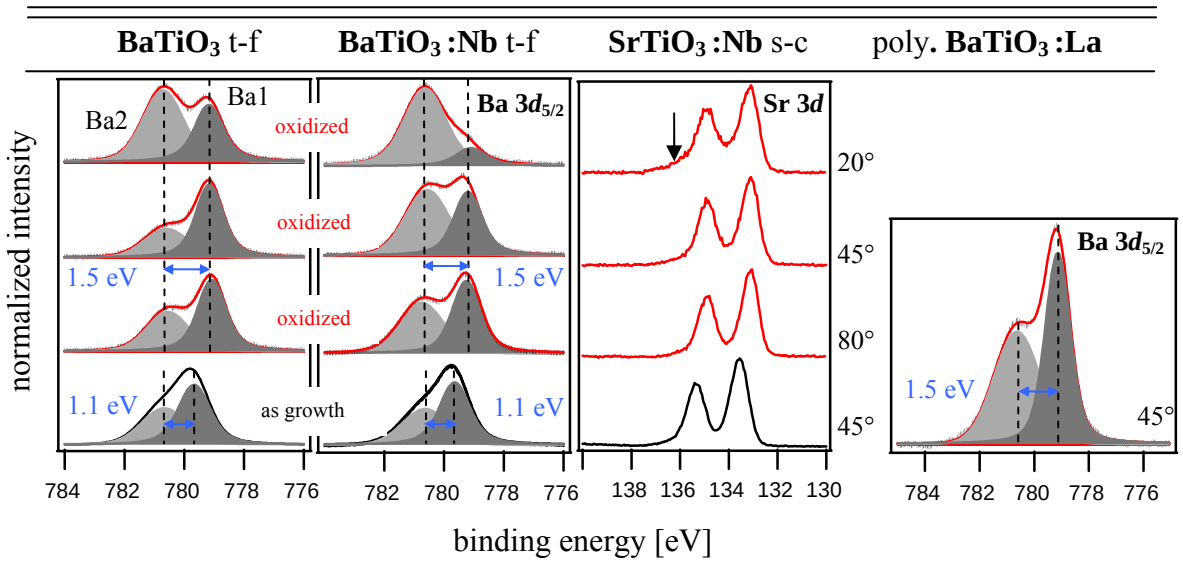

Figure 3.4.2: Ba $3d_{5/2}$ and Sr 3*d* core levels spectra recorded for the different systems mentioned above their respective frame at different takeoff angles. The intensities have been normalized to the maximum peak for comparison. Ba2 (light gray) increases subsequently at the surface. Noted that Ba2 is particularly important for Nb:BTO t-f. After oxidation, the binding energy difference Ba2 – Ba1 is increased to 1.5 eV for $BaTiO_3$ composition. Clear Sr shoulder is visible at higher binding energy for STO s-c sample. No changes have been observed in the Ti core-levels and are thus not reported.

As evidenced in the spectra, the Ba spectra exhibit a second barium component (light gray). As expected, oxygen thermal treatment increases the binding energy difference Ba2 – Ba1 to 1.5 eV (as growth = 1.1 eV for thin films). The same binding energy difference is observed for oxidized La-doped $BaTiO_3$ ceramic after oxidation. Higher Ba2 intensity for the Nb-doped thin film compared to the undoped film is evident from Figs. 3.4.2 and 3.4.3.

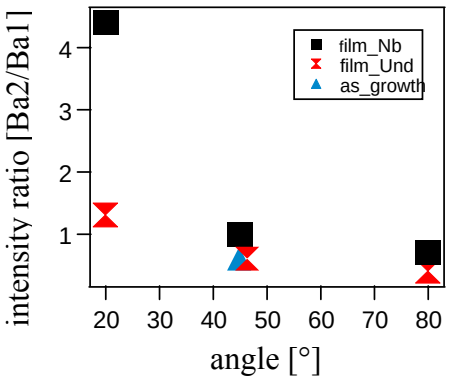

Figure 3.4.3: Intensity ratio of Ba2/Ba1 for thin films at different takeoff angles, derived from the Ba emission of Fig. 3.4.6 after oxidation. Ba2 is much higher at low angle for Nb:doped BTO t-f. For the *as grown* state, the intensity ratio of Ba2/Ba1 is similar for doped and undoped thin films and is indicated by one blue dot.

The Sr 3*d* level also exhibits a second component at higher binding energies at low angle of measurements. A second component of the Sr 3d level has also been observed by Baniecki et al. on BST thin films [66]. But the mechanism leading to the Sr splitting might have a different origin than the corresponding splitting of the Ba levels. Brookes *et al.* [67] have demonstrated a surface core-level shift (SCLS) in the very-near surface region of $SrTiO_3$ materials. In the Ba levels, the intensity of Ba2 is too high and remains largely visible at higher angle, excluding a pure SCLS effect.

By inspecting the O 1*s* of the corresponding samples (Figure 3.4.4), it is clear that an oxygen shoulder appears for all these samples at higher binding energy, especially at low angle where the Ba2 component is dominant. This shoulder is strongly apparent for single crystal and polycrystalline samples. The binding energy difference between these shoulders and the Ba2 component are found to be ~248.5 eV, corresponding to BaO bonding as shown for the Nb-doped BTO in Fig. 3.4.5. It would also be nice to measure a standard SrO sample to quantify the same binding energy difference between the oxygen shoulder and the second Sr component visible at low angle. The surface enrichment of BaO is expected to modify the cationic Ti/Ba ratio, particularly at low angle. In fact, this is exactly what we have observed, as reported below in the table II.

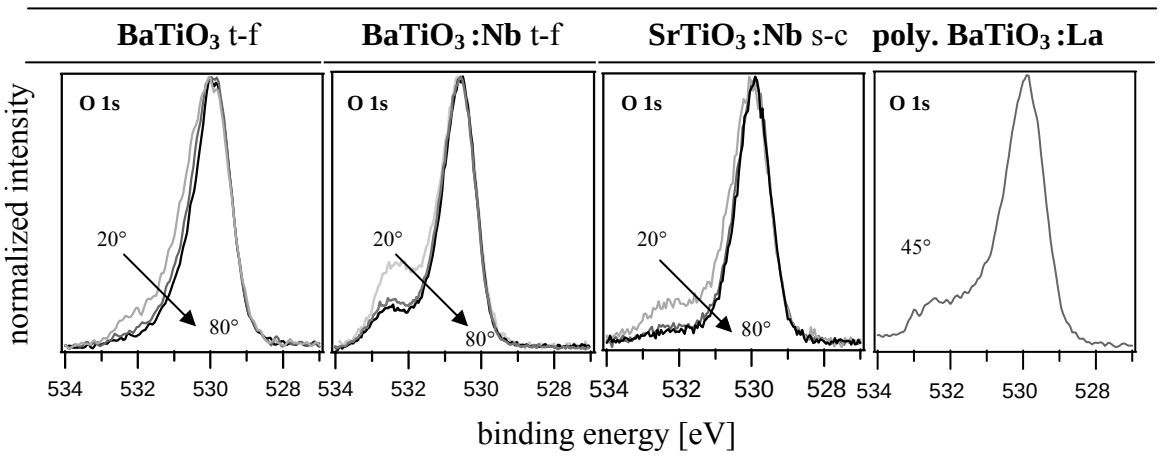

Figure 3.4.4: O 1*s* core levels for thin films, single crystal and ceramic of $ATiO_3$ materials. The intensities have been normalized to the maximum peak for comparison. In all these samples, a clear oxygen shoulder appears at higher binding energy under oxidation treatment. The doped materials have higher O shoulders. The binding energy differences between the corresponding Ba2 positions and these shoulders are similar to BaO bonding (248.5 eV), as discussed in the text.

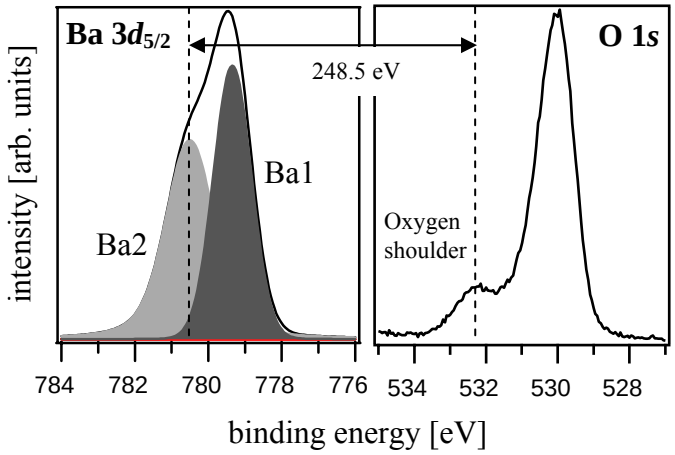

Figure 3.4.5: Ba 3*d*5/2, and O 1*s* spectra recorded from Nb-doped BTO sputtered thin films after oxidation. Example is taken from this sample to highlight the energy separation between Ba2 and the oxygen shoulder corresponding to BaO bonding.

Table II – Cationic ratio **Ti/Ba** derived from XPS after **oxidation**

θ	$BaTiO_3$ t-f	$BaTiO_3$:Nb t-f	$SrTiO_3$:Nb s-c	Poly. $BaTiO_3$:La
80°	0.8	0.95	0.8	–
45°	0.8	0.9	0.8	0.6
20°	0.87	0.5	0.7	–
untreated : 45°	1.2	1.1	0.8	0.8

Table II gives evidence for noticeable Ba enrichment, especially at low angle of measurement. Therefore, for thin films and polycrystalline La-doped BTO, we can assume that oxygen-rich annealing is responsible to Ba enrichment at the surfaces via formation of BaO species.

We note that no Ti enrichment is observed at the surface of La-doped $BaTiO_3$ ceramic for the untreated state as well as after oxidation. It might contradict the model of Ti-vacancy compensation for La-doping as detailed in chapter I.2.

The valence band spectra are presented in Figure 3.4.6. The observed tendency after oxidation is a general lowering of the VBM binding energies, corresponding to lower Fermi energy positions. This trend is expected when oxygen vacancies are removed after oxygen treatment decreasing thus the charge carrier density, principally governed by the oxygen activity in ABO_3 compounds. Typical electrical measurements usually support higher insulating character in $ATiO_3$ compounds after oxidation. However, the presented valence band emissions are a direct evidence of higher insulating character through lower Fermi level.

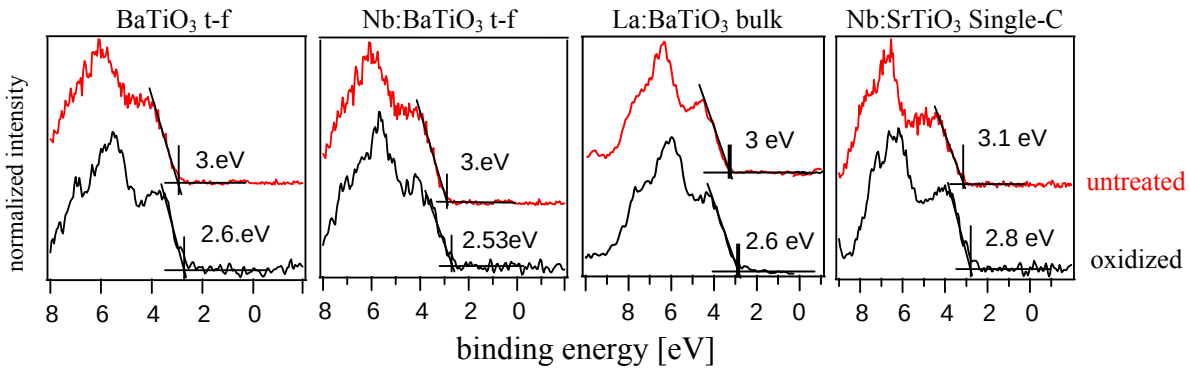

Figure 3.4.6: X-ray valence band spectra for thin films, ceramic, and single crystal used in the present study. Lowering of the Fermi level is evident after oxidation for all these systems.

Under strong oxidizing conditions, the segregation of BaO at the surface may lead to sizeable grain growth. Thus, to study the surface morphology after annealing treatment, we have performed Atomic Force Microscopy (AFM) on thin film samples. A roughness of ~2 nm was measured for both films after deposition (as grown state). However, large grains appear at the surfaces after subsequent oxidation as shown in Figure 3.4.7 for undoped and Nb-doped $BaTiO_3$ thin films. This behaviour is in agreement with the features observed by Szot *et al.* on $SrTiO_3$ single crystals after prolonged oxidation (see also § I.2.4). Magnification of one droplet indicates a well faceted single crystal-like morphology. Surprisingly, their measured heights exhibit values of around 100-150nm, half of the film thickness. Such features were not observed with the Nb-doped $SrTiO_3$ single crystal in contrast to literature [69]. This suggests that the grain formation require higher and/or longer thermal treatment for surface

crystallite formation than performed in this work. Also the occurrence of grain boundaries in polycrystalline materials films may help the nucleation and growth of such crystallites thanks to the grain boundaries selective out-diffusion of Barium.

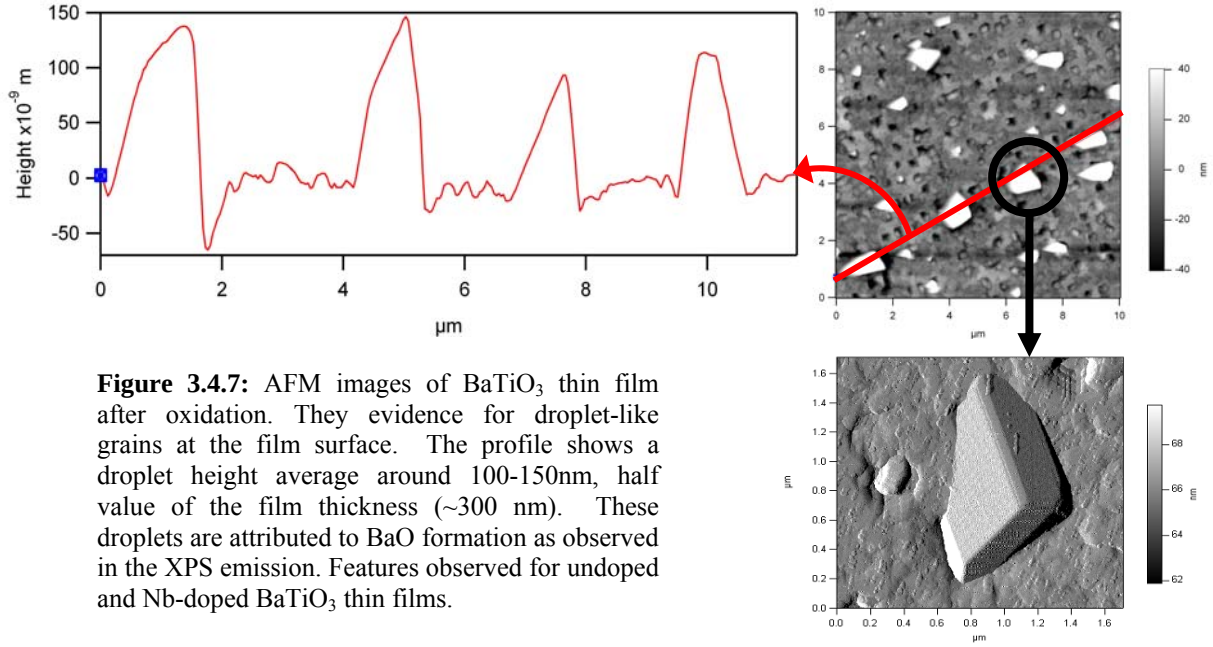

Figure 3.4.7: AFM images of $BaTiO_3$ thin film after oxidation. They evidence for droplet-like grains at the film surface. The profile shows a droplet height average around 100-150nm, half value of the film thickness (~300 nm). These droplets are attributed to BaO formation as observed in the XPS emission. Features observed for undoped and Nb-doped $BaTiO_3$ thin films.

3.4.4 Summary

In summary, the results show that the surface of $BaTiO_3$ is subjected to important modifications from the initial state under extensive thermal treatment, as probed by XPS and AFM measurements. Two identical experiments have been performed showing the reproducibility of the results. Subsequent BaO formation has been observed in the near surface region. The binding energy differences between Ba2 and the oxygen shoulders are exactly corresponding to BaO bonding, as deduced from standard BaO powder. When the takeoff angles is decreased (surface sensitive), Ba2 and the oxygen shoulders increase subsequently for all the investigated samples denoting a clear tendency of surface Ba segregation. The cationic stoichiometry derived from XPS calculations confirms large Ba enrichment at the surface. This enrichment occurs by the formation of micro-crystals as indicated by AFM. All these observations seem to be more pronounced for Nb-doped thin films. The doping effect might enhance the Ba segregation velocity if we assumed that Nb^{5+} is

principally compensated by barium vacancies ($V_{Ba}^{''}$) to counter-balance the resulting extra charge Nb^{5+}/Ti^{4+}. Our experiments might thus be a direct evidence that ionic compensation of donor dopant La^{3+} or Nb^{5+} goes through Ba^{2+} vacancies which is of technological interest but still matter of debate in the recent literature as detailed in chapter I.2. We do not see Ti enrichment at the surface of La-doped ceramics when thermally untreated which contradicts the model of Ti-vacancy compensation for La-doped $ATiO_3$ [71]. Ionic compensation via barium vacancy is thus strongly suggested regarding the potential of Ba-segregation in donor doped materials.

Multilayer-type arrangements of different Ruddlesden-Popper phases were also suggested to occur (see e.g. [61]). Ruddlesden-Popper phases evolve from insertion of (AO) planes between perovskite $ATiO_3$ layers of various thicknesses [70] (see also chap **I**.2.2, Figure 1.2.6). In such intercalation (AO) does not represent a separate phase but a structural accommodation. So far, no evidence has been provided in the literature to confirm this mechanism.

Explanation about the second barium component (Ba2) is not entirely clear since Ba2 is already observed before thermal treatment (when Ti-rich). Subsequent oxygen annealing increase considerably Ba2 through BaO formation but the observed extra component is in fact the sum of two contributions (BaO + unknown contribution) after oxidation. The unknown contribution in the Ba emission (visible when as deposited) is discussed in the next paragraph.

3.5 The barium components

In this section, the barium components observed in the photoemission spectra are discussed. The lower binding energy peak, throughout this work denoted as Ba1, is clearly assigned to Ba atoms in the perovskite phase whereas the higher binding energy component Ba2 has been found to be surface related. The origin of Ba2 will be discussed. Different cationic ratio (Ba/Sr) in (Ba,Sr)TiO_3 thin films, can change the Ba emission spectra. Amorphous $BaTiO_3$ do not exhibit a surface barium component. The results are discussed regarding possible electronic origin, or change in the Ba-coordination in the near-surface region.

3.5.1 Introduction

Since the first photoemission spectroscopy paper on $BaTiO_3$ [13], the XPS Ba emissions have been subjected to several interpretations such as surface core level shift [15,66], barium carbonate formation ($BaCO_3$) [72], non-perovskite surface layer [73], oxygen vacancies effect [74,75], smaller surface electron density [16] or even due to surface polarization charges [76]. The two different chemical states of Ba were observed in thin films [16,66,74] and ceramic materials [13,15,76]. Addition of acceptor dopants (Fe) or donor dopants (Nb) in ceramics of $BaTiO_3$ were not found to change the Ba2 component [22]. It also appears that the surface treatments performed prior to the analysis can considerably affect the Ba emissions [66,74,76]. Baniecki *et al.* have shown that BST films subjected to $H_2O/H_2O{:}HNO_3$ treatments causes a large suppression in the intensity of Ba2 [66] as well as subsequent Ar ion sputtering [74], whereas surface polishing increases Ba2 [76]. Thermal annealing can also affect the Ba core levels as described in section 3.4 of chapter III. The binding energy difference of Ba1 and Ba2 was found to be separated by 1.5 eV±0.1 eV in most of the publications mentioned above. Finally, we have to mention that Sr line shape is also described by two overlapping spin-orbit-split (SOS) pairs in $SrTiO_3$ materials [15,66]. Angle-resolved XPS also demonstrated the surface nature of the second Sr emissions. However, the observed Ba2 intensities are much more intense than the Sr2, suggesting different mechanisms between both cations as discussed below.

3.5.2 Results

The higher binding energy pair (Ba2) was first attributed to Ba atoms in a carbonate phase [72]. However Ba2 is still observable in $BaTiO_3$ thin-films deposited and analyzed *in-situ*. Therefore, we can reasonably exclude such extra phase. As discussed before, it is also very unlikely to involve surface core-level shift effect for the Ba emissions as observed in the Sr levels. The Ba 4*d* and Sr 3*d* levels in dependence of the photon energy are shown Figure 3.5.1.

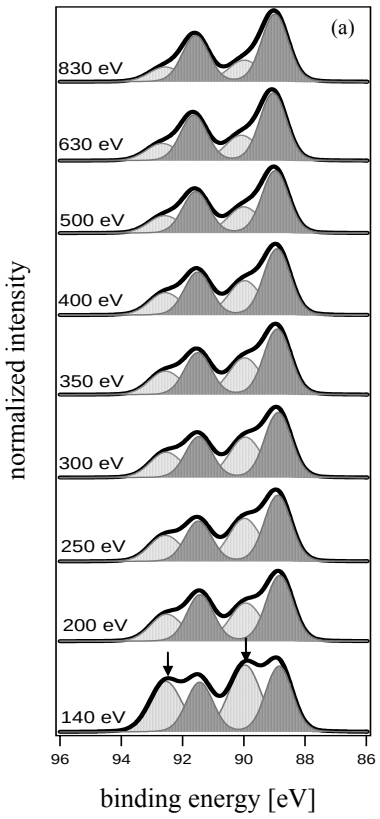

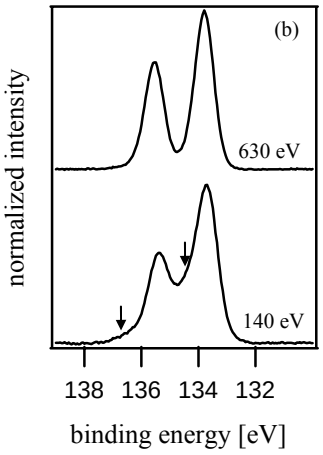

Figure 3.5.1: (a) Background subtracted Ba4d emission of $BaTiO_3$ thin films with varying excitation energy. All the intensities are normalized to the maximum. The light gray colour denotes the surface species and the dark gray, the bulk components. The binding energy difference between both components has been constrained to 1.1eV. For comparison, the Sr 3*d* core levels is also shown in (b) with two similar excitation energy for STO single crystal. The splitting of Ba is much more pronounced than Sr for a given excitation energy.

Two barium components are clearly observed, Ba1 at 88.9 eV and Ba2 at 90 eV. The intensity of Ba2 is reduced with respect to Ba1 with increasing excitation energy, thus probing Ba1 located deeper in the film. In Figure 3.5.2 is plotted the intensity ratio Ba2/Ba1 derived from Fig. 3.5.1. Using a simple bi-layer model illustrated figure 3.5.3, we can estimate the thickness of the surface layer containing Ba2 to 0.5 nm. The calculated mean-free-path (λ) was used according Tanuma, Powell, and Penn using parameters for Al_2O_3 [77].

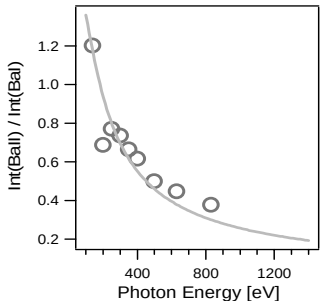

Figure 3.5.2: Ratio of the surface-to-bulk components derived from Fig. 3.5.1(a) plotted versus the photon energy. The solid line is a fit using a bi-layer model describes in figure 3.5.3.

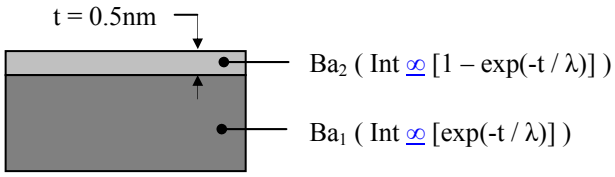

Figure 3.5.3: Simple bi-layer model, the surface layer (clear gray) is supposed to contain only the surface species Ba2. The mean free path (λ) for the electrons has been proposed by Tanuma, Powell and Penn and used in this calculation. The surface layer thickness calculated is ~5 Å.

All the presented spectra were recorded at room temperature. $BaTiO_3$ is ferroelectric at T_{room} so one can not exclude a ferroelectric effect arising from sub-polarized layer. When BTO is not covered by a metal electrode, one can assume an uncompensated state as exemplified in Fig. 3.5.4 (a), leading to surface polarization which can be screened by metal deposition (b). By speculating that these polarization charges occur in our films, they could disturb the electronic levels of Ba inducing thus Ba2. Using the Landau–Devonshire theory including a surface term, Binder [78] has shown a decrease of polarization in the vicinity of the surface arising from polarization non-uniformity. A proposed diagram is shown in Fig. 3.5.5, unifying the Binder model and the observed Ba emission.

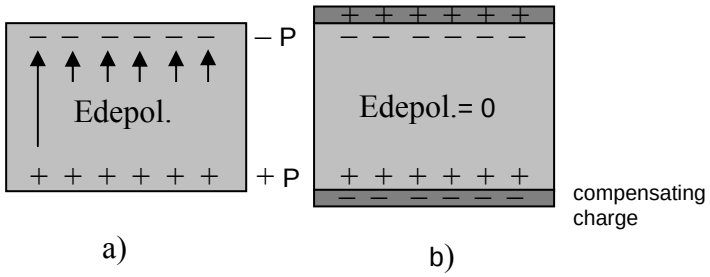

Figure 3.5.4: (a) A depolarization field (Edepol.) arises in an isolated ferroelectric, due to uncompensated polarization charges (P) on opposite faces of the material. (b) Metal electrodes provide a source of compensating charges, which cancel Edepol.

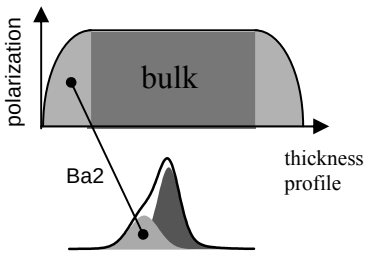

Figure 3.5.5: Polarization profile vs. the film thickness according Binder [12]. Boundary conditions give rise to a decrease of P. A correlation is suggested between polarization gradient and Ba2

If we now assume that Ba2 is due to a depolarization effect, one can expect a modification of the Ba emission under metal deposition according Fig. 3.5.4 (b). In fact this is exactly what we observed during Pt deposition as shown in figure 3.5.6. The energy separation between Ba2 and Ba1 is reduced with respect to the Pt deposition time. The metal provides therefore the compensating charges to screen the polarized surface leading to a lowering of the energy separation.

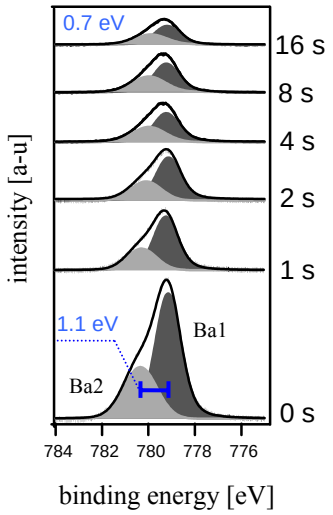

Figure 3.5.6: The Ba $3d_{5/2}$ core level during Pt deposition. The Pt deposition time is indicated in second. Energy separation between surface and bulk component decreases with Pt deposition. Before deposition, the corresponding O 1*s* level does not indicate BaO bonding.

To ensure that Ba2 is related to ferroelectricity, we have measured the Ba levels of $Ba_{1-x}Sr_xTiO_3$ compositions with varying *x* (0, 0.4, 0.5, 0.9) of sputtered thin films. Each composition corresponds to the stoichiometry of the sputtered target. Since strontium substitution in $BaTiO_3$ lattice lowers the Curie temperature of the cubic to tetragonal transition in bulk ceramics [79], a pure paraelectric state is expected for small amount of Ba (e.g. T_c = 50K for x = 0.9) at room temperature. Surprisingly, whereas a lowering of Ba2 was expected for small amounts of Ba (paraelectric state), we have observed an increase of Ba2 with increasing *x* as shown in Figure 3.5.7. To obtain reasonable fit, the energy separations of Ba1 ─ Ba2 were not constrained to the same value. Thus, an increase of this separation is observed by decreasing the Ba content. A clear oxygen shoulder is concomitantly observed for $Ba_{0.1}Sr_{0.9}TiO_3$ composition. No additional O peaks are evidenced for the other compositions whereas Ba2 is still visible. The presented spectra were recorded on polycrystalline BST deposited onto polycrystalline Pt using the same deposition conditions for all the compositions. There is, however, no guarantee that the deposition conditions used for $Ba_{0.1}Sr_{0.9}TiO_3$ are as appropriate as they are for $BaTiO_3$. This is indeed suggested by the oxygen shoulder occurrence. Thus, it is difficult to attribute Ba2 with a possible electronic

effect or BaO formation whereas both can occur in thin films not deposited under optimal conditions. However, this result does not support an influence of ferroelectricity on the occurrence of the second Ba component. The disappearance of Ba2 would be expected at small Ba concentrations to corroborate this effect.

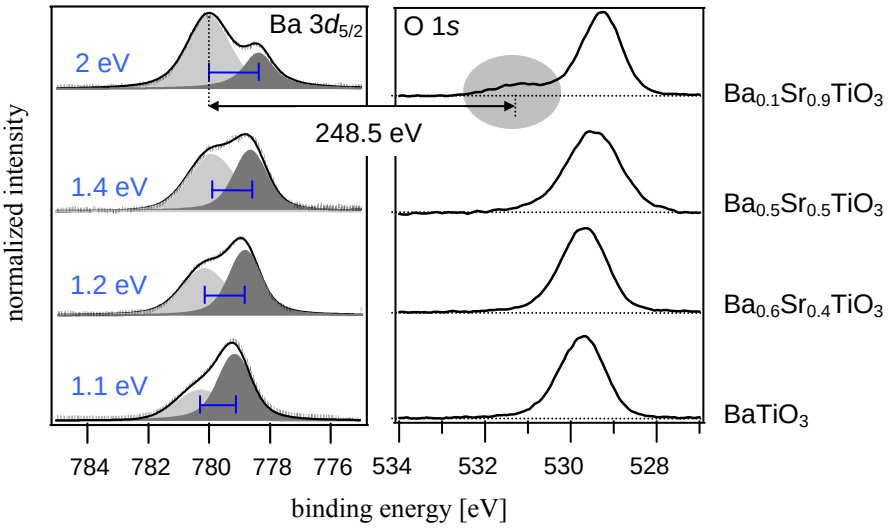

Figure 3.5.7: Ba $3d_{5/2}$ and O 1*s* core levels of $Ba_{1-x}Sr_xTiO_3$ thin films deposited onto Pt. By decreasing the amount of Ba (increasing x), the surface barium component increases as well as the energy separation. For $Ba_{10}Sr_{90}TiO_3$, an important oxygen shoulder is observed. The binding energy difference between Ba2 and the corresponding O shoulder corresponds to BaO bonding (248.5 eV). No obvious oxygen shoulders are observed for the other compositions.

We have also investigated the contact formation of Pt and post-deposition ex-situ oxidized $BaTiO_3$ thin films (see Fig. 3.5.8). As described in section **III**.3.4, extensive oxygen annealing induces BaO formation at the surface of $BaTiO_3$. After this treatment, the Ba levels are thus constituted of BaO and $BaTiO_3$ bonding as shown in figure 3.5.8. Before metal deposition, the Ba $3d_{5/2}$ level exhibits the two components corresponding to BTO and BaO separated by 1.5 eV. Similarly to Fig. 3.5.6, the Pt deposition affects the energy separation between Ba2 and Ba1 although the uncovered $BaTiO_3$ surface shown in Figure 3.5.8. do not show any obvious BaO bonding. This suggests that Pt deposition also induces a decrease of the energy separation when Ba2 is well identified as BaO compound.

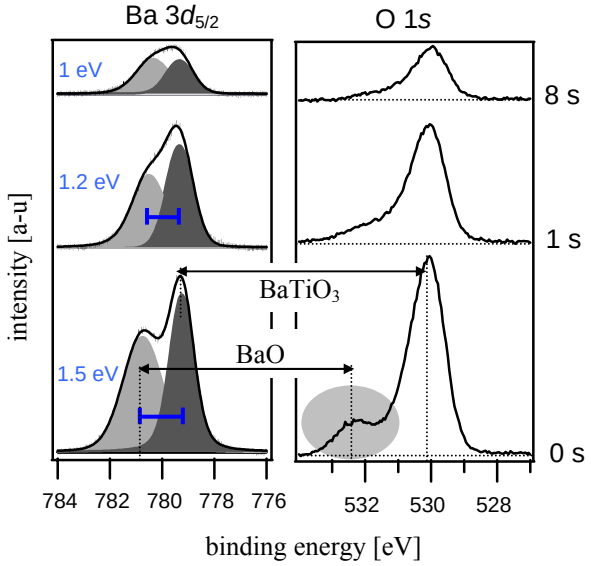

Figure 3.5.8: The Ba $3d_{5/2}$ and O 1s core levels during Pt deposition of BTO thin film highly oxidized. The Pt deposition time is indicated in second. Energy separation between BaO and bulk components also decreases with Pt deposition as in the case of BTO without apparent BaO bonding (see Fig. 3.5.6).

In this context, the measurement of $BaTiO_3$ single crystal can also help to identify the origin of the second barium component. To avoid charging effect, the single crystal must be conducting enough, e.g., using doped sample. We have thus measured the surface properties of Nb-doped $BaTiO_3$ single crystal (Nb: 0.02 wt %). The sample was first cleaned by heating at moderate temperature (400°C) in 1 Pa oxygen to remove the typical hydrocarbon contaminations from ambient conditions. The XPS spectra are displayed in Fig. 3.5.9.

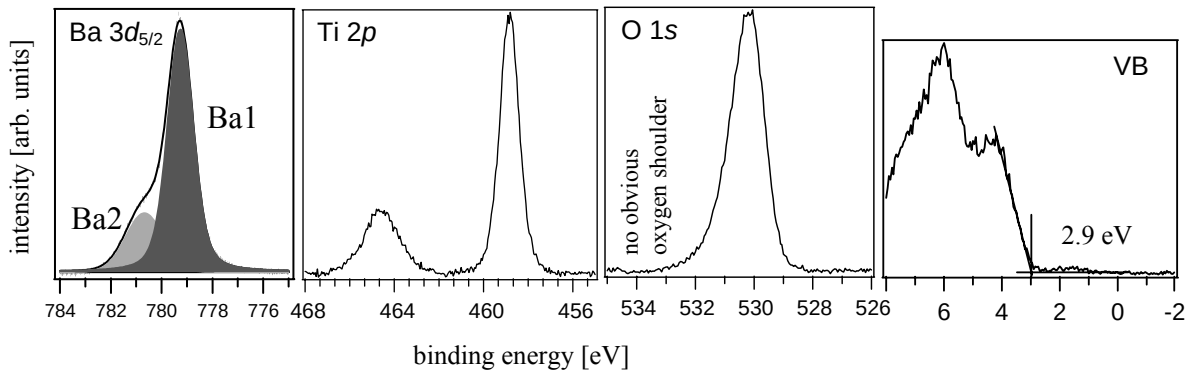

Figure 3.5.9: XPS core-levels recorded from Nb-doped $BaTiO_3$ single crystal (0.02wt% of Nb). As evident from the Ba emission, the surface Ba component is still largely observable. Furthermore, no obvious oxygen shoulder could be observed from the O 1s level. The calculated energy separation between both Ba components is ~1.4 eV. The intensity of Ba2 is obviously lower than those observed in thin film form.

It is clear from the spectra that Ba2 is still visible at the surface of Nb:BTO single crystal. The Ba2 emission seems however to be different than those observed in thin films form. Indeed, the deconvolution of both spectra leads to an energy separation of ~1.4 eV between Ba2─Ba1 whereas thin films of BTO have lower value (~1.1eV). The intensity ratio between Ba2/Ba1 is

also radically lower in the single crystal (~0.24) than those observed for numerous thin films (~0.6). Finally, no oxygen shoulder is evidenced confirming that Ba2 is not ascribed to BaO formation.

3.5.3 *Summary*

The origin of the barium component remains still unclear. Therefore, only speculative explanations can be given from the available data. This justifies position of this section at the end of the manuscript. The intensity ratio and the energy separation between surface and bulk components are sensitive to several factors making the interpretation difficult. If Ba2 is clearly surface related, it is however not clear why the splitting change under metal deposition, and between thin film and single crystal. Since our samples are expected to be in ferroelectric phase at the operating temperature of measurement, electronic origin through screening effect might be a possible explanation. This would at least explains the difference observed between $SrTiO_3$ (paraelectric at T_{room}) and $BaTiO_3$ (ferroelectric at T_{room}), as well as the modification of Ba2 with metal deposition. The presence of sub-polarized layer might thus induce Ba2. However, when the amount of Ba decreases for BST compositions, the Ba2 content increases with respect to Ba1. This is in contradiction with polarization effect as residual ferroelectric domains must be cancelled at low Ba concentrations.

If a subsequent oxidative thermal treatment is performed, Ba2 can be identified as BaO bonding. However Ba2 is still largely observed although BaO is not formed as observed in the single crystal of $BaTiO_3$:Nb.

3.6 Literature

[1] J. Im, O. Auciello, P.K. Baumann, S.K. Streiffer, D.Y. Kaufman, and A.R. Krauss. (2000), *Appl. Phys. Lett.*, **76**, 625-627.

[2] R. Schafranek, A. Giere, A.G. Balogh, T. Enz, Y. Zheng, P. Scheele, R. Jakoby, and A. Klein. (2009), *J. Europ. Ceram. Soc.*, **29**, 1433.

[3] V. Reymond. (2007), Thesis, University of Bordeaux.

[4] C. Noguera. (2000), *J. Phys. Cond. Mat.*, **12**, R367.

[5] J. Goniakowski, F. Finocchi, and C. Noguera. (2008), *J. Phys. Cond. Mat.*, **71**, 016501.

[6] S.M. Sze. *Physics of semiconductor Devices* (Wiley, New York, 1981).

[7] R. Meyer, R. Waser, J. Helmbold, and G. Borchardt. (2002), *J. Electroceram.* **9**, 101.

[8] K. Szot, and W. Speier, (1999), K. Szot, and W. Speier. (1999), *Phys. Rev. B.* **60**, 5909.

[9] A. Thissen, *Thesis*, (2000), Untersuchung der geometrischen und der elektronischen Struktur ul-tradünner Kalium- und Natriumschichten auf SrTiO3 (001)-Oberflächen mit Photoelektronenspektroskopie, Gerhard-Mercator-Universität Duisburg.

[10] J.F. Moulder, W.F. Stickle, P.E. Sobol, and K.D. Bomben. (1995), *Handbook of X-ray Photoelectron Spectroscopy*, Phys. Elect., Eden Prairie.

[11] G.K. Wertheim, and S.B. DiCenzo. (1988), *Phys. Rev. B.* **37**, 844.

[12] R. Schafranek, S. Payan, M. Maglione, and A. Klein. (2008), *Phys. Rev. B.* **77**, 195310.

[13] B. Cord, and R. Courths. (1985), *Surf. Sci.* **152**, 1141.

[14] J.D. Baniecki, M. Ishii, T. Shioga, S. Miyahara, and K. Kurihara. (2006), *Appl. Phys. Lett.* **89**, 162908.

[15] L.T. Hudson, R.L. Kurtz, S.W. Robey, D. Temple, and R.L. Stockbauer. (1993), *Phys. Rev. B.* **47**, 16.

[16] X.L. Li, B. Chen, H.Y. Jing, H.B. Lu, B.R. Zhao, Z.H. Mai, and Q.J. Jia. (2005), *Appl. Phys. Lett.* **87**, 222905.

[17] R. Schafranek, A. Klein. (2006), *Solid State Ionics.* **177**, 1659.

[18] R. Schlaf, A. Klein, C. Pettenkofer, and W. Jaegermann. (1993), *Phys. Rev. B.* **48**, 14242.

[19] A. Klein, C. Pettenkofer, W. Jaefermann, M.C. LuxSteiner, and E. Bucher. (1994), *Surf. Sci.* **321**, 19.

[20] R. Schafranek, A. Wachau, C. Korber, and A. Klein. (2009), unpublished result.

[21] D.Y. Wang. (1994), *J. Am. Ceram. Soc.* **77**, 897.

[22] H. Jena, V.K. Mittal, S. Bera, S.V. Narasimham, K.V. Govindan Kutty, and T.R.N. Kutty. (2008), *Appl. Surf. Sci.* **254**, 7074.

[23] E. Arveux, S. Payan, M. Maglione, and A. Klein. (2009), to be published.

[24] D.M. Smyth. (2000), *Solid State Ionics.* **129**, 5.

[25] D.R. Turner, and H.A. Sauer. (1959), *J. Electrochem. Soc*. **107**, 3. p250.

[26] S.S. Flaschen, and L.G. Van Uitert. (1956), *J. Appl. Phys.* **27**, 190.

[27] D.P. Cann, and C.A. Randall. (1997), *J. Mater. Res.* **12(7)**, 1685.

[28] W.J. Heywang. (1971), *Mater. Sci.* **6**, 1214.

[29] J.K. Song, *et. al.* (2008), *J. Ceram. Proc. Res.* **9**, 292.

[30] Y. Gassenbauer, A. Klein. (2006), *J. Phys. Chem.* **110**, 4793.

[31] F. Parmigiani, E. Kay, and P.S. Bagus, (1990), *J. Electr. Spectr. Rel. Phen.* **50**, 39.

[32] L.T. Hudson, R.L. Kurtz, S.W. Robey, D. Temple, and R.L. Stockbauer, (1993), *Phys. Rev. B.* **47**, 1174.

[33] P. Pertosa, and F.M. Michel-Calendini, (1978), *Phys. Rev. B.* **17**, 2011.

[34] S. Matsushima, S. Kohiki, and M. Oku, (2000), *J. Ceram. Soc. Jap.* **108**, 952.

[35] H. Thomann, *Ferroelectrics*. (1987) **73**, pp. 183-199.

[36] J. Junquera, M. Zimmer, P. Ordejon, and P. Ghosez., (2003), *Phys. Rev. B.* **67**, 155327.

[37] F. Amy, A.S. Wan, A. Kahn, F.J. Walker, and R.A. McKee., (2004), *J. Appl. Phys.* **96**, 1635.

[38] K. Abe, S. Komatsu, N. Yanase, K. Sano, and T. Kawakubo., (1997), *Jpn J. Appl. Phys.* **36**, 5846.

[39] C.B. Eom, J.Z. Sun, K. Yamamoto, A.F. Marshall, K.E. Luther, and S.S. Laderman, (1989), *Appl. Phys. Lett.* **55**, 595.

[40] J.M. Triscone *et. al.* (1996), *J. Appl. Phys.* **79**, 4298.

[41] J. Maserjian. (1969), *J. Vac.Sci. Technol.* **6**, 5.

[42] G.H. Jonker. (1964), *Sol. Stat. Electron.* **7**, 895-903.

[43] D. Nagano, H. Funakubo, K. Shinozaki, and N. Mizutani. (1998), *Appl Phys. Lett.* **16**, 2017-2019.

[44] N. Lemée, C. Dubourdieu, G. Delabouglise, J.P. Sénateur, and F. Laroudie. (2002), *J. Crys. Grow.* **235**, 347-351.

[45] H. Z. Guo, L.F. Liu, H.B. Lu, Y.Y. Fei, W.F. Xiang, Y.L. Zhou, and Z.H. (2004), *Chin. Phys. Lett.* **21**, 396-399.

[46] L. Yan, H. Lu, Z. Chen, S. Dai, Y. Zhou, and G. Yang. (2002), *J. Crys. Grow.* **244**, 225-228.

[47] Y. Sasaki, I. Fujii, T. Matsui, and K. Morii. (1995), *Mat. Lett.* **26**, 265-271.

[48] Y. Shao, R.A. Hughes, A. Dabkowski, G. Radtke, W.H. Gong, J.S. Preston, and G.A. Botton. (2008), *Appl. Phys. Lett.* **93**, 192114.

[49] Y. Gassenbauer, R. Schafranek, A. Klein, S. Zafeiratos, M. Hävecker, A. Knop-Gericke, and R. Schlög. (2006), *Phys. Rev. B.* **73**, 245312.

[50] A. Klein, and F. Säuberlich, in: *Transparent Conductive Zinc Oxide: Basic and Applications in Thin Film Solar Cells*, Eds. K. Ellmer, A. Klein and B. Rech, (Springer-Verlag, Berlin, 2008).

[51] C. Körber, and A. Klein. (2009), *Sens. Actuat. B*, doi:10.1016/j.snb.2009.03.067.

[52] D.M. Smyth. (2000), *Solid State Ionics*, , **129**, 5-12.

[53] M. Maglione and M. Belkaoumi. (1992), *Phys. Rev. B.* **45**, 2029-2034.

[54] S.B. Desu, and D. A. Payne. (1990), *J. Am. Ceram. Soc.* **73**, 33908-3406.

[55] S.B. Desu, and D. A. Payne. (1990), *J. Am. Ceram. Soc.* **73**, 3407-3415.

[56] B. Rahmati, J. Fleig, E. Bischoff, W. Sigle, J. Maier, and M. Rühl. (2005), *J. Am. Ceram. Soc.* (2005), **25**, 2211.

[57] D.M. Smyth. (2002), *J. Electroceram.*, **9**, 179-186.

[58] C.H. Wu, J.P. Chu, and S.F. Wang. (2005), *J. Appl. Phys.* **98**, 026109.

[59] J.P. Chu, C.W. Chang, T. Mahalingam, C.C. Lin, and S.F. Wang. (2003), *J. Mat. Sc. Lett.* **22**, 1269-1273

[60] K. Szot, W. Speier, J. Herion, and Ch. Freiburg. (1997), *Appl. Phys. A: Matter. Sci. Process.* **64**, 55.

[61] M. Mlynarczyk, K. Szot, A. Petraru, U. Poppe, U. Breuer, R. Waser, and K. Tomala. (2007), *J . Appl. Phys.* **101**, 023701.

[62] R. Meyer, R. Waser, J. Helmbold, and G. Borchardt. (2002), *J. Electroceram.* **9**, 101.

[63] K. Szot, and W. Speier. (1999), K. Szot, and W. Speier, *Phys. Rev. B.* **60**, 5909.

[64] K. Szot, W.Speier, M. Pawelczyck, J. Kwapulinski, J. Hulliger, H. Hesse, U. Breuer, and W. Quadakkers. (2000), *J. Phys. Condens. Matter.* **12**, 4687.

[65] B. Rahmati, J. Fleig, W. Sigle, E. Bischoff, J. Maier, M. Rühle. (2005), *Surf. Sc.* **595**, 115.

[66] J.D. Baniecki, M. Ishii, T. Shioga, K. Kurihara, and S. Miyahara. (2006), Appl. Phys. Lett. **89**, 162908.

[67] N.B. Brookes, G. Thorton, and F.M. Quinn. (1987), *Sol. stat. comm.* **64**, 383.

[68] X. Wang, U. Helmersson, L. D. Madsen, I.P. Ivanov, P. Münger, S. Rudner, B. Hjövarsson, and J.E. Sundgren. (1998), *J. Vac. Sc. Technol. A.* **17**, 564.

[69] K. Szot, W. Speier, U. Breuer, R. Meyer, J. Szade, and R. Waser. (2000), *Surf. sci.* **460**, 112.

[70] S.N. Ruddlesden, and P. Popper. (1958), *Acta Cryst.* **11**, 54.

[71] H.M. Chan, M.P. Harmer, and D.M. Smyth. (1986), *J. Am. Ceram. Soc.* **69,** 507.

[72] Y. Fujusaki, Y. Shimamoto, and Y. Matsui. (1999), *Jpn. J. Appl. Phys.* **38**, 52.

[73] J.X. Liao, C.R. Yang, J.H. Zhang, C.L. Fu, H.W. Chen, and W.J. Leng. (2006), *Appl. Surf. sc.* **252**, 7407.

[74] V. Craciun, and R.K. Singh. (2000), *Appl. Phys. Lett.* **76**, 14.

[75] M. Ihazu, K. Abe, and N. Fukushima. (1997), *Jpn. J. Appl. Phys.* **36**, 58566.

[76] S. Kumar, V.S. Raju, and T.R.N. Kutty. (2003), *Appl. Surf. Sci.* **206**, 250.

[77] S. Tanuma, C.J. Powell, and D.R. Penn. (1993), *Surf. Interf. Analys.* **20**, 77.

[78] K. Binder. (1981), *Ferroelectrics.* **35**, 99.

[79] Jaffe *et. al.* (1971), *Piezoelectric ceramics*, Academic Press, London.

Final Comments

Conclusion

The aim of this work was to better understand the properties of ferroelectric $BaTiO_3$ thin films and interfaces. The present work follows a previous thesis which was performed on non-ferroelectric $(Ba,Sr)TiO_3$ thin films by R.Schafranek [1]. In situ photoemission spectroscopy has been carried out in the surface science division at TU Darmstadt whereas dielectric measurements were performed at the ICMCB of Bordeaux in the frame of the European Multifunctional Materials Institute (EMMI).

We have first investigated the influence of sputtering conditions of $BaTiO_3$ thin films on their surface properties. In contrast to undoped $BaTiO_3$ and $(Ba,Sr)TiO_3$ thin films which exhibit typical Ti excess [1-2], Nb-doped $BaTiO_3$ have been measured with large Ba-rich surfaces (~10%) and higher Fermi level when deposited onto Pt. Higher Fermi level position is expected with donor-dopant and is a good indication of Nb effect. However, we do not observe Ba enrichment at the surface of BTO:Nb when identically sputtered onto single crystal of $SrTiO_3$. This difference suggests a correlation between the thin film microstructure, surface composition and doping effect. As a perspective, it would be nice to eventually see different mode of Nb incorporation between polycrystalline and epitaxial films. Perhaps, the polycrystalline character favours the Ba-migration due to ionic compensation of Nb whereas the lack of grain boundaries in epitaxial films is not favourable of Ba-migration. At least, we note that highly doped $BaTiO_3$:Nb single crystal are not possible to obtain.

When subsequently annealed under oxidizing conditions, deviations from stoichiometry and heterogeneous surface compositions have been found. We have observed large Ba-enrichment at the surfaces. This enrichment occurs by the formation of micro-crystals. Doping with Nb seems to enhance the Ba segregation. This point is again in favour of the Ba vacancies model in donor-doped BTO system.

Surface niobium segregation has also been evident on our sputtered $BaTiO_3$:Nb films. The Nb accumulation at the surface was successfully shown using depth profile measurement. Effective incorporation of Nb donors into $BaTiO_3$ thin films was also not evident from conductivity measurements. The insufficient doping is further indicated by the Fermi level position in XPS, which is considerably lower than those of doped BaTiO3 single crystals.. An

extension of the results is attempted to explain the contrasted results observed in the literature in which thin film properties are strongly different than their bulk parents.

After having investigated the surface properties of undoped and Nb-doped $BaTiO_3$ thin films, we have measured the interface formation with metal in order to determine the band alignment Asymmetric energy band diagrams between top and bottom electrodes were determined with Pt contacts. A Schottky barrier height of ~0.6 eV and ~1 eV are observed respectively for top and bottom contact. Similar results have already been established by Schafranek et al. [4] with undoped (Ba,Sr)TiO_3. The present work has extended the study with the influence of doping effect at the interfaces. Nb doping induces a band bending at the interfaces whereas undoped BTO show flat band behaviour. The space charge for doped films might be provided by a small amount of ionized Nb_{Ti} donors, . The present result show direct evidence for such space charge at the BTO:Nb/Pt interface. Space charge effect in $BaTiO_3$:Nb has already been probed by impedance spectroscopy [5] and is now directly evidenced at the metal junction.

Motivated by several studies on PTCR system (donor-doped BTO-based) in which the contact nature with the electrode have been shown to play a major role [6], we have investigated the contact formation of BTO:Nb/indium. Indeed, metals with large oxygen affinity (e.g. In) are typically used in multilayered PTCR devices to avoid high resistivity contacts, which might cover the desired PTCR effect. Nowadays, indium-gallium alloy is often used to realize ohmic contact but no direct determination of the interface properties has been reported so far. Negligible Schottky barrier could be directly identified with In deposition giving rise to ohmic contact properties without observable Ti reduced species in contrast to Pt deposition.

A more fundamental interface experiment has been performed between $BaTiO_3$ and $SrTiO_3$:Nb materials. Electrical studies of $SrTiO_3/BaTiO_3$ have been performed by several authors [7] and highly asymmetric behavior were evidenced in their electrical measurements using Pt as top electrode and STO:Nb as bottom electrode. These observations are believed to be explained by the interface properties of the $SrTiO_3/BaTiO_3$ contact, which has been found to induce ideal ohmic contact to $BaTiO_3$ with no barriers for charge injection. In addition, a sharp interface with a zero valence band offset has been experimentally determined in good agreement with previous theoretical calculations [8], interface studies [9] and electrical

properties [7]. It would also be nice to provide our own electrical measurements on such stacks. We first did not succeed to obtain good electrical contact with the $SrTiO_3$:Nb single crystal. We note that this difficulty agree with the lower surface doping observed in STO:Nb. Then, the insertion of indium-gallium alloy between STO:Nb substrate and the probe tip could improve the contact quality, which also agree with the In experiment. But at this stage of the writing, the results could not be formatted at time for the present manuscript. Recent C─V measurements performed on $SrTiO_3$:Nb/$BaTiO_3$/Pt structure have shown large asymmetrical behaviour in good agreement with the band alignment determination. Additional dielectric measurements will thus be shown during the examination of the PhD.

The dielectric properties of Pt/$ATiO_3$/Pt stacks have been consequently much easier to obtain. We have compared sputtering deposition under *on* and *off*-axis configuration. The microstructure could be enhanced with *off*-axis sputtering films as showed with AFM and XRD measurements. Using an appropriate scaling, the dependence of the maximum of the permittivity was found to be frequency independent for *off*-axis deposition compared to *on*-axis films showing frequency dispersion. For BST thin film compositions, the plotting of the Curie-Weiss behaviour is closer to the bulk properties for transverse deposition, which also agrees with the general improvement obtained for better thin film microstructures. Additional experiments might be suitable to identify the nature of the differences (grain sizes, growth mode, and chemical composition) to ensure these preliminary results.

Finally we discussed the Ba features, which reveal two different chemical states. The origin of the second barium component is not understood but it is suggested to study the dependence of Ba2 in dependence of the substrate orientation similarly to the study of the O shoulder in $SrTiO_3$ single crystal. Unfortunately, such Nb-doped $BaTiO_3$ single crystals are not as available as Nb-doped $SrTiO_3$ single crystal.

This thesis presents a systematic study of undoped and Nb-doped $BaTiO_3$ using in-situ photoemission spectroscopy. Simultaneous information on electronic and chemical properties of the interfaces could be obtained. Correlation with theoretical prediction might be further suitable to obtain a better understanding of the band structure of perovskite titanate.

Corresponding literature

[1] R. Schafranek. (2009), *Thesis*, Kathodenzerstäubte (Ba,Sr)TiO_3- Dünnschichten für steuerbare Mikrowellenkomponenten Material-, Bauteil- und Grenzflächeneigenschaften, TU Darmstadt.

[2] V. Reymond. (2004), *Thesis.* Nouvelles couches minces et multicouches derives de $BaTiO_3$: optimisation des propriétés diélectriques, ICMCB of Bordeaux.

[4] R. Schafranek, S. Payan, M. Maglione, and A. Klein. (2008), *Phys. Rev. B.* **77**, 195310.

[5] M. Maglione and M. Belkaoumi. (1992), *Phys. Rev. B.* **45**, 2029-2034.

[6] W.J. Heywang. (1971), *Mater. Sci.* **6**, 1214.

[7] K. Abe, S. Komatsu, N. Yanase, K. Sano, and T. Kawakubo., (1997), *Jpn J. Appl. Phys.* **36**, 5846.

[8] J. Junquera, M. Zimmer, P. Ordejon, and P. Ghosez., (2003), *Phys. Rev. B.* **67**, 155327.

[9] F. Amy, A.S. Wan, A. Kahn, F.J. Walker, and R.A. McKee., (2004), *J. Appl. Phys.* **96**, 1635

Remerciements à… **Acknowledgments to…** **Herzlichen Dank an…**

- **Mario Maglione**, *intrinsèquement admirable, je lui dois tant.*
- *Ich danke* **Andreas Klein**, *für seine Aufmerksamkeit und Flexibilität. Ich habe von ihm in kurzer Zeit sehr viel gelernt.*
- **Sandrine Payan** & **Robert Schafranek** *sans qui rien n'aurait commencé.*
- **Jean Etourneau**, *président du jury et infatigable rassembleur d'hommes.*
- **Wolfram Jaegermann**, *to have developed a nice atmosphere of work in the surface science group. "no risk, no fun"*
- **Christophe Muller**, *pour avoir rapporté ma thèse et supporté avec moi la visite à Cripple Creek.*
- **Dieter Schmeißer** & **Wolfgang Donner**, *as members of the committee of my PhD and occasionally, amateur of "Gitane".*
- **Claude Delmas**, *pour m'avoir accueilli au sein de l'institut.*
- **Rodolphe Decourt**, *un phrasé affuté, une générosité sans faille, il sait tous réparer sauf peut-être lui-même.*
- **Shunyi Li**, 我期待着，不久我将能够与您在中国相会。
- **Juergen, Azad, Merhdad** & **René,** *the band of Darmstadt.*
- **Anthony** & **Marjorie**, *de la fraîcheur ces deux-là !!*
- **Lionel,** *physicien du plasma spécialiste du XIX^{ème} Siècle, un mélange rare* !
- **Sascha, Marcus and Olivier**, *Der perfekte WG.*
- **Elias, U-Chan, Cathy, Mickael, Dominique** & **Annie**
- **Cédric,** *spécialiste Olympien !!*, **Aurélien** *Héraultais dans l'âme !!*, **Jéré** *dégoupilleur hors normes !!* & **Alex**
- **L'ADOC** *et ses adociens.*
- **Le Thib, Le Ben, Joseph** & **Marie**, *avec eux c'est du solide sans défaut.*
- **Enfin à toute ma famille,** *parfois dubitative dans mes choix improbables mais toujours derrière.*

Permanent e-mail address : emmanuelarveux@gmail.com

Propriétés de surfaces et interfaces de couches minces ferroélectriques de $BaTiO_3$ étudiées par spectroscopie de photoémission in-situ

Résumé :
Cette thèse porte sur l'étude de couches minces ferroélectriques à base de $BaTiO_3$ déposées par pulvérisation cathodique. Ces matériaux permettent par exemple de réaliser des condensateurs accordables ou encore des mémoires non-volatiles pour le stockage d'informations. Cependant, leurs propriétés diélectriques sont considérablement dégradées par des effets extrinsèques d'interfaces; film/substrat ou encore film/électrode. Dans ce contexte, la spectroscopie de photoémission (XPS) a été utilisée pour quantifier les états électroniques et chimiques de ces interfaces avec une approche in-situ. L'étude sur la formation du contact film/électrode a permis de mesurer la hauteur de barrière de Schottky partiellement responsable des caractéristiques capacités – tensions des couches. Des phénomènes de ségrégation ont été mis en évidence révélant une profonde instabilité de la stœchiométrie de surface. Enfin, la conséquence d'un dopage au niobium dans les couches minces de $BaTiO_3$ est discutée du point de vue des modes de compensation, de la solubilité du dopant et des propriétés diélectriques.

Mots clés :

• $BaTiO_3$ • Couches minces • Ferroélectricité • Propriétés de surface
• Propriétés des interfaces • Spectroscopie de photoémission • dopage • Ségrégation

---

Surface and interface properties of $BaTiO_3$ ferroelectric thin films studied by in-situ photoemission spectroscopy

Abstract :
The aim of this work was to better understand the surface and interface properties of sputtered ferroelectric $BaTiO_3$ thin films. They are typically used as dielectrics in integrated capacitors, electromechanical sensors and so. This thesis studies the chemical and electronic structures of the interface of $BaTiO_3$ in order to understand basic mechanisms of contact formation with the substrate and the electrode like the Schottky barrier height. Furthermore, the surface stoichiometry of such films has been investigated under different thermal preparation revealing significant instability through segregation phenomenon. Finally, the doping effect with niobium is studied regarding compensation mode, dopant solubility and dielectric properties. The experimental setup allows for in-situ analysis of surface and interface properties using photoelectron spectroscopy.

Keywords :

• $BaTiO_3$ • Thin films • Ferroelectrics • Surface properties • Interface properties
• Photoemission spectroscopy (XPS) • Doping effect • Segregation